REPUBLIC OF TURKEY
YILDIZ TECHNICAL UNIVERSITY
GRADUATE SCHOOL OF SCIENCE AND ENGINEERING

SPACE RADIATION ESTIMATION FOR THE TURKISH LUNAR MISSION

Burak BEKTAŞOĞLU

MASTER OF SCIENCE THESIS
Department of Physics
M.Sc. Programme in Physics

Supervisor
Asst. Prof. Murat HÜDAVERDİ

Co-supervisor
Prof. Dr. M. Bilge DEMİRKÖZ

August, 2022

REPUBLIC OF TURKEY
YILDIZ TECHNICAL UNIVERSITY
GRADUATE SCHOOL OF SCIENCE AND ENGINEERING

SPACE RADIATION ESTIMATION FOR THE TURKISH LUNAR MISSION

A thesis submitted by Burak BEKTAŞOĞLU in partial fulfillment of the requirements for the degree of **MASTER OF SCIENCE** is approved by the committee on 11.08.2022 in Department of Physics, M.Sc. Programme in Physics.

Asst. Prof. Murat HÜDAVERDİ Yıldız Technical University Supervisor	Prof. Dr. M. Bilge DEMİRKÖZ Middle East Technical University Co-supervisor

Approved By the Examining Committee

Asst. Prof. Murat HÜDAVERDİ, Supervisor
Yıldız Technical University _____

Assoc. Prof. Ufuk SAKARYA, Member
Yıldız Technical University _____

Prof. Dr. Hüseyin ÇAVUŞ, Member
Çanakkale Onsekız Mart University _____

I hereby declare that I have obtained the required legal permissions during data collection and exploitation procedures, that I have made the in-text citations and cited the references properly, that I haven't falsified and/or fabricated research data and results of the study and that I have abided by the principles of the scientific research and ethics during my Thesis Study under the title of Space Radiation Estimation for The Turkish Lunar Mission supervised by my supervisor, Asst. Prof. Murat HÜDAVERDİ. In the case of a discovery of false statement, I am to acknowledge any legal consequence.

Burak BEKTAŞOĞLU

Signature

This study was supported by YTU Scientific Research & Project Office (BAP) funding with contract numbers FBG-2021-4332 and was partially supported by the Turkish Academy of Sciences (TÜBA) and the Presidency of Strategy and Budget, grant number 2015K121190.

Dedicated to my family

ACKNOWLEDGEMENTS

First and foremost, I would like to express my deepest gratitude to my advisor, Asst. Prof. Murat Hudaverdi for his patience, motivation, support, and guidance with his experience during this research. I would like to express my deepest gratitude to my co-advisor Prof. Dr. Melahat Bilge Demirköz for her support, and guidance.

I would like to thank Prof. Dr. Tsvetan Dachev from the Space Research and Technology Institute of the Bulgarian Academy of Sciences for his support about the Chandrayaan-1 mission data. I would like to thank Burak Yaglioglu, Project Manager of the Turkish Lunar Mission from TUBITAK Space Technologies Research Institute, for his help.

My sincere thanks go to the wonderful team members of Yıldız Technical University-Space Science and Technology Research Group, Muhammed Kiyami Erdim, Fatih Hazar, Onur Unver, Dr. Cemile Ezer, Emine Gulmez, and Hakan Necmettin Azman, who have always helped and motivated me.

I would like to thank the whole team and Abdulrahman Albarodi who helped me at the Middle East Technical University- IVMER (Space and Accelerator Technologies Research and Application Center) laboratory.

I would like to thank Yıldız Technical University Scientific Research Projects Coordination Unit and Yıldız Technical University Foundation for their financial support during the project process.

I am grateful to my family and my friends for their continuous support during this project.

Burak BEKTAŞOĞLU

TABLE OF CONTENTS

LIST OF SYMBOLS

v	Velocity
Gy	Gray
s	Second
km	Kilometer
m	Meter
kg	Kilogram
R	Distance
M	Mass
G	Gravitational Constant
L	Angular Momentum

LIST OF ABBREVIATIONS

GMAT	General Mission Analysis Tool
SPENVIS	Space Environment Information System
ISRO	Indian Space Research Organisation
Geant4	Geometry and Tracking 4
RADOM	Radiation Dose Monitor
ESA	European Space Agency
NASA	National Aeronautics and Space Administration
NSSDC	National Space Science Data Center
SPE	Solar Particle Event
GCR	Galactic Cosmic Ray
TID	Total Ionizing Dose
DD	Displacement Damage
IO	Initial Orbit
EBO	Earth Bound Orbit
LTT	Lunar Transfer Trajectory
ILO	Initial Lunar Orbit
LO	Lunar Orbit
OLO	Operational Lunar Orbit
CAD	Computer Aided Design
STEP	Standard for the Exchange of Product Data

LIST OF FIGURES

LIST OF TABLES

ABSTRACT

Space Radiation Estimation for The Turkish Lunar Mission

Burak BEKTAŞOĞLU

Department of Physics
Master of Science Thesis

Supervisor: Asst. Prof. Murat HÜDAVERDİ
Co-supervisor: Prof. Dr. M. Bilge DEMİRKÖZ

One of the biggest challenges for space missions is space radiation effects. Space radiation is very dangerous to the health of astronauts on manned missions and can cause spacecraft electronic systems and solar panels to malfunction. It can even cause a task to be terminated. For this reason, the situation that the spacecraft will be in during the mission should be well known. Therefore, various simulations and tests must be performed to prepare for the space mission. In this way, precautions are taken in a way that electronic components and astronauts can withstand.

The trajectory used in space missions should be determined in such a way that it best suits the purpose of the mission and that the spacecraft is exposed to the lowest possible radiation dose. Because the less radiation the spacecraft will be exposed to, the easier it will be to take precautions on the spacecraft and reduce the cost of the mission.

In this study, a radiation environment simulation was made for the 2023 Turkish Lunar Mission to be carried out within the scope of the National Space Program. First, an estimated mission profile for the 2023 Lunar Mission was designed and a trajectory simulation was made. Second, data on the space particle environment on orbit were obtained for the estimated date of the mission. In addition, a model satellite was designed to be used in simulations. Finally, the particle flux data and the modeled satellite were used in the Geant4 simulation. The simulation found the radiation dose rate that the satellite will be exposed to in the 2023 Turkish Lunar Mission.

Keywords: Lunar mission, space radiation, space environment.

ÖZET

Türkiye Ay Misyonu için Uzay Radyasyon Tahmini

Burak BEKTAŞOĞLU

Fizik Anabilim Dalı
Yüksek Lisans Tezi

Danışman: Asst. Prof. Murat HÜDAVERDİ
Eş-Danışman: Prof. Dr. M. Bilge DEMİRKÖZ

Uzay görevleri için en büyük zorluklardan biri uzay radyasyon etkileridir. Uzay radyasyonu insanlı görevlerde astronotların sağlığı için oldukça büyük bir tehlike arz eder. Uzay araçlarının elektronik sistemlerinin, güneş panellerinin bozulmasına hatta görevin sonlanmasına sebep olabilir. Bu nedenle uzay aracının görev boyunca içinde bulunacağı durum iyi bilinmelidir. Bunun için çeşitli simülasyonlar ve testler yapılarak uzay görevine hazırlık yapılmalıdır. Bu sayede elektronik bileşenlerin ve astronotların dayanabileceği şekilde önlemler alınmaktadır. Uzay görevlerinde izlenen yörüngenin, görevin amacına en uygun şekilde ve uzay aracının olabildiğince düşük miktarda radyasyon dozuna maruz kalacağı şekilde belirlenmesi gerekmektedir. Bu çalışmada, Türkiye'nin Milli Uzay Programı kapsamında gerçekleştireceği Ay Görevi için bir radyasyon ortamı simülasyonu yapılmıştır. İlk olarak, 2023 Ay Görevi için tahmini bir yörünge oluşturuldu ve belirlenen tarihte yörünge üzerinde uzay aracının maruz kalacağı parçacık ortamı verileri elde edildi. Devamında, modellenen yörüngedeki parçacık akısı bilgisi elde edildi. Son olarak bu bilgilerle, modellenen uydunun 2023 Türkiye Ay Görevinde içinde bulunacağı radyasyon ortamı Geant4 kullanılarak simüle edildi.

Anahtar Kelimeler: Ay görevi, uzay radyasyonu, uzay ortamı.

YILDIZ TEKNİK ÜNİVERSİTESİ
FEN BİLİMLERİ ENSTİTÜSÜ

1
INTRODUCTION

1.1 Literature Review

Since it can cause the electronic systems in the spacecraft to malfunction and even cause the end of the mission, space radiation is one of the biggest problems to be taken care of in space missions. According to a report published by NASA in 1999, the US National Geophysical Data Center has recorded 4500 satellite anomalies or malfunctions due to space radiation effects in the last 25 years. This is an example of how serious the effects of space radiation are [1]. Space radiation is a greater threat in manned missions. Space radiation can produce acute effects on astronauts. Astronauts are exposed to radiation at effective doses in the range of 50-2000 millisievert (mSv). In the long run, this can cause diseases such as cancer, circulatory system disorders, and cataracts [2]. Various measurements are taken on all space missions in history, and some of them are radiation measurements. These measurement results can be used to prepare for future missions. During the mission, the spacecraft is exposed to trapped particles, solar particles, and galactic cosmic rays [3]. The effects of these particles on the electronic systems in the spacecraft can be examined under 3 headings. The first is the total ionizing dose effect, the second is the solar particle effect, and the third is the displacement damage [4]. Before a mission, preparation is made for space radiation based on measurement results from previous missions and simulation and test results.

The shield of the spacecraft plays a very important role in this. However, the shield for protection from radiation cannot be made in any thickness. Because as the shield thickness increases, the weight of the spacecraft increases and as the weight of the spacecraft increases, a stronger propulsion system is required [5]. The stronger propulsion system brings with it more weight. You can't put more fuel in a spacecraft either, because more fuel requires a larger fuel tank. A Larger fuel tank requires larger spacecraft. Thus, again, the weight of the spacecraft and the cost of the mission increase. Therefore, the shielding required for the protection of electronic components and astronauts is a sensitive issue, and the requirements must be well defined, and the right tests performed. How much radiation a spacecraft will be exposed to during the

mission depends on the date and orbit of the mission. Two examples can be given for this situation, respectively. Missions during peak solar activity are very risky because the risk of solar particles malfunctioning in the spacecraft increases considerably. A spacecraft in the Van Allen Belts, which originates from the Earth's magnetic field, must spend as little time in these belts as possible for the purpose of the mission. Therefore, planning is based on mission date and orbit.

1.2 Objective of the Thesis

On February 9, 2021, Turkey's 10-year National Space Program was announced. One of the goals of this program is to perform an unmanned Moon Mission in 2023. The aim of this thesis is to simulate the space radiation environment that the spacecraft will be exposed to during the 2023 Turkish Lunar Mission. For this purpose, many studies such as satellite design, orbital planning, and simulation algorithms have been carried out. During the studies, different methods were tried and the best possible method was chosen according to the results. The project was carried out in partnership with Yıldız Technical University Space Science and Technology Research Group and Middle East Technical University-IVMER (Space and Accelerator Technologies Research and Application Center), and the results were regularly presented to the Presidency of Defense Industries.

1.3 Hypothesis

Simulation results for the space radiation environment may differ from actual results. The first reason for this is the uncertainties in particle models. The second reason is the occurrence of unexpected effects such as strong solar flares. In addition, the models used in the simulation must be chosen correctly. In this study, first of all, an orbit was created using the General Mission Analysis Tool (GMAT) and the Space Environment Information System (SPENVIS) was used to simulate the particle environment in the orbit. A predicted satellite model made using AutoCAD was simulated using Geant4 (for Geometry and Tracking) with particle environment data. The same processes were tested for another mission to demonstrate the accuracy of this method. This mission is the Chandrayaan-1 mission accomplished by the Indian Space Research Organization (ISRO) in 2008. During this mission, the Chandrayaan-1 satellite made measurements with the detector named Radiation Dose Monitor (RADOM). Measurement data and simulation results were compared. In this way, the method used to simulate the radiation environment for the 2023 Turkish Lunar Mission was tested.

2
SPACE RADIATION ENVIRONMENT

Space radiation affects all space missions and all satellites and has three sources. The first source is the trapped particles found in the Van Allen Belts, the second source is solar particles and the third is galactic cosmic rays. The effects of space radiation on the electronic systems of spacecraft can be examined under four headings. These effects are total ionizing dose, single event effect, displacement damage, and spacecraft charging. These effects differ based on mission duration, mission date, and orbit used on the mission. The trajectory used for the 2023 Turkish Lunar Mission in this project is a partially advantageous trajectory in terms of space radiation damage, as the spacecraft is not planned to be in the Van Allen Belts for a long time and the mission period is not planned too long. However, the date of the 2023 Turkish Moon Mission is a bit of a disadvantage, as the mission is in a period when the effects of the Solar Cycle-25 increase. Because in 2023, the probability of a deterioration in the electronic systems of the spacecraft due to solar effects is higher than in the solar minimum period.

This thesis study was carried out by considering all these effects and the result obtained was compared with a previous mission that was performed. In this part of the thesis, the sources and effects of space radiation are mentioned.

2.1 Trapped Radiation

The fluid movement in the Earth's liquid iron core causes the formation of a magnetic field around the Earth [6]. It is also called geomagnetic field. The Earth's magnetic field interacts with the solar wind and this interaction causes an electrical current layer formation. It is known as magnetopause. The region enclosed by the magnetopause is known as the magnetosphere [7]. The green line in Figure 2.1 represents magnetopause and the thin yellow line shows magnetic field lines. The sunward side of the magnetosphere compresses by the solar wind, and shock waves are created on that side represented by a dark green line named Bow Shock.

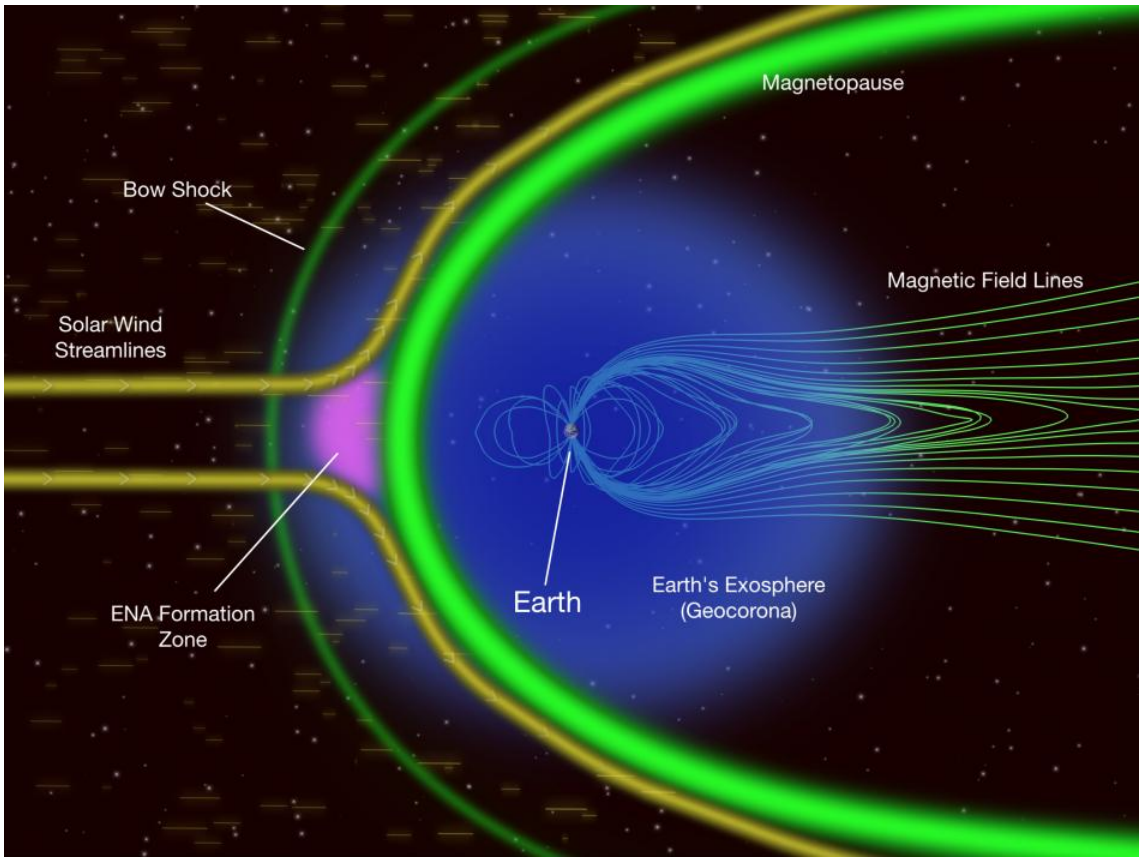

Figure 2.1 The Earth's magnetic field lines, magnetopause. Adapted from [8]

Energetic proton and electron populations trapped in the Earth's magnetosphere constitute the Earth's radiation belts that cause trapped particle radiation. The movements of the charged particles in the Earth's magnetic field are given in Figure 2.2. The particles rotate around the magnetic field line and move back and forth along the line. They also drift east or west depending on their charge [9].

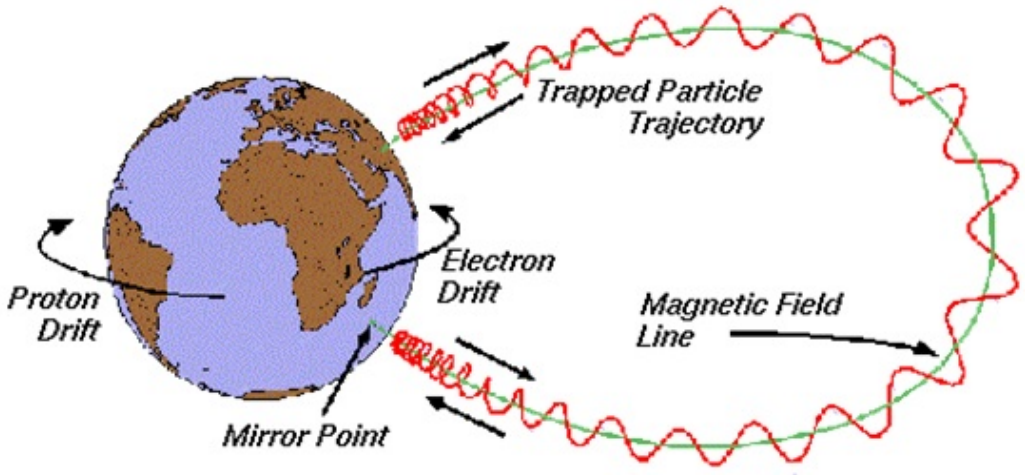

Figure 2.2 Motion of charged and energetic particles in the Earth's magnetic field. Adapted from [9].

The radiation belts were discovered by James Van Allen in 1958 with Geiger counters flying on the Explorer 1 satellite [10]. That's why these belts are also known as Van Allen Belts. These belts are two toroidal-shaped distinct belts that surround the Earth [11]. The first one is called the inner radiation belt and the second one is called the outer radiation belt. Inner and outer Van Allen radiation belts are given in Figure 2.3.

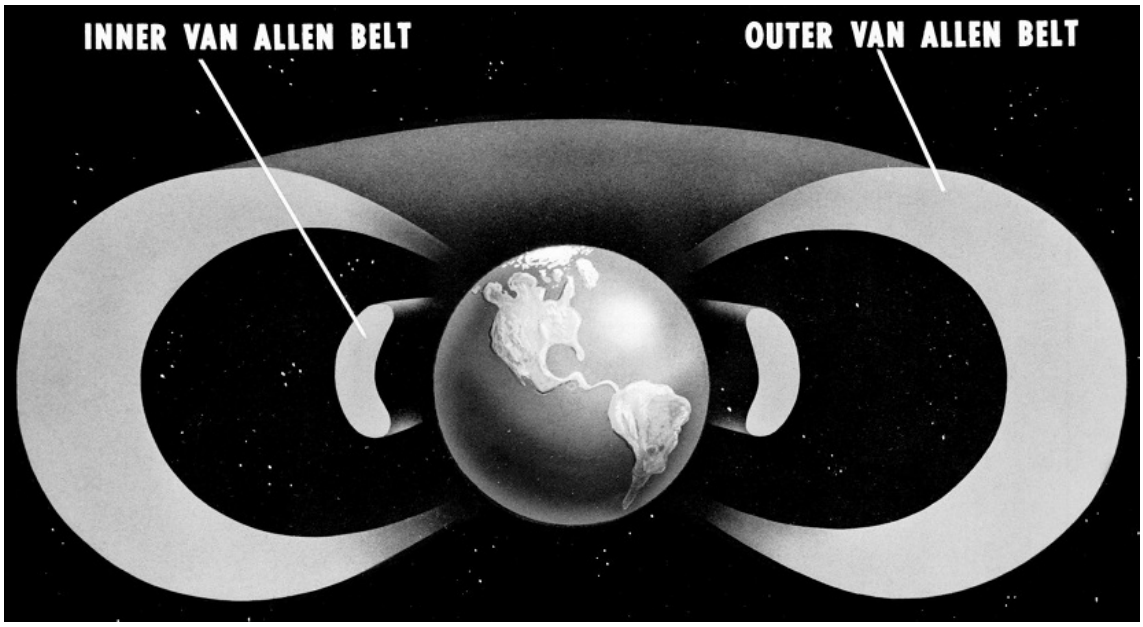

Figure 2.3 Inner and outer Van Allen Belts. Adapted from [12].

Protons are located in just one radiation belt, while electrons are located in two belts [13]. The inner belt extends from about 0.1 to 2 R_E and the outer belt extends from approximately 3 R_E to 9-10 R_E [14]. The main zones of the inner belt and outer belt are centered at around 1.5 R_E and 4 R_E respectively.

Space Environment Information System (SPENVIS) was used to obtain the fluxes of the trapped particles. SPENVIS is developed by the Royal Belgian Institute for Space Aeronomy for European Space Agency's (ESA) Space Environments and Effects Section [15]. There are different models for trapped particles in SPENVIS. Information of AP-8/AE-8 and CRRESPRO/CRRESELE for proton and electron are given in Table 2.1. The model chosen for the trapped particles is the AP-8 and AE-8 models. The accuracy of the method used for the 2023 Turkish Lunar Mission simulations has been demonstrated according to the simulation results for the Chandrayaan-1 mission. The results of CRRES models and AP models are shared for the simulations for the Chandrayaan-1 mission [11]. However, the CRRES model from these models was not used for the Lunar mission. This is because the energy gap in the results obtained from the CRRESPRO and CRRESELE models is not wide. Extrapolating for flux values at higher energies will detract from reality. For this reason, In this study, the AP-8 Max model for protons and the AE-8 Max model for electrons were used.

Table 2.1 SPENVIS proton and electron models for Van Allen Belts. Adapted from [9]

PROTON MODELS		
Model	Coordinate Range	Energy Range (MeV)
AP-8	$1.14 \leq L \leq 6.60$	0.10-400.00
CRRESPRO	$1.00 \leq L \leq 5.50$	1.10-90.40
ELECTRON MODELS		
Model	Coordinate Range	Energy Range (MeV)
AE-8	$1.14 \leq L \leq 12.00$	0.04-7.00
CRRESELE	$2.50 \leq L \leq 6.80$	0.50-6.60

CRRESPRO and CRRESELE models developed by U.S Air Force Research Laboratory [16]. AP-8 and AE-8 models were developed by NASA in the 1980s as a result of the data collected from 1958 to 1970 and made available by U.S. National Space Science Data Center (NSSDC) [11, 17]. The energy range for the proton in the AP-8 model is between 1.00×10^{-1} MeV and 4.00×10^{2} MeV, and for the electron in the AE-8 model, the energy range is between 4.00×10^{-2} MeV and 7 MeV [18, 19]. The distribution of protons with energies higher than 10 MeV and electrons with energies higher than 1 MeV in the Van Allen belts are given in Figure 2.4 and Figure 2.5, respectively [9].

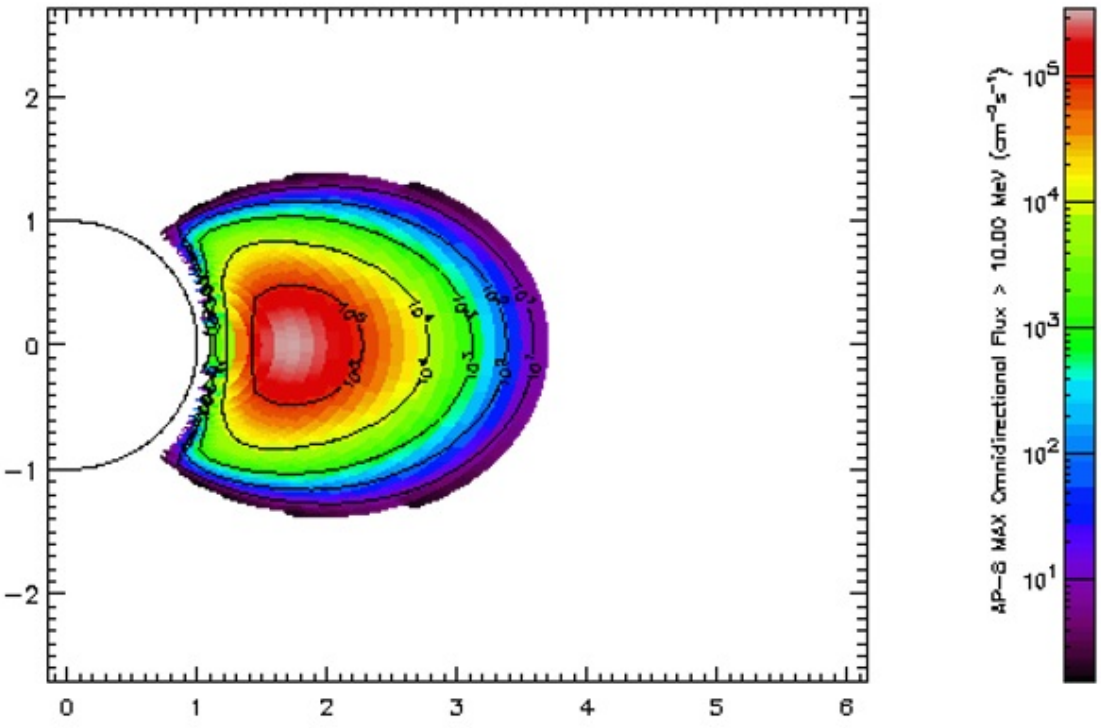

Figure 2.4 Proton flux in Van Allen Belt. Adapted from [9].

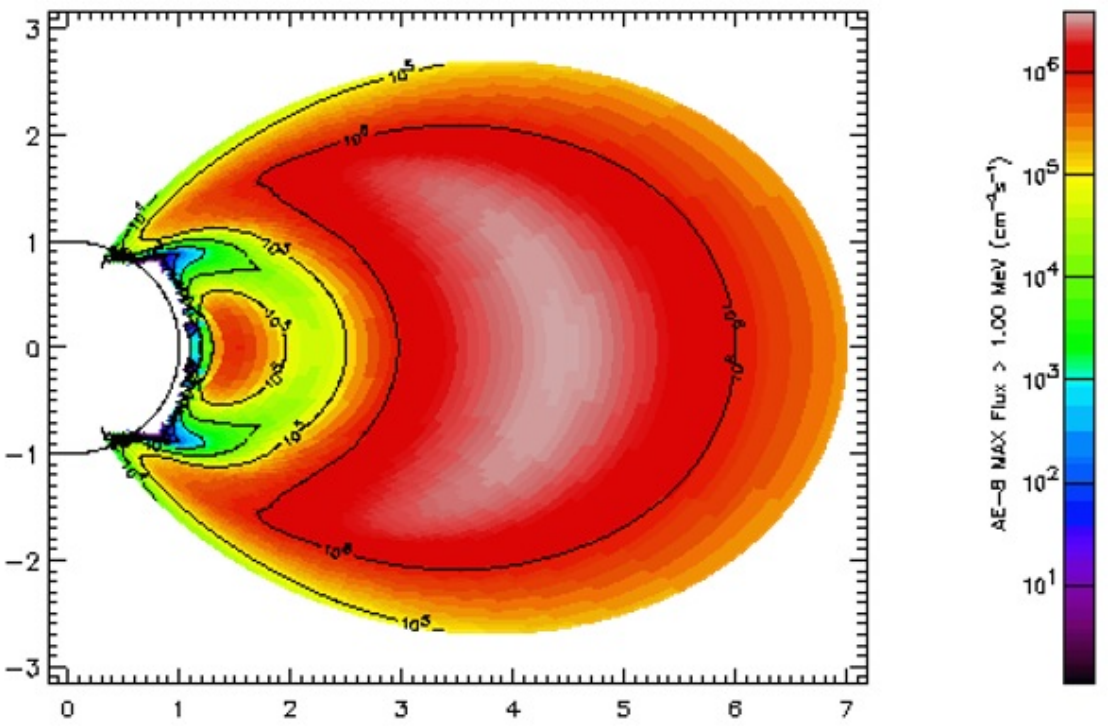

Figure 2.5 Electron flux in Van Allen Belts. Adapted from [9].

In space missions, it is necessary to stay in the regions with dense particle flux in Figure 2.4 and Figure 2.5 as short as possible. The high particle flux in these regions may cause undesirable adverse effects on the spacecraft or -in manned missions- the crew.

2.2 Solar Particle Events (SPE)

Solar particle events (SPEs) are another source of space radiation. Solar particle events can give radiation hazards to electronic components on spacecraft and humans in crewed missions [20]. Solar energetic particles consist of energetic protons, electrons, alpha particles, and heavy ions up to the iron and their energies can up to a few GeV. Solar flares occur on the surface of the Sun due to nuclear reactions taking place in the Sun. Coronal mass ejections (CMEs) occur near the region of the solar flare. CMEs are large bubbles of plasma (Figure 2.6) emanating from the Sun's outer atmosphere, and shockwaves are formed before coronal mass ejections. Solar particles are accelerated by the shockwaves and their speed can approach the speed of light [21].

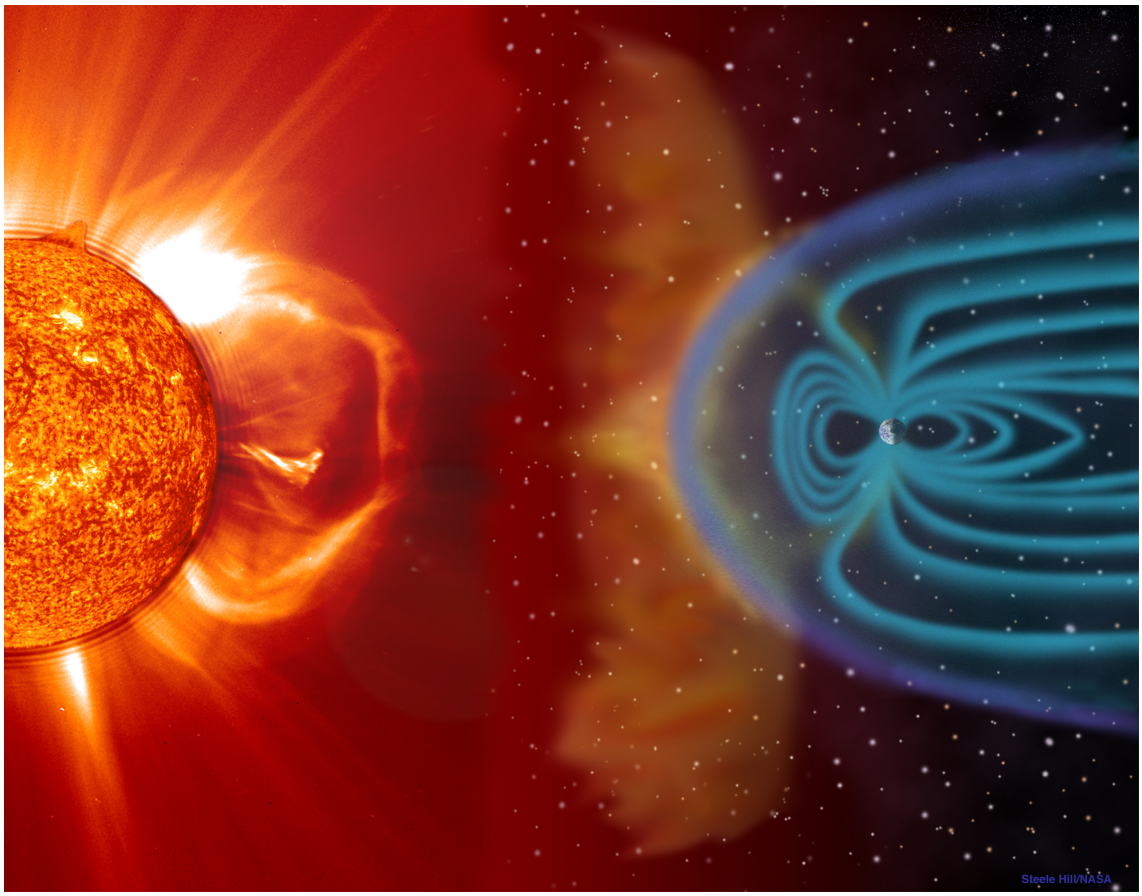

Figure 2.6 Coronal Mass Ejection. Adapted from [22].

The flux of SPEs increases or decreases according to the Sun's 11-year cycle. Solar flares occur several times a day during the solar maximum period, while they occur much less frequently during the solar minimum period. Of the 11-year solar cycle, 4 years are the solar minimum period and 7 years are the solar maximum period [23]. Figure 2.7 shows the difference between the sun's maximum and minimum periods.

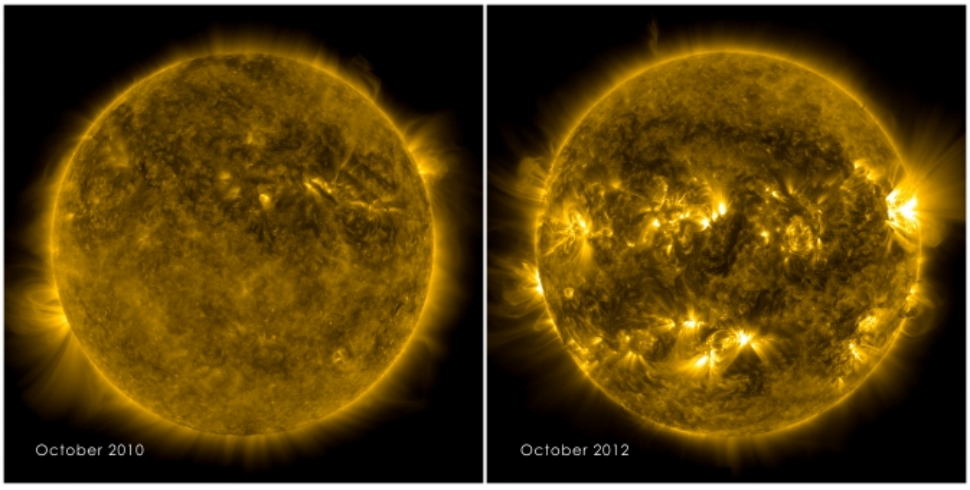

Figure 2.7 Coronal Difference between solar maximum and solar minimum. Adapted from [24].

There are several solar particle models in SPENVIS. These models are examined under two headings (Table 2.2). These are solar proton models and solar heavy ion models.

Table 2.2 Solar particle models in SPENVIS. Adapted from [25].

Solar Proton Models	
1	Solar Accumulated and Peak Proton and Heavy Ion Radiation Environment (SAPPHIRE)
2	Emission of Solar Protons (ESP)
3	Model of Jet Propulsion Laboratory (JPL-91)
4	The Rosenqvist Model
5	The King Model
Solar Heavy Ion Models	
1	Solar Accumulated and Peak Proton and Heavy Ion Radiation Environment (SAPPHIRE)
2	Prediction of Solar Particle Yields for Characterizing Integrated Circuits (PSYCHIC)

The models used in SPENVIS to obtain the solar particle flux on the mission orbit are the combined versions of the models. Combined versions of these models are given in Table 2.3. In all models except the King Model, the ion range can be selected as desired from hydrogen to uranium.

Table 2.3 Models available in SPENVIS for particle flux in orbit. Adapted from [15].

1	SAPPHIRE (Total fluence)
2	SAPPHIRE (Worst event fluence)
3	SAPPHIRE (1 in n year event fluence)
4	ESP-PSYCHIC (Total fluence)
5	ESP-PSYCHIC (Worst event fluence)
6	King Model

In this study, the ESP-PSYCHIC model was used for solar particles. Because the proton energy value is constrained due to the incomplete nature of the datasets of the King and JPL models. In addition, according to the Fluence-Energy comparison of the ESP-PSYCHIC model and the SAPPHIRE models, the ESP-PSYCHIC model was thought to be more reliable because it created the intermediate value on the graph, and therefore the ESP-PSYCHIC model was preferred [26]. ESP-PSYCHIC model was developed by the National Aeronautics and Space Administration (NASA) and has an energy range of 1.00×10^{-1} MeV - 5.00×10^{2} MeV [15].

2.3 Galactic Cosmic Rays (GCR)

The energetic flux of particles caused by supernovas and their remnants outside the solar system are known as galactic cosmic rays (GCRs). Galactic cosmic rays are the most penetrating type of ionizing radiation, and their distribution in the interstellar medium is thought to be isotropic. It also constantly bombards the Earth from all angles. The energy range of GCR particles can range from a few tens to $10{\times}10^{20}$ eV/nucleon [11]. Galactic cosmic rays consist of from hydrogen to iron in the periodic table but 99% of galactic cosmic rays are hydrogen and alpha particles. Heavy ions form of remaining 1% of GCRs [27]. The relative abundance graph in the galactic cosmic ray is given in Figure 2.8.

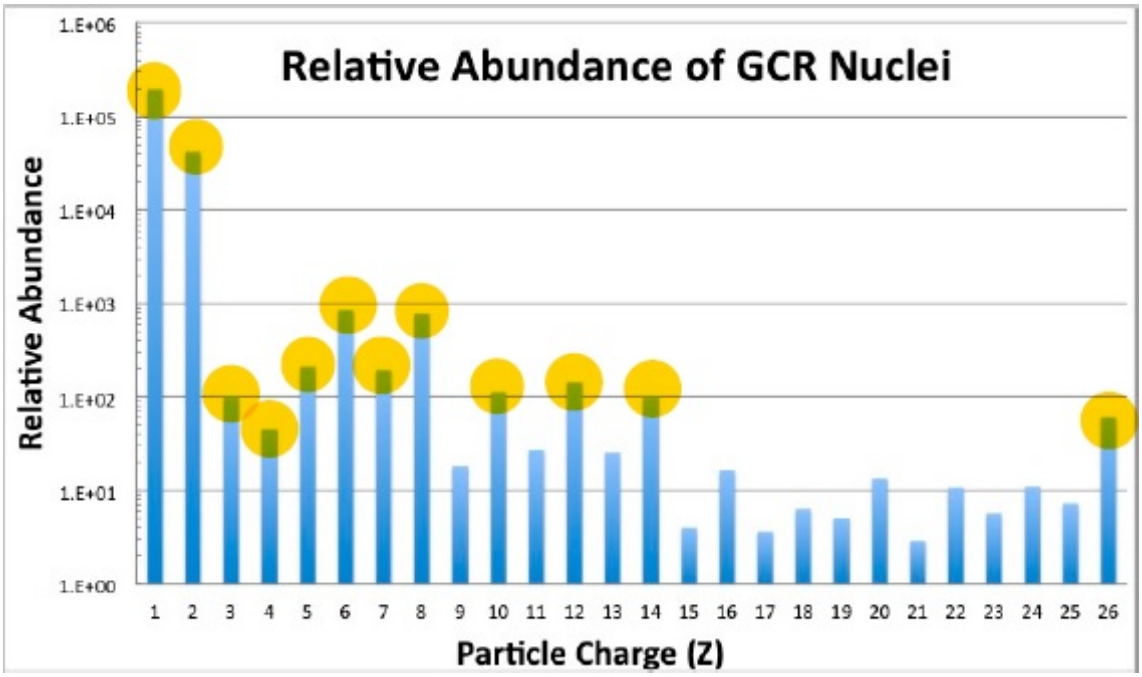

Figure 2.8 GCR element abundance graph. Adapted from [28].

For galactic cosmic ray particles, there are four different models in SPENVIS. These models are given in the Table 2.4 [29].

Table 2.4 Galactic cosmic ray models in SPENVIS. Adapted from [15].

1	ISO 15390 Model
2	CREME 96 Model
3	CREME 86 Model
4	Nymmik Model

The CREME96 Model is fundamentally different from the CREME86 and corresponds to the GCR maximum in 1986-87. The CREME86 model, on the other hand, gives different results according to various space weather indices. The Nymmic model is the same as the ISO 15390 model, except that the flux increases with decreasing energy for particles below 10 MeV [30]. For this reason, in this study, the ISO 15390 model was thought to be more efficient and was used in simulations. The ISO-15390 model was developed by Lomonosov Moscow State University-Skobeltsyn Institute of Nuclear Physics and Royal Belgian Institute for Space Aeronomy (BIRA-IASB). This model takes into account the variation in GCR intensity versus the solar cycle, using the 12-month average number of Sunspots [30]. In addition, the time delay in the GCR flux was taken depending on the solar cycle and the magnetic stiffness of the particles. There are no abnormal cosmic rays in this model [29]. ISO 15390 standard model particle energy range is between 1.00 MeV and 1.00×10^5 MeV.

2.4 Space Radiation Effects on Electronics

Space radiation can affect the electronic systems of spacecraft and the health of astronauts in manned missions in various ways. For this reason, it is an important issue how resistant spacecraft is to space radiation, and in this study, the effects of space radiation on spacecraft electronic systems are emphasized. In this context, space radiation can have an effect in 3 ways. These are total ionizing dose (TID), single event effect (SEE), and displacement damage (DD). Total ionizing dose and displacement damage are cumulative effects [4]. Tests for these effects can be made in Turkey at the Middle East Technical University Defocusing Beamline (DBL) at the Turkish Energy, Nuclear and Mining Research Council SANAEM Proton Accelerator Facility. At the Proton Accelerator Facility, protons can accelerate up to 30 MeV of kinetic energy, and ESA ESCC No. 25100 Standard Single Event Effect Test Method and Guideline is considered for these SEE tests. Also, TID tests can be performed at the Gama Irradiation Facility at the same location [31] [32].

2.4.1 Total Ionizing Dose (TID)

The gradual space radiation that a spacecraft's electronic system components are exposed to throughout its mission life creates a total ionizing dose effect by accumulating free charge [33]. Ionization results from the interaction of a material's atoms with charged particles or high-energy photons. Photon-induced ionization occurs when the secondary electrons formed by the high-energy photon form electron-hole pairs. Proton and other charged particles also cause ionization by forming electron-hole pairs. This degradation begins when the total ionizing radiation tolerance of the electronic system reaches its tolerance limit [34].

During the mission, it is possible to model the space environment in orbit where the spacecraft will travel [34]. Photon sources and particle accelerators are used to test electronic components against this effect [33]. Thus, it is understood how long the electronic component will withstand these effects. The total ionizing dose is the measure of deposited energy per unit mass. According to The International System of Units (SI), the unit used for TID is Gray (Gy). 1 Gy equals to 100 rad. The total ionizing dose (TID) effect usually occurs in conjunction with single event effects (SEE) and displacement damage (DD) [34].

2.4.2 Single Event Effects (SEEs)

The single event effect (SEE) is caused by an ionizing particle that creates a free charge as it passes through the sensitive region of the electronic component [35]. Figure 2.9 shows the single event effect mechanism.

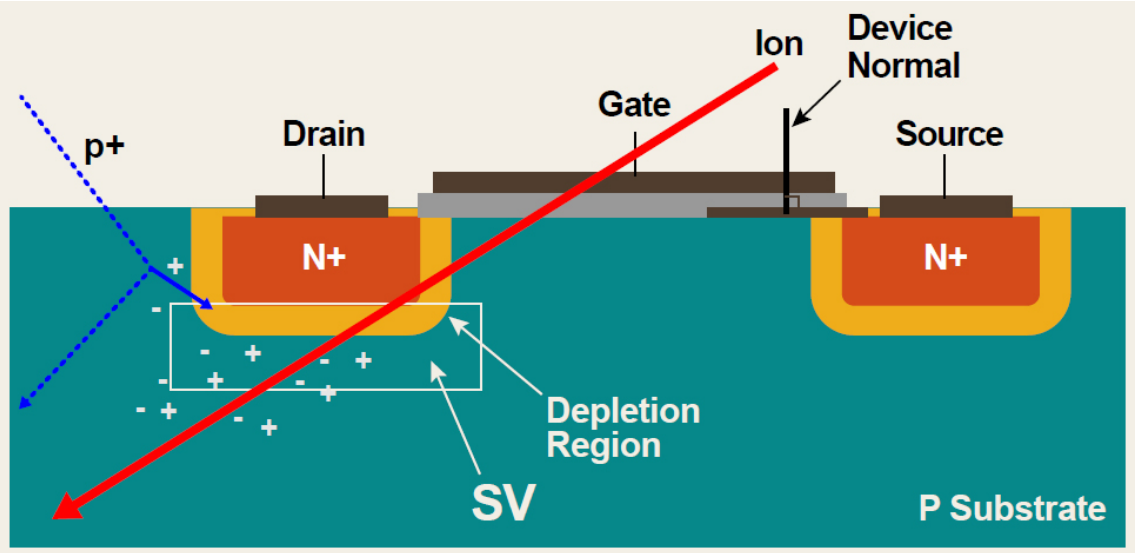

Figure 2.9 Single event effect mechanism. Red line shows heavy ion path in device. Blue (dashed) arrow indicates recoil ion generation by a proton and an atom in the semiconductor lattice. Adapted from [35].

Single event effects fall into two categories. These are soft errors and hard errors. The soft errors category consists of single event upset, single event transient, single event snapback, and single event functional interrupt. The hard errors category consists of single event latch-up, single event burnout, and single event gate rupture [36]. Single event effects and their definitions are given in Table 2.5.

Semiconductor memory devices have many capacitors, and the sensitivity increases as these memory systems get smaller. Hard errors are caused by mechanical faults such as poor solder, connector failure, and the damaged component needs to be replaced, and these are repeatable errors. However, soft errors are caused by alpha particles or cosmic rays and cause changes in the data stored in memory and are temporary, non-repeating errors. Correct data can be reloaded into the memory cell when a soft error occurs. If the soft error is not corrected, it can create a system failure or be mistaken for a system failure [37].

Table 2.5 Soft and hard errors. Adapted from [38][39].

Error Type	**Error**	**Error Explanation**
Soft	Single Event Upset (SEU)	Change of logic cell or microprocessor state and not destructive.
Soft	Single Event Transient (SET)	Transient voltage excursion in an integrated circuit.
Soft	Single Event Snap-Back (SESB)	Localized warming up after high current state.
Soft	Single Event Functional Interrupt (SEFI)	Component deterioration (reset or lock-up).
Hard	Single Event Latch-Up (SEL)	Potential devastating damage. A low impedance and high current path are formed.
Hard	Single Event Burnout (SEB)	Regenerative feed-back, and high current.
Hard	Single Event Gate Rupture (SEGR)	Rupture of the dielectric layer or gate oxide.

2.4.3 Displacement Damage (DD)

An energetic particle (proton, electron, neutron, and heavy ion) can cause a displacement of an atom by elastic or inelastic collision from its normal lattice position in a semiconductor, and it is known as displacement damage [40]. If the displaced atom moves to the non-lattice position, this defect is called an interstitial [41]. In silicon, the resulting interstitial silicon and vacancy pair is called the Frenkel defect (Figure 2.10).

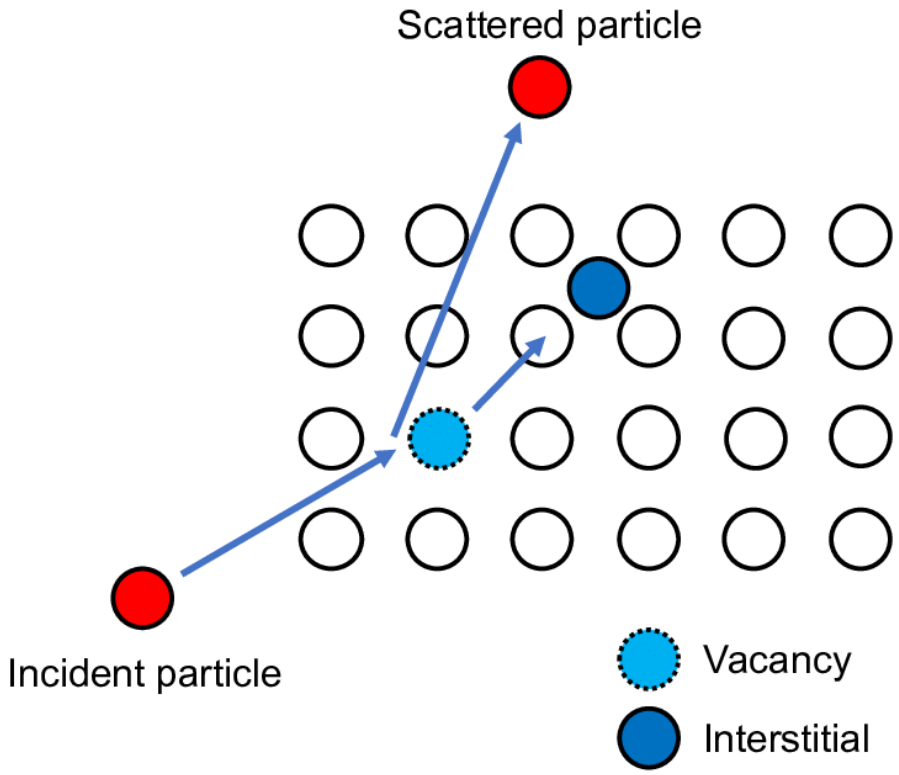

Figure 2.10 Single event effect. Adapted from [42].

Interstitials or gaps formed as a result of the collision cause the formation of allowed energy states in the band gap in the semiconductor material. This affects the performance of electronic devices [40]. This type of damage, for example, can do quite a bit of damage to solar panels. It causes an increase in the resistance of the solar cells, thus reducing the energy production of the solar cells [41].

Non-ionizing energy loss (NIEL) is calculated as the energy lost per unit mass of a particle as it moves through the material. NIEL has the same unit as linear energy transfer (LET) [40].

3
TRAJECTORY PLANNING

Mankind began its Moon missions with the Union of Soviet Socialist Republics and the United States. Beginning with the Luna-1 satellite mission in 1959, the Moon missions continued with the Luna satellite series and the Ranger missions in the 1960s. The first lunar impact was performed on the Luna-2 mission. The first manned Moon landing mission was made by the United States on July 20, 1969, with the Apollo-11 mission [43].

The distance between the Moon and the Earth is roughly 384400 km [44], but this distance varies between 356500 km and 406700 km [45]. Various orbits have been used in missions to cover this distance. Basically, two issues are interrelated here, these are the cost of the space mission and the duration of the mission. Shortening the spacecraft's arrival time to the Moon increases the cost of the mission. Here, of course, issues such as whether the mission is manned or not and the purpose of the mission are very effective [43]. The orbit used in the Luna-2 mission to directly hit the Moon's surface and the orbit used in the Apollo 11 mission are given in Figure 3.1 and Figure 3.2. Although both missions were lunar missions, the purpose of these two missions and the use of very different spacecraft required different mission profiles.

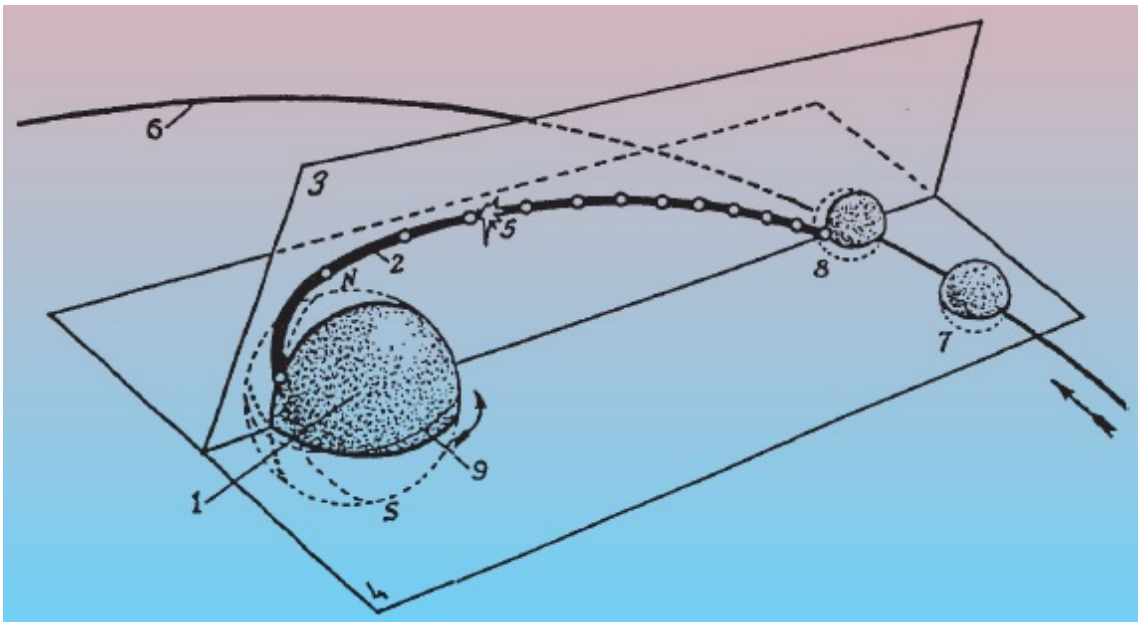

Figure 3.1 Luna-2 mission trajectory profile. The Luna-2 mission is the first to touch the Moon. Adapted from [43].

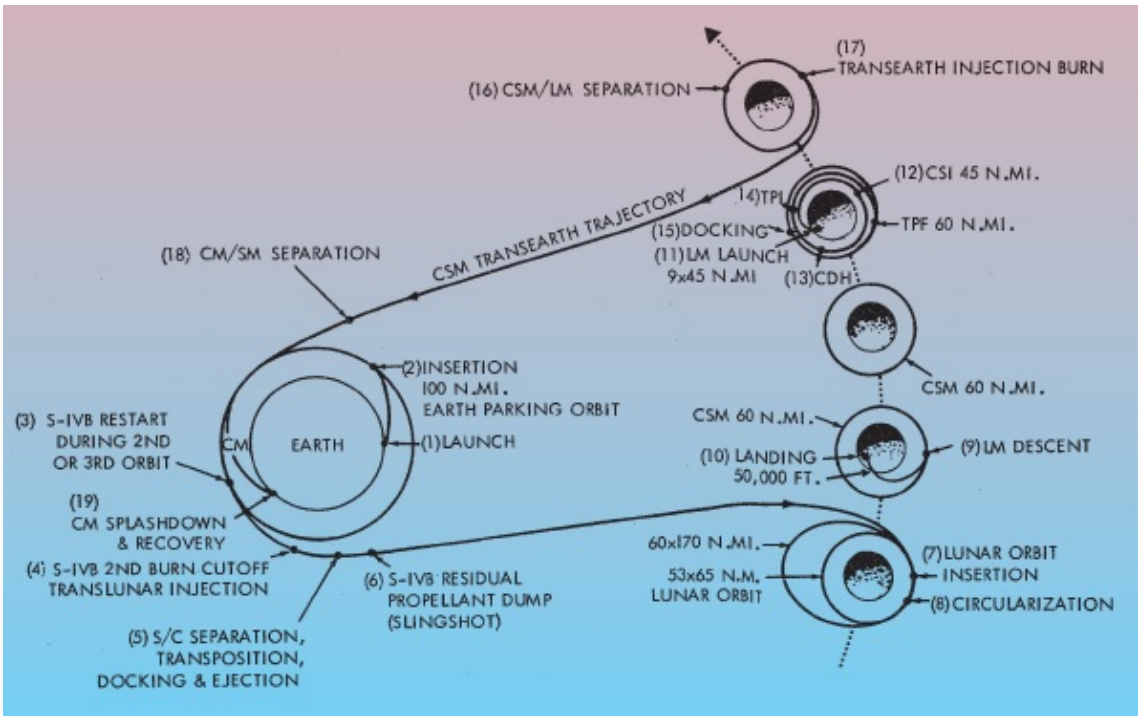

Figure 3.2 Apollo 11 mission profile. In the mission, it entered the 34-hour Moon transfer orbit after one and a half orbits in the Earth Parking Orbit at an altitude of about 185 km. After completing its transfer orbit, it entered lunar orbit. While in lunar orbit, the Lunar module, which contained two of the three astronauts in the crew, separated from the crew module attached to the service module and landed on the Moon. This mission is the first manned Moon mission in human history. Adapted from [43].

In lunar missions, the distance and duration of transfer orbits may differ. While the Luna-2 orbit given in Figure 3.1 took 1 day and 10 hours (34) hours, the Moon transfer orbit in the Apollo 11 mission given in Figure 3.2 took 3 days (72 hours). In addition, in the Luna 9 mission, the lunar transfer orbit took 79 hours (3 days and 7 hours), while the Lunar prospector took 4 days and 9 hours (105 hours). These lunar transfer trajectories are given in Figure 3.3 [46].

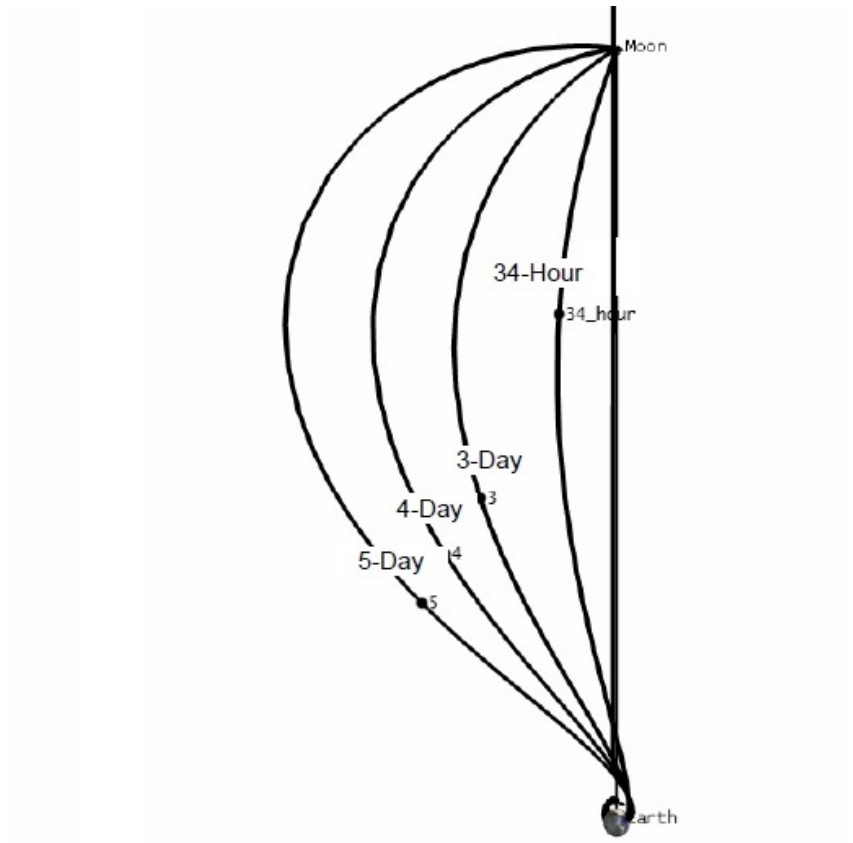

Figure 3.3 Transfer trajectories. Adapted from [46].

In lunar missions, the mission profile usually starts with the park orbit, and then the Hohmann transfer orbit is used. The Hohmann transfer orbit uses 2-body dynamics. Of the two bodies on a Moon mission, one is the Earth and the other is the spacecraft on the Hohmann transfer orbit extending from the Earth Park orbit through the Keplerian ellipse to the Moon. Delta-v (Δv) would have to be large for spacecraft following this orbit to be captured by the Moon. The Hohmann transfer profile for a Moon mission and the calculation of simply delta-v (Δv) are given below [47].

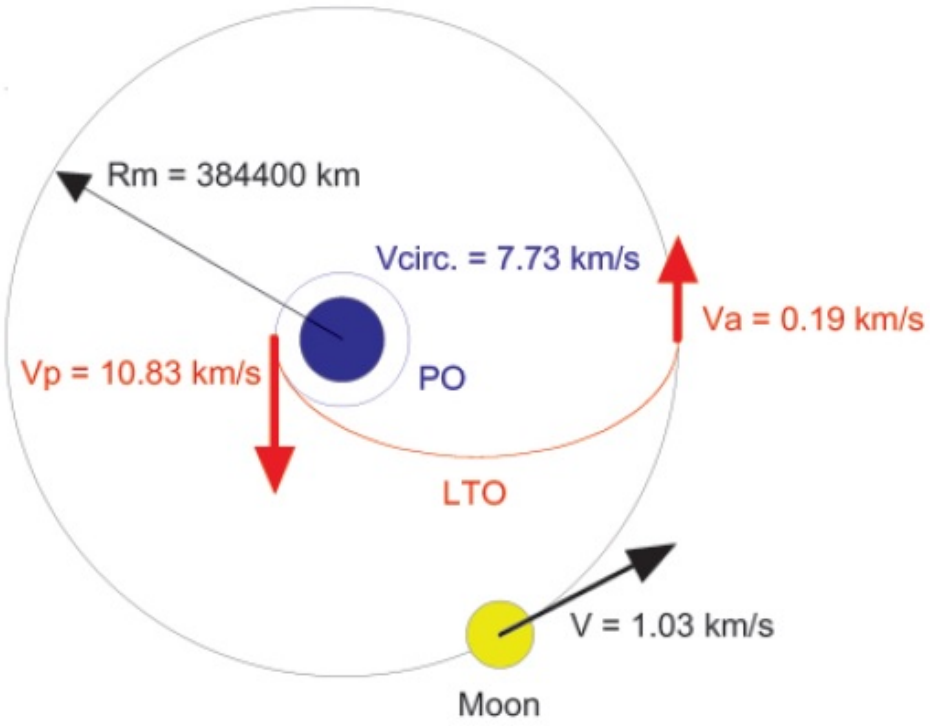

Figure 3.4 The velocities of a spacecraft reaching the Moon by Hohmann transfer from the Earth Parking Orbit at an altitude of 300 km. Adapted from [43].

Equation 3.1 is used to find the orbital velocity of the spacecraft on parking orbit at an altitude of 300 km before the trans-lunar injection [43][48].

$$v = \sqrt{\frac{GM}{R}} \tag{3.1}$$

The Earth radius (R_E)[49]: 6378.142 km (Equatorial radius referans)
Altitude (R_A): 300 km

$$R = R_E + R_A \tag{3.2}$$

Total Distance (R): 6678.142 km = 6678142 m
Newtonian constant of gravitation (G) [50]: $6.6743 \times 10^{-11} kg^{-1}m^3s^{-2}$
The Earth mass (M_E) [51]: $5.9722 \times 10^{24} kg$

$$v = \sqrt{\frac{(6.6743 \times 10^{-11} kg^{-1}m^3s^{-2})(5.9722 \times 10^{24} kg)}{(6678142m)}} \tag{3.3}$$

$$v = 7.725 km/s \tag{3.4}$$

Equation 3.5 is used to find the Δv required for trans-lunar injection. The distances in Equation 3.5 are shown in Figure 3.5 [52].

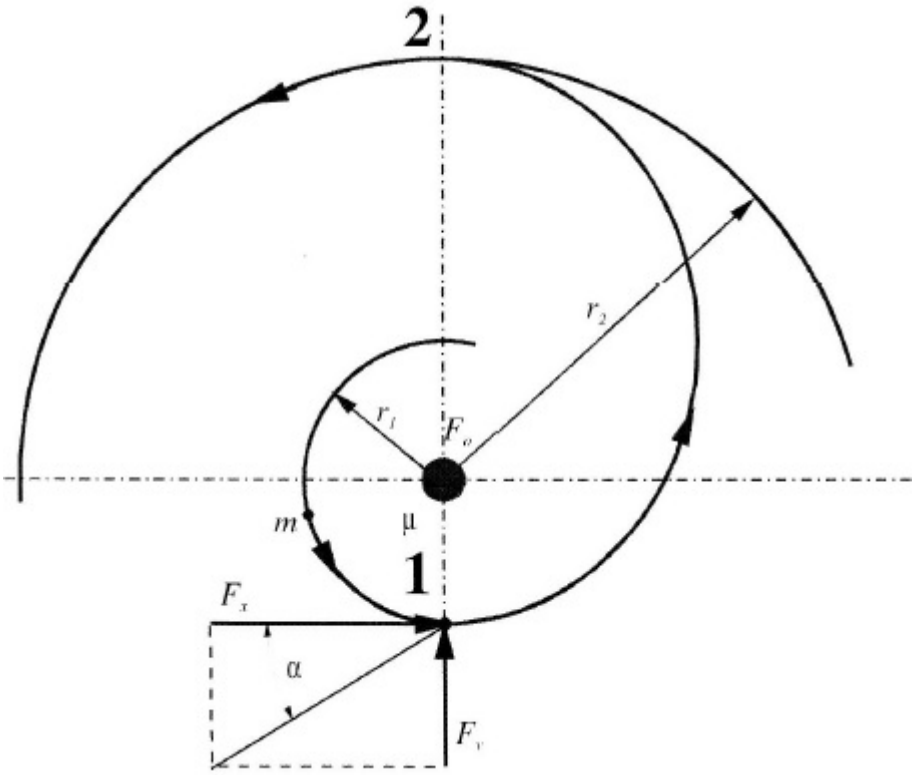

Figure 3.5 r_1 is the radius of the small circular orbit and r_2 is the radius of the large circular orbit. The transfer orbit between two circular orbits is the Hohmann transfer orbit. Adapted from [52].

$$\Delta v = \sqrt{\frac{\mu}{R_1}}\left(\sqrt{\frac{2R_2}{R_1+R_2}}-1\right) \tag{3.5}$$

$$R_1 = R = R_E + R_A = 6678142m \tag{3.6}$$

$$\mu = GM, \sqrt{\frac{\mu}{R_1}} = \sqrt{\frac{GM}{R}} = v = 7.725km/s = 7725m/s \tag{3.7}$$

$$R_2 = D_M + R_E \tag{3.8}$$

D_M:Distance of the Moon from the Earth

$$D_M = 384400000m \quad , \quad R_E = 6378142m \tag{3.9}$$

$$R_2 = 390778142m \quad , \quad 2R_2 = 781556284m \tag{3.10}$$

$$R_1 + R_2 = 397156284m \tag{3.11}$$

$$\Delta v = (7725m/s)\left(\sqrt{\frac{781556284m}{397156284m}} - 1\right) \tag{3.12}$$

$$\Delta v = 3111m/s = 3.111km/s \tag{3.13}$$

The perigee velocity of the spacecraft in the Hohmann transfer orbit is the sum of its velocity in the circular orbit and the Δv velocity and is given in 3.14. This result is found in Figure 3.4.

$$v_p = v + \Delta v = (7.725 + 3.111)km/s = 10.836km/s \tag{3.14}$$

Equation 3.15 is used to find the velocity of the spacecraft when it reaches lunar orbit. The values in the equation are given in Figure 3.6.

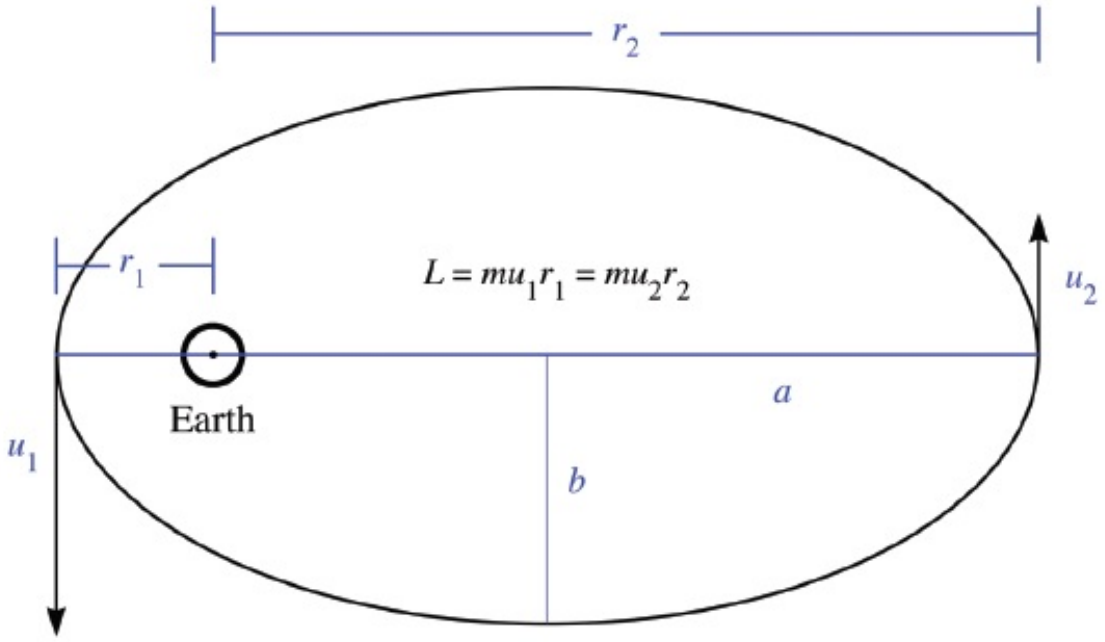

Figure 3.6 Assuming that a spacecraft in an elliptical orbit with a semi major axis a and a semi minor axis b will go to the Moon by making a Hohmann transfer, its velocity when it enters the Lunar Transfer Trajectory will be u1 and when it finishes the transfer orbit its speed will be u2. Here you can make calculations using the angular momentum formula. r1 can be taken as the sum of the Earth radius and the altitude of the earth park orbit, and r2 as the sum of the Earth radius length and the distance to be reached at the end of the transfer trajectory. v_1 instead of u_1 and v_2 instead of u_2 were used in transactions. Adapted from [48].

Angular momentum is L=mvr. Therefore we can get Equation 3.15 [48].

$$v_1 r_1 = v_2 r_2 \tag{3.15}$$

$$v_1 = 10.836 km/s \quad , \quad r_1 = 6678.143 km \quad , \quad r_2 = 390778.142 km \tag{3.16}$$

$$v_2 = \frac{v_1 r_1}{r_2} = \frac{(10.836 km/s)(6678.143 km)}{390778.142 km} = 0.185 km/s \tag{3.17}$$

In order for the spacecraft with a speed of 0.185 km/s to be captured by the Moon with a speed of 1.022 km/s [53], the propulsion system must be operated and one or more burns should be made.

There are also low-budget mission profiles from the Hohmann transfer. Ballistic capture method is one of them. Ballistic capture method was used for Japan's Hiten space probe. This method consumes less fuel and therefore requires a lower budget. The trajectory of the Hiten probe is given in the Figure 3.7 [47]. Of course, to use such orbits, your mission objective must allow it.

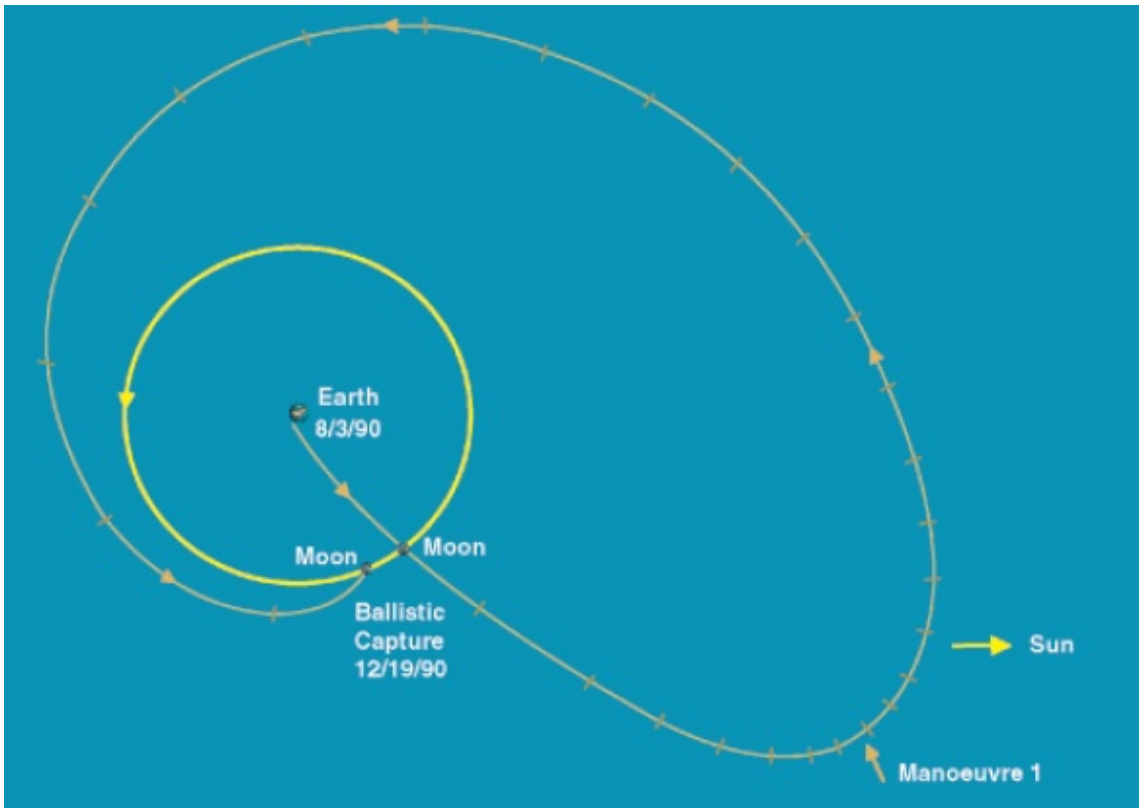

Figure 3.7 Hiten mission profile. Ballistic capture method was used in this mission. Adapted from [43].

When the mission profile of the 2023 Turkish Lunar Mission was first studied, the Hohmann transfer orbit was also among the options. Various orbits have been created and results for each compared, but one of the goals of the 2023 Lunar Mission is to collect as much scientific data as possible. For this reason, a longer mission plan was made instead of mission planning such as going directly to the Moon, and the data of the Chandrayaan-1 mission were used in these studies. The profile of the Chandrayaan-1 mission is similar to the mission profile considered for the 2023 Turkish Lunar Mission [54]. During the mission, the Chandrayaan-1 satellite measured the radiation dose rate with the Radiation Dose Monitor (RADOM) on the satellite.

For this study, some of the data of this measurement were shared by Prof. Dr. Tsevetan Dachev from the Bulgarian Academy of Sciences. The shared part of the data consists of the initial orbit of the mission. Since the purpose of this thesis is to find the radiation dose rate that the spacecraft will be exposed to during the 2023 Turkish Lunar Mission, the first orbital portion of the Chandrayaan-1 mission was simulated exactly and compared with real mission data [11]. Thus, the relationship between the results of the method used and the actual data was obtained. The mission profile of Chandrayaan 1 is given in Figure 3.8. During the nearly 10-month mission, the Chandrayaan-1 satellite gradually increased its peak in its orbit around the Earth and reached the Moon [54].

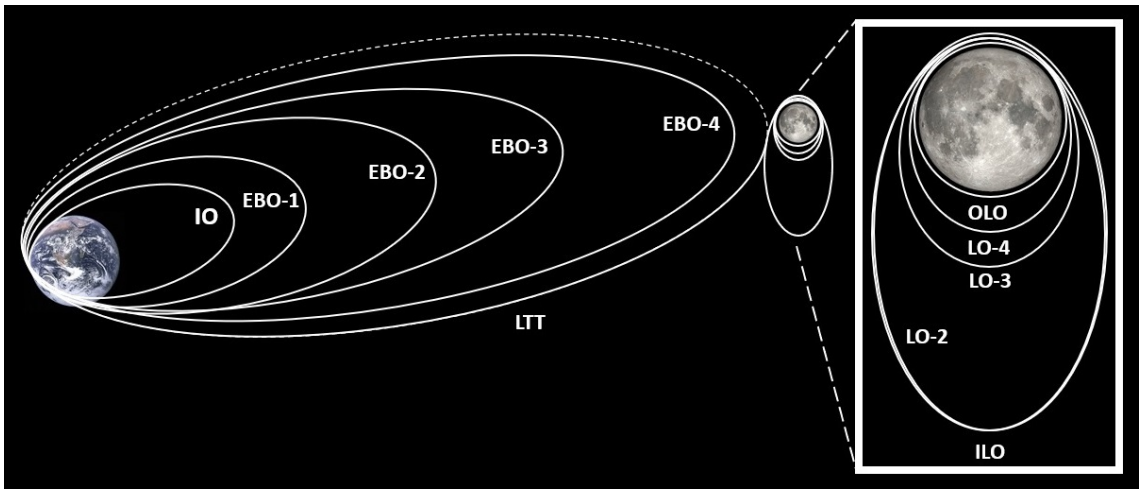

Figure 3.8 IO: Initial Orbit. EBO: Earth Bound Orbit. LTT: Lunar Transfer Trajectory. ILO: Initial Lunar Orbit. LO: Lunar Orbit. OLO: Operational Lunar Orbit [55][56][57].

Chandrayaan-1 spent about 13 days in orbit around the Earth and reached the Moon in about four and a half days. After 4 days of orbit correction around the Moon, Chandrayaan-1 was in a 100 km circular orbit for about nine and a half months and completed its mission. The perigee, apogee, and periselene, aposelene distances of Chandrayaan-1's orbits throughout the mission are given in Table 3.1 [54].

Table 3.1 Chandrayaan-1 mission phases [54].

Orbit	Distance	Orbit	Distance
Initial Orbit (IO)	Perigee: 254.4 km Apogee: 22860.7 km	Initial Lunar Orbit (ILO)	Periselene: 507.9 km Aposelene: 7510.1 km
Earth Bound Orbit 1 (EBO-1)	Perigee: 299.2 km Apogee: 37908.1 km	Lunar Orbit 2 (LO-2)	Periselene : 200.6 km Aposelene: 7502.4 km
Earth Bound Orbit 2 (EBO-2)	Perigee: 336.6 km Apogee: 74715.9 km	Lunar Orbit 3 (LO-3)	Periselene: 183.0 km Aposelene: 255.2 km
Earth Bound Orbit 3 (EBO-3)	Perigee: 347.9 km Apogee: 165015.7 km	Lunar Orbit 4 (LO-4)	Periselene: 101.7 km Aposelene: 255.2 km
Earth Bound Orbit 4 (EBO-4)	Perigee: 459.6 km Apogee: 266613.0 km	Operational Lunar Orbit (OLO)	Periselene: 101.9 km Aposelene: 102.8 km
Lunar Trasnfer Trajectory (LTT)	Perigee: 972.8 km Apogee: 379860.2 km		

One of the documents used for trajectory planning of the 2023 Turkish Lunar Mission is the article of Burak Yaglioglu, the Project Manager of the Turkish Lunar Mission at TUBITAK Space Technologies Research Institute. The article was published in the December issue of the "Anahtar Dergi", the journal of the Ministry of Industry and Technology of the Republic of Turkey [58]. Details of the modeled trajectory are given in Section 3.1.

3.1 Trajectory to the Moon

According to the article published in the journal of the Ministry of Industry and Technology, in the 2023 Turkish Moon Mission, the spacecraft is planned to start the mission with an orbit with a perigee of 300 km and an apogee of 125,000 km [58]. The spacecraft will then perform two orbit-raising maneuvers. After spending approximately one month in this part of the mission, it will be injected into the lunar transfer trajectory, which takes 5 days, and the spacecraft will reach the Moon. After reaching the Moon, the spacecraft will spend one month to placing in a circular polar orbit of 100 km [58]. The spacecraft will make a hard landing after completing its mission by collecting various data for 3 months in polar orbit of 100 km. The estimated mission profile is designed in 3 stages and these stages are given below.

1. Earth Bound Orbit
2. Lunar Transfer Trajectory
3. Lunar Orbit

The estimated mission profile of the 2023 Turkish Lunar Mission is given in Figure 3.9.

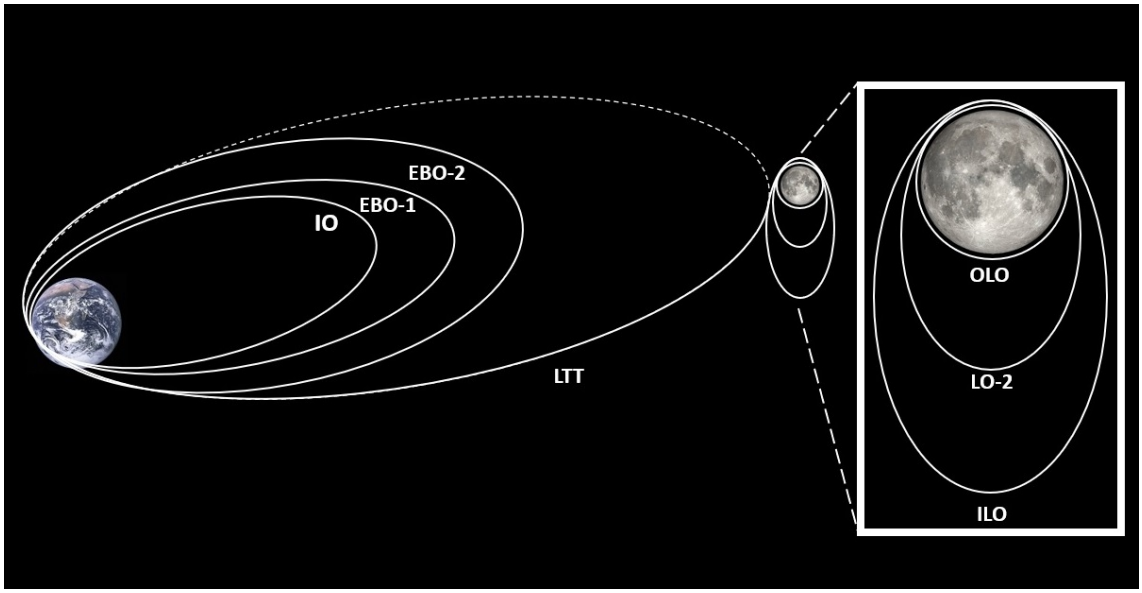

Figure 3.9 IO: Initial Orbit. EBO: Earth Bound Orbit. LTT: Lunar Transfer Trajectory. ILO: Initial Lunar Orbit. LO: Lunar Orbit. OLO: Operational Lunar Orbit.

There are various programs for trajectory planning, such as the System Tool Kit (STK) and the General Mission Analysis Tool (GMAT). These programs use gravitational fields with varying accuracy and offer a graphical environment [59]. In this study, the General Mission Analysis Tool was used in trajectory planning. General Mission Analysis Tool is open source software developed with contributions from NASA, the private sector, and the public [60]. Images of trajectory simulation from GMAT are given in Figure 3.10 and Figure 3.11.

3.1.1 Earth Bound Orbits

The chosen date of the mission is 13 June 2023. The orbital planning of the model satellite starts at 14:00:00.000 according to the UTC time zone. The inclination of the trajectory is nearly 29.6 degrees. According to the predicted mission profile, the apogee will be raised by a series of two orbital burns that will be performed after the initial orbit. The perigee and apogee of the initial orbit are 300 km and 125000 km respectively. After completing nearly 13 days (number of orbits is 6) in IO, propulsion system engines will run, and the satellite will perform an orbit-raising maneuver. According to the predicted mission profile, with this maneuver, the apogee will be raised to 175000 km (EBO-1). After orbiting for 10 days (number of orbits is 3) in EBO-1, the second orbit raising maneuver will perform to raise the apogee to 225000 km. The number of orbits in EBO-2 is 1. The IO, EBO-1, and EBO-2 parts of the mission take approximately 27 days in total. The GMAT view of the designed orbit is given in Figure 3.10.

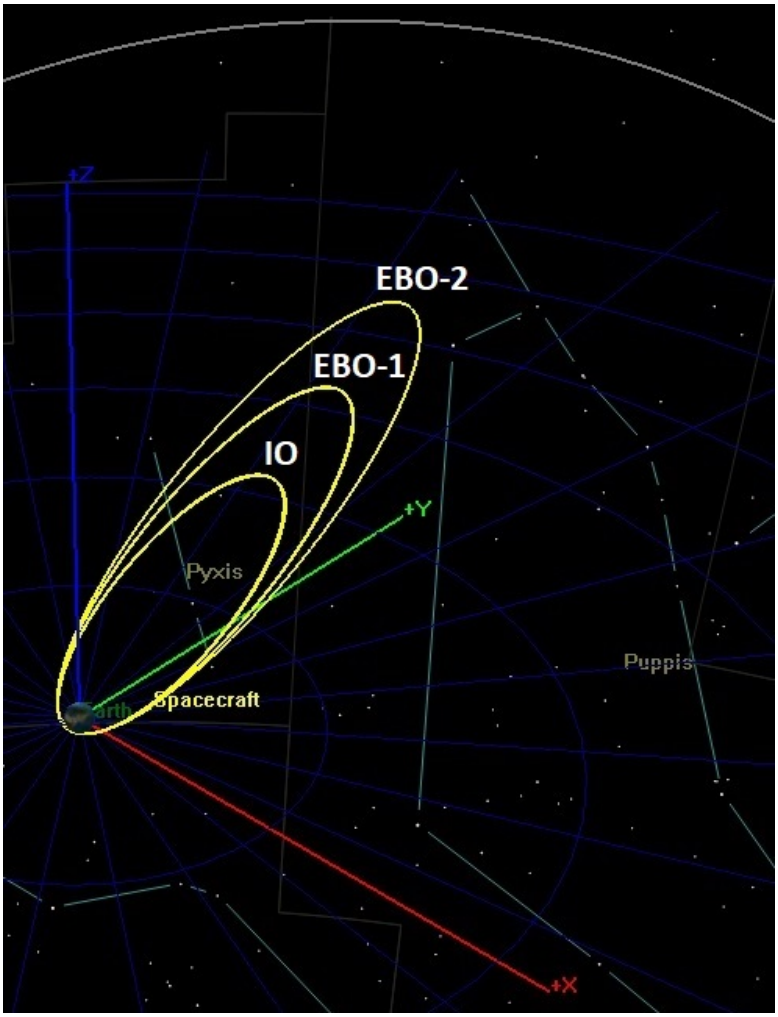

Figure 3.10 Earth Bound Orbits of the mission. IO: Initial Orbit. EBO: Earth Bound Orbit. The gray circular line above shows the orbit of the Moon. The blue line represents the +Z axis, the red line the +X axis, and the green line the +Y axis.

3.1.2 Lunar Transfer Trajectory

On 10 July 2023, nearly 27 days after the start of the mission, the modeled satellite will perform a trans-lunar injection burn. The lunar transfer trajectory will take 5 days, and 32 days after the start of the mission, the modeled satellite will have reached the Moon. It is thought that the hybrid propulsion system produced by DeltaV in Turkey will be used in the first maneuver in this part of the mission [58]. The image of the lunar transfer trajectory from the GMAT program is given in Figure 3.11. The gray circular line represents the Moon's orbit, and the yellow curved line represents the transfer orbit the spacecraft used to reach the Moon.

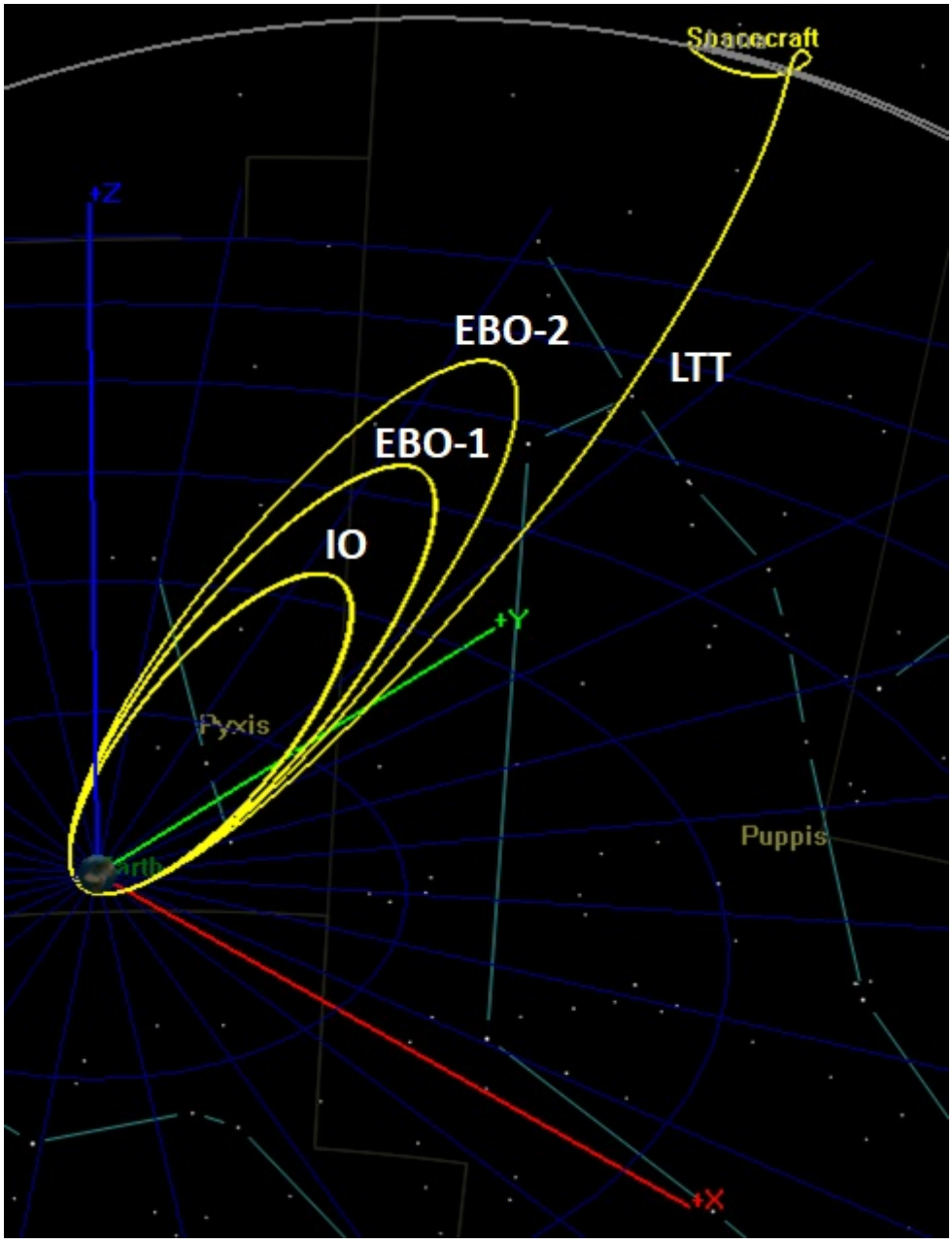

Figure 3.11 Lunar Transfer Trajectory (LTT). The blue line represents the +Z axis, the red line the +X axis, and the green line the +Y axis.

3.1.3 Lunar Orbit

Once the spacecraft is placed in lunar orbit, it is expected to take a month to place on a 100 km circular orbit. Meanwhile, the satellite, which continues to collect data, will spend 3 months in a 100 km circular orbit and complete its mission [58]. While obtaining the particle flux for the lunar orbit, it was assumed that the spacecraft was in a circular orbit at an average lunar distance of 384,400 km for 4 months. Therefore, estimation of aposelene and periselene altitudes in lunar orbit was not considered necessary. You can find the orbital altitudes and departure dates for this part of the mission in Table 3.2.

Table 3.2 Estimated mission plan of 2023 Turkish Lunar Mission. Dates are written as DD/MM/YYYY. The altitude of Lunar Orbit 2 and deadline information for Lunar Orbit 1 were not written, as no predictions were made about the lunar orbit. (AFMS: Altitude From Moon Surface)

Orbit	**Deadline in Orbit**	**Altitude of Orbit**
Initial Orbit (IO)	26/06/2023 03:10	Perigee: 300 km Apogee: 125000 km
Earth Bound Orbit 1 (EBO-1)	06/07/2023 02:19	Apogee: 175000 km
Earth Bound Orbit 2 (EBO-2)	10/07/2023 19:50	Apogee: 225000 km
Lunar Transfer Trajectory (LTT)	15/07/2023 12:15	Apogee: 393000 km
Lunar Orbit 1 (LO-1)	-	AFMS: 6203 km (Initial Altitude)
Lunar Orbit 2 (LO-2)	14/08/2023	-
Operational Lunar Orbit (OLO)	12/11/2023	100 km Circular Polar Orbit

4
MODELING OF LUNAR MISSION SATELLITE

A model satellite design was needed for use in the Geant4 simulation. However, since the design of the vehicle to be used in the 2023 Turkish Lunar Mission could not be reached while these studies were being carried out, an estimated satellite design was made within the scope of this study. While designing the estimated satellite to be used in the Geant4 simulation for the 2023 Turkish Lunar Mission, the design of the Chandrayaan-1 [55] and LRO (Lunar Reconnaissance Orbiter) [61] satellites was inspired. The sole purpose of the design is to obtain a satellite model to be used in the Geant4 simulation. The modeling of the satellite to be used in the mission was completed with the contributions of Turkish Lunar Mission Project Manager Burak Yaglioglu from TUBITAK Space Technologies Research Institute and used in the Geant4 simulation. The spacecraft model has 4 tanks to represent the chemical propulsion system. Also, the model contains a predicted model of the hybrid propulsion system. While making predictive modeling for the hybrid propulsion system, it was inspired by the images shared by the Turkish Space Agency in various sources. The hybrid propulsion system was made by DeltaV Space Technologies Inc. in Turkey with local and national resources [58]. There is one antenna and one solar panel on the satellite. In addition, a laser altimeter-like device was placed outside the satellite to represent any payload to be placed outside the satellite [62]. AutoCAD [63] and FreeCAD [64] were used to design the satellite. GDML file is required to import the design into Geant4 simulation. GUIMesh was used to obtain the GDML file.

4.1 GUIMesh

A geometry desired to be used in Geant4 simulation can be defined using C++ code and the passage and interaction of particles from that geometry can be simulated. However, this method is not useful for complex geometries. It is more useful to obtain the design of the geometry desired to be used in Geant4 simulation as a STEP file and to import the STEP file into Geant4. To obtain a STEP file, it is necessary to design in Computer-Aided Design (CAD) programs, but the STEP file must be converted to GDML format for it to be readable by Geant4. GUIMesh, a program that embeds the libraries of the open source CAD program FreeCAD, can be used to convert it to GDML format and have the geometry read by Geant4. Thanks to GUIMesh, material assignments can be made to each geometry in the STEP file. GUIMesh user interface is given in Figure 4.1. In Figure 4.1, the name of a representative object appears in the Volume List section on the middle screen, and the material assigned to the object appears in the Volume Properties section on the right screen [39][65].

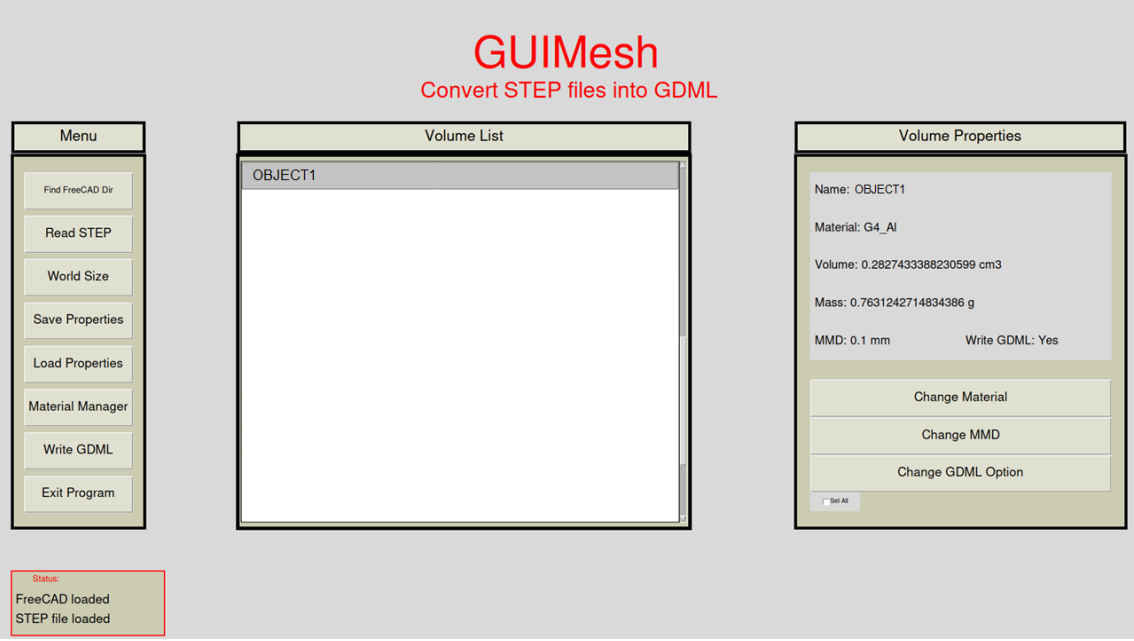

Figure 4.1 GUIMesh user interface.

Material assignments are made in Geant4 format. Ported version of GUIMesh from Python 2 to Python 3 was used. This version was taken from Middle East Technical University-IVMER (Space and Accelerator Technologies Research and Application Center) [39]. In this study, the satellite model was designed in AutoCAD and the created STEP file was imported into FreeCAD. The STEP file created in FreeCAD was loaded into GUIMesh and the material was assigned to each object in the model.

4.2 Model Satellite Structure

The estimated satellite model design was made using AutoCAD to be used in the Geant4 simulation. An image of the model satellite is given in Figure 4.2. The predicted satellite model was designed as a cube and its edge length is 2.5 m. The length of the antenna on the model satellite is 1.5 meters. The distance of the solar panel to the model satellite is 1 meter and its dimensions are $2.25m \times 2.25m$.

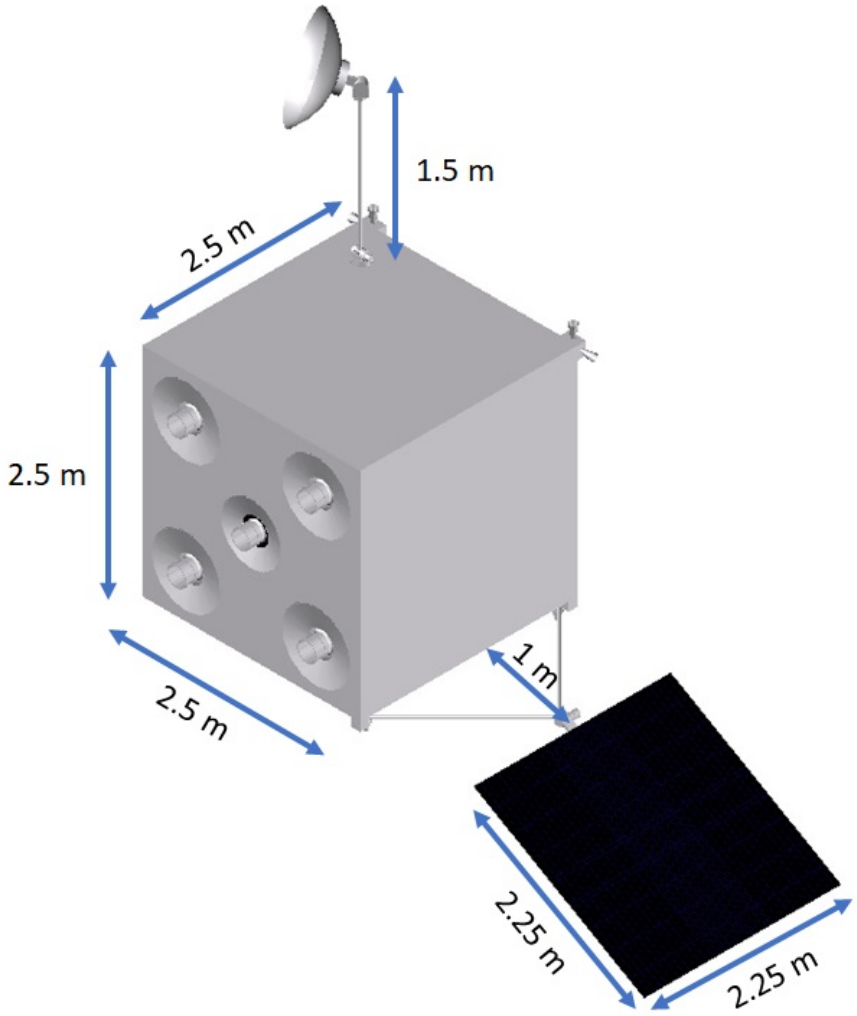

Figure 4.2 Dimensions of model satellite.

The volume of $90cm \times 249.6cm \times 249.6cm$ above the section where all the tanks are located was left empty for the payload. All the walls of the model satellite were made of aluminum with a thickness of 2 mm. The reason why all the walls of the satellite are modeled at this thickness is that the same selection was made in the simulation studies for the Chandrayaan-1 mission [66]. Figure 4.3 shows a view of the estimated satellite model from a different angle. The material of the arms of the solar panel and the antenna was chosen as aluminum.

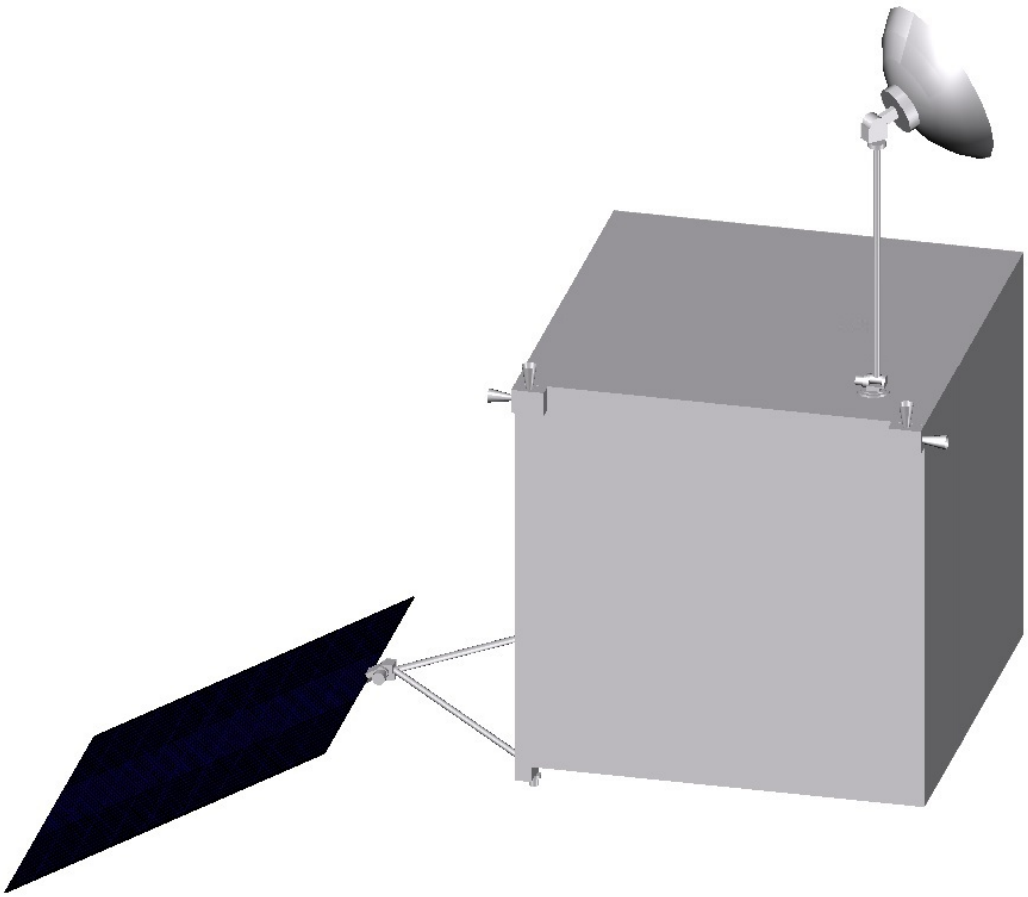

Figure 4.3 Different view of the model satellite.

The model satellite has chemical propulsion tanks and a hybrid propulsion system [58]. The propulsion system of the model satellite is given in Figure 4.4. In the design of the chemical propulsion system, the design of the fuel tank, oxidizer tank, and ignition system were not modeled separately. A tank with a length of 145 cm and a radius of 45 cm was made to represent the chemical propulsion system. The wall thickness of the tank is 2 mm, and the material is aluminum. The nozzle length is 20 cm, the radius is 12 cm, and it is designed as stainless steel [67].

The reason for modeling the hybrid propulsion system of the model satellite is to ensure that the interior of the model satellite is as similar as possible to the satellite to be used in the mission. Because the more similar the modeled satellite is to the satellite to be used in the mission, the more realistic the result obtained with Geant4 simulation will be.

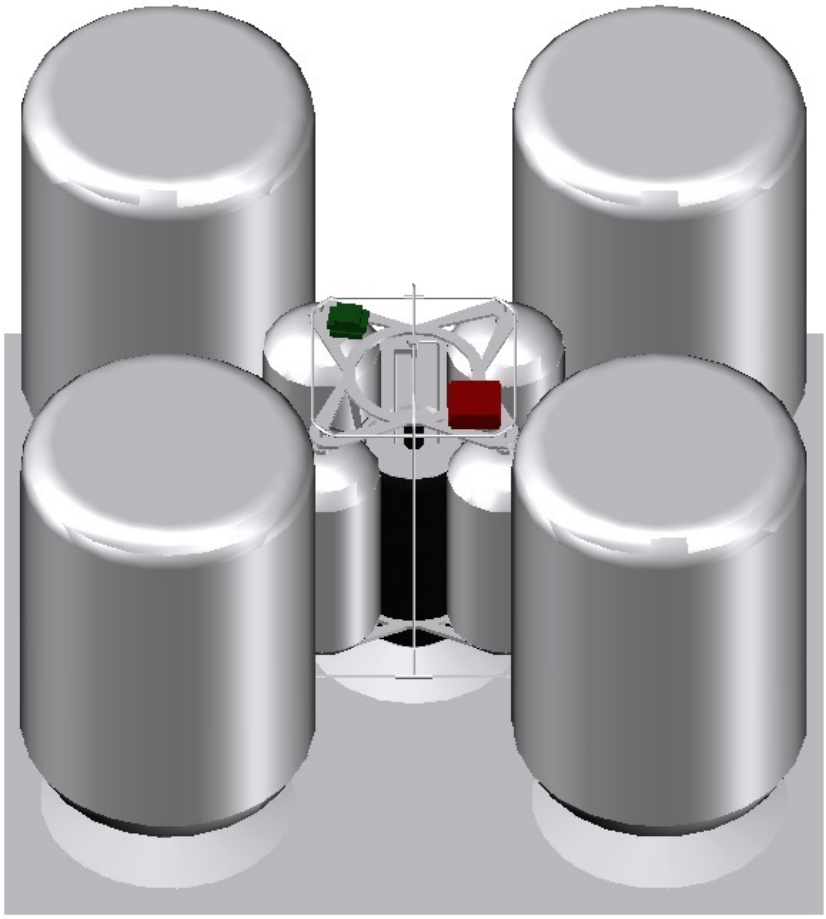

Figure 4.4 Chemical and hybrid propulsion systems of the model satellite.

The hybrid propulsion system consists of 1 engine and 4 oxidizer tanks. An aluminum structure with a thickness of 2 mm was made to represent the engine of the hybrid propulsion system. It is equipped with 1 mm thick carbon fiber [68][69]. The length of the structure with the engine is 73 cm and the radius is 19 cm. The oxidizer tanks are designed in aluminum with a length of 81 cm, a radius of 18 cm, and a wall thickness of 2 mm. The thickness of the upper and lower skeletons is 1.5 cm and is designed as aluminum material. The pipes are made of aluminum. The diameter of the pipes is 1 cm, and the wall thickness is 2 mm. The picture of the modeled hybrid propulsion system is given in Figure 4.5 and 4.6.

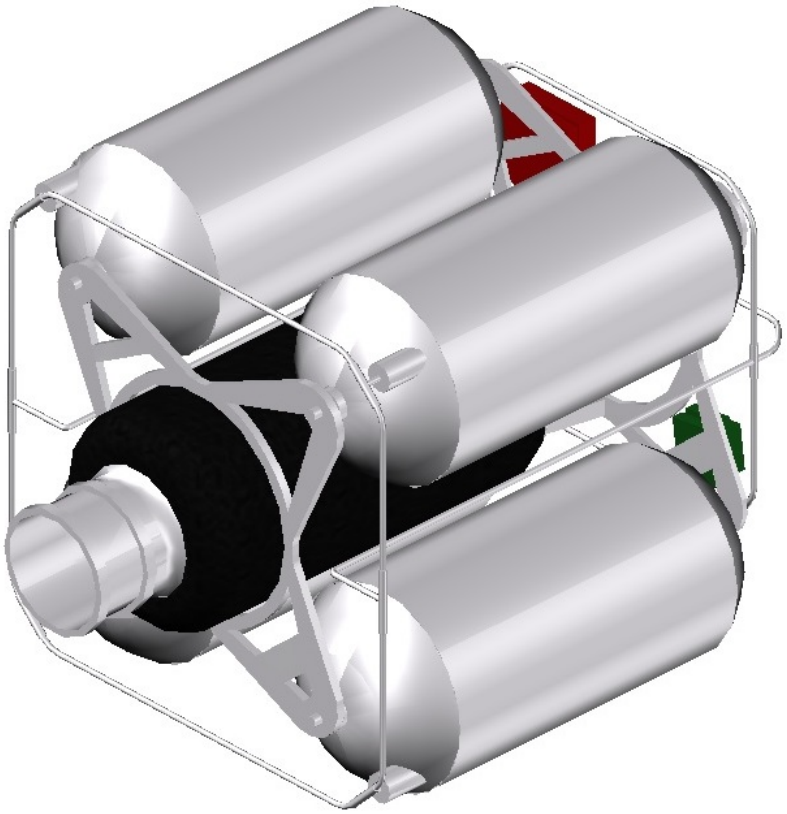

Figure 4.5 Hybrid propulsion system of the model satellite.

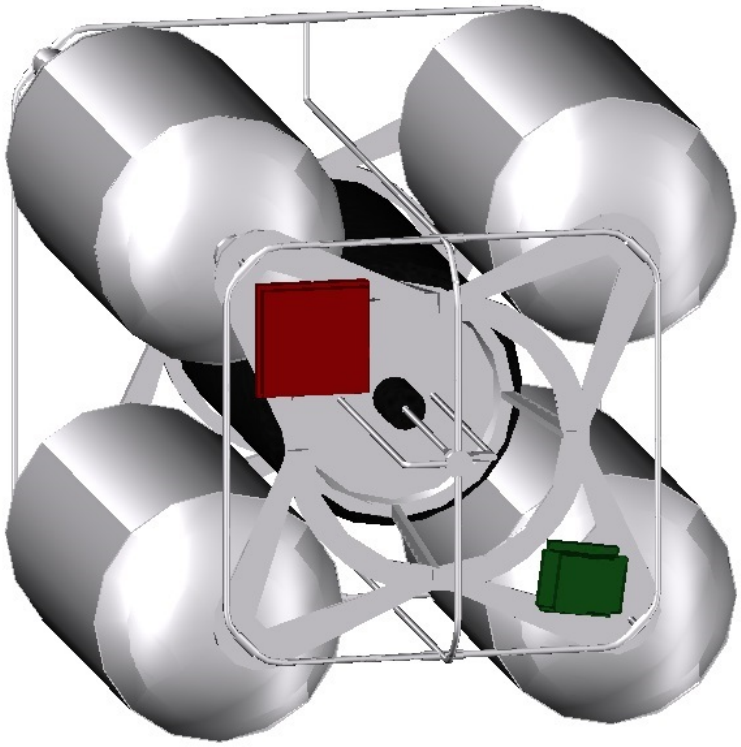

Figure 4.6 A view of the hybrid propulsion system of the model satellite from a different angle.

5
SPACE ENVIRONMENT ESTIMATION FOR THE MISSION

The data of the space environment in which the spacecraft will be in the Turkish Lunar Mission were obtained in SPENVIS. The data was obtained by dividing the mission into two parts in SPENVIS. The first part of the estimated mission profile consists of the Earth Bound Orbits + Lunar Transfer Trajectory and the second part of the estimated mission profile consists of Lunar Orbits. In both parts, the dates are the same as the dates in the predicted mission profile. The images of trajectories obtained from SPENVIS for the two parts of the mission given in Section 3 are given in Figure 5.1 and Figure 5.2. While obtaining data from SPENVIS for the second part of the mission, Initial Lunar Orbit (ILO), Lunar Orbit (LO), and Operational Lunar Orbit (OLO) around the Moon are not defined in SPENVIS. Instead, data was collected for a circular orbit at the Moon's average distance from the Earth, 384,400 km. This situation is also described in Section 3.1.3. Figure 5.1 shows the altitude-dependent graph obtained from SPENVIS for the estimated trajectory that the spacecraft will be on the first part of the mission. In Figure 5.2, the altitude-dependent graph obtained from SPENVIS is given for the circular trajectory in the second part of the mission. Particle flux-energy and fluence-energy graphs from SPENVIS are given in Section 5.1 for the first part of the mission, and in Section 5.2 for the second part of the mission. For the first part of the mission, sees the effects of trapped particles, solar particles, and galactic cosmic ray particles, while the second part of the mission sees the effects of solar particles and galactic cosmic ray particles. The reason why the effect of the trapped particles is not seen in the second part of the mission is that the effect of the Van Allen belts ends long before the Moon distance. Details about the graphics are given in the relevant sections.

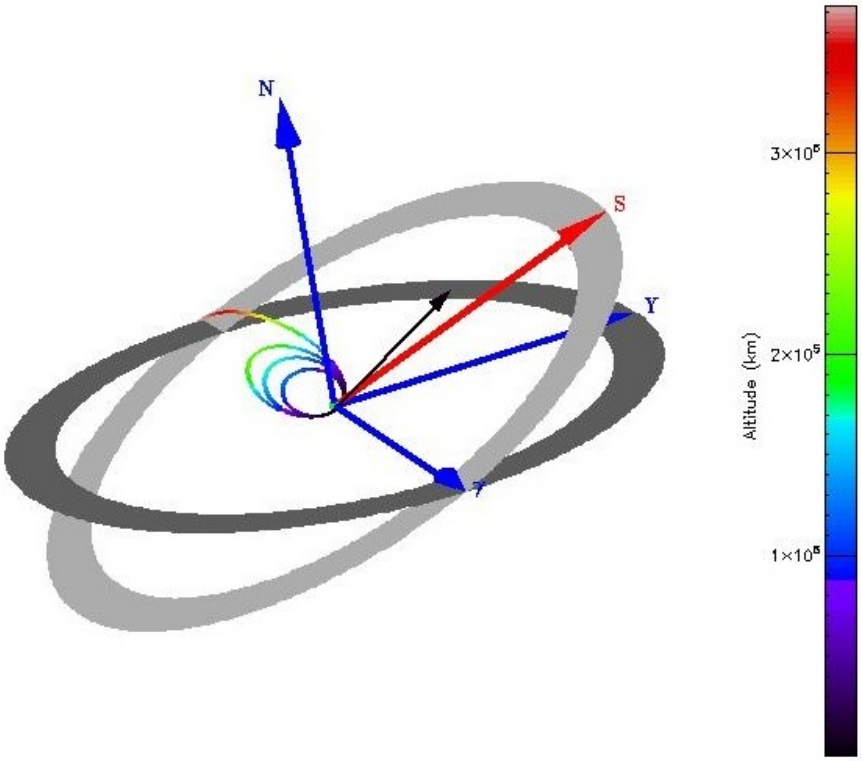

Figure 5.1 Earth bound orbits and lunar transfer trajectory in SPENVIS. The colored bar on the right gives the altitude. The altitude increases as the color approaches red.

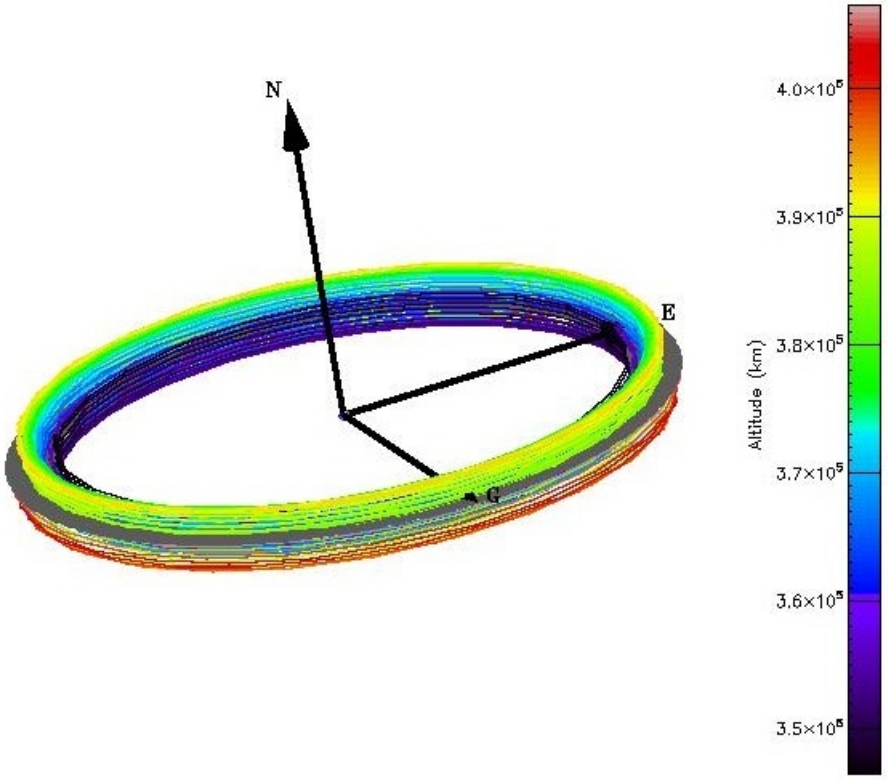

Figure 5.2 Lunar orbits in SPENVIS. The colored bar on the right gives the altitude. The altitude increases as the color approaches red.

5.1 Data for the Earth Bound Orbits and Lunar Transfer Trajectory

Particle flux-energy and fluence-energy graphs from SPENVIS are given below for the first part of the mission. Graphs of trapped particles are given in Section 5.1.1, graphs of solar particles are given in Section 5.1.2, graphs of galactic cosmic ray particles are given in Section 5.1.3.

5.1.1 Trapped Particles Data

For the first part of the mission, the spacecraft will pass through the Van Allen belts according to the predicted orbit and for that reason, data for trapped particles were obtained from SPENVIS. Energy-Integral Flux-Differential Flux graphs of trapped protons and trapped electrons are given in Figure 5.3 and Figure 5.4. One of the factors affecting the data in the graphs is the mission trajectory. Another factor that affects the data in the graphs is the duration of the mission. Since the spacecraft will not be in the inner and outer belts for a long time the effect of trapped particles on the spacecraft will be as little as possible. Due to the trajectory, in the trapped particle graphs obtained from SPENVIS, the integral flux is less than the differential flux at low energies, but the integral flux exceeds the differential flux at high energies (Section 5.1.1). This is an expected situation. Because when we have very high differential flux values at low energies and try to integrate over these values, the value of the integral may be smaller than the differential value.

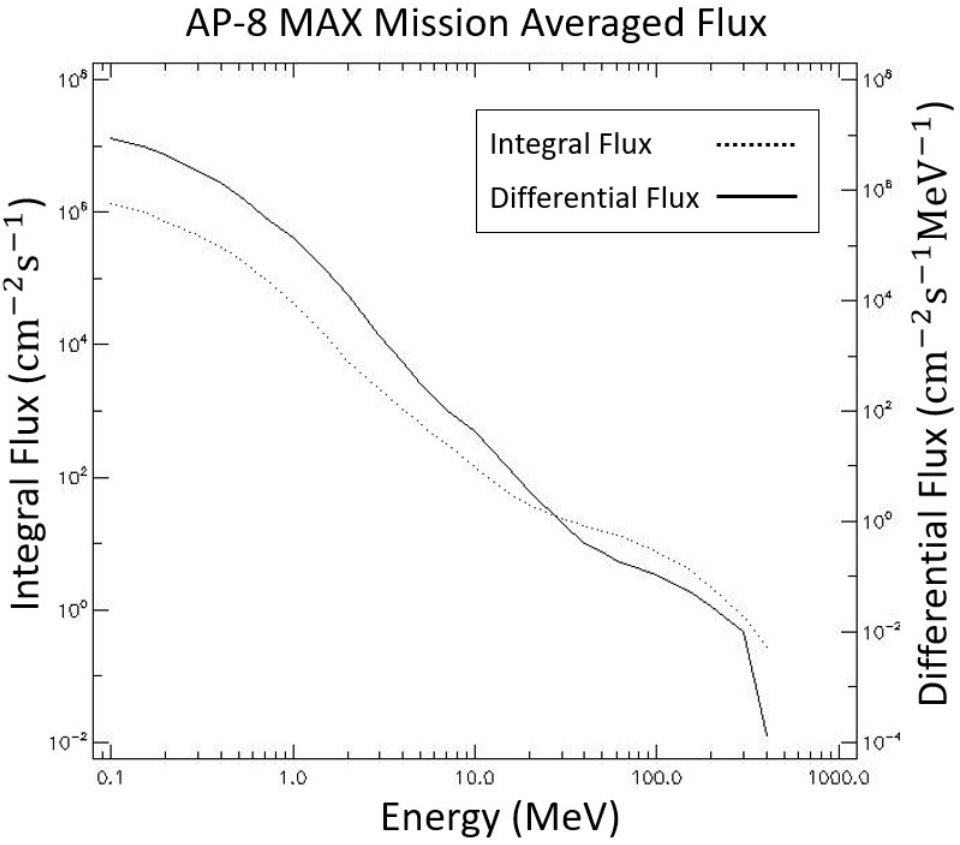

Figure 5.3 Trapped protons Energy-Differential Flux-Integral Flux graph.

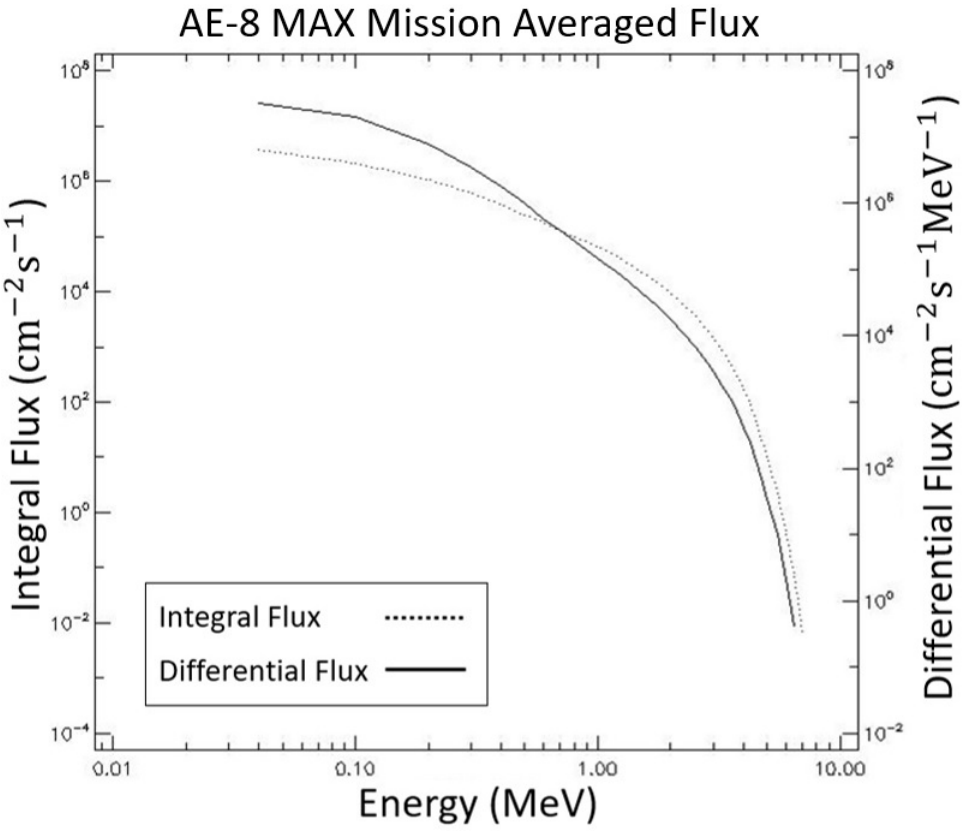

Figure 5.4 Trapped electrons Energy-Differential Flux-Integral Flux graph.

5.1.2 Solar Particles Data

The graphs Figure 5.5 through Figure 5.14 are solar particle graphs obtained from SPENVIS for the first part of the mission. It was mentioned in Chapter 3 that the mission date was set for 13 June 2023 in the estimated orbit simulations. As this date is close to 2025, the solar maximum year of the solar cycle 25, the fluxes of the solar particles are high. The particles chosen to study the solar particle effect are hydrogen, helium, carbon, nitrogen, oxygen, neon, magnesium, silicon, sulfur, and iron. These particles were selected according to their abundance ratio [70][71]. In the solar particle graphs, except for the hydrogen graph in the first part of the mission, the other graphs show that the integral fluence is more than the differential fluence. Especially in terms of mission date, the effect of solar particles was expected to be high, so it is expected that the integral fluence is more than the differential fluence. However, it is thought that the protons in the Van Allen belts cause the integral flux to be higher than the differential flux in the hydrogen graph.

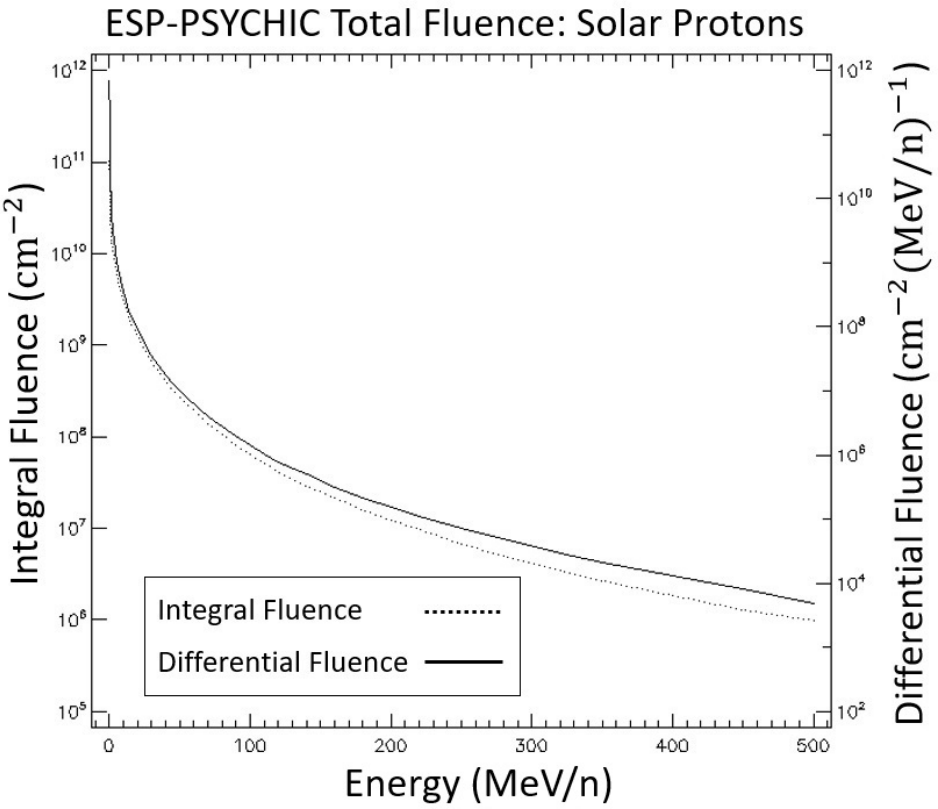

Figure 5.5 Solar Hydrogen Energy-Differential Fluence-Integral Fluence graph.

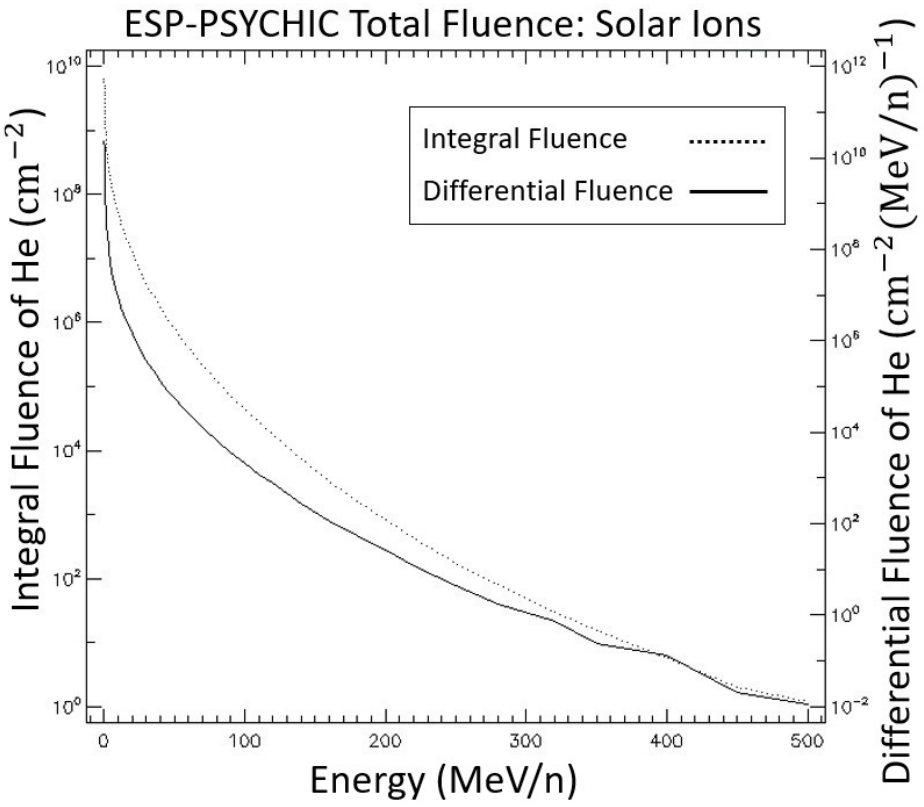

Figure 5.6 Solar Helium Energy-Differential Fluence-Integral Fluence graph.

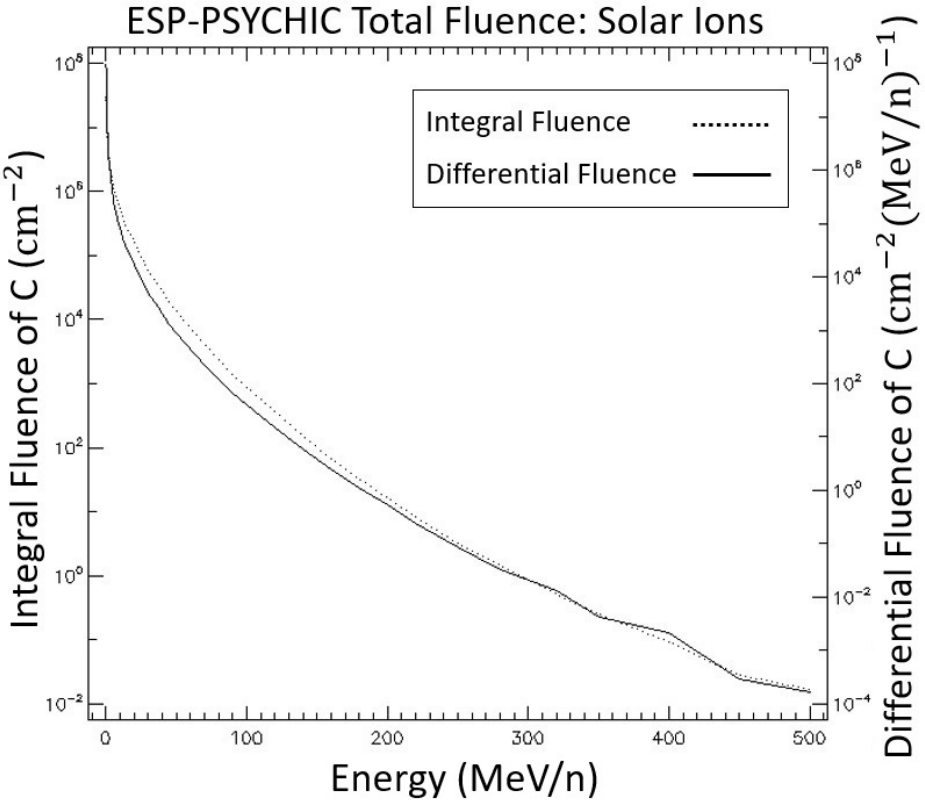

Figure 5.7 Solar Carbon Energy-Differential Fluence-Integral Fluence graph.

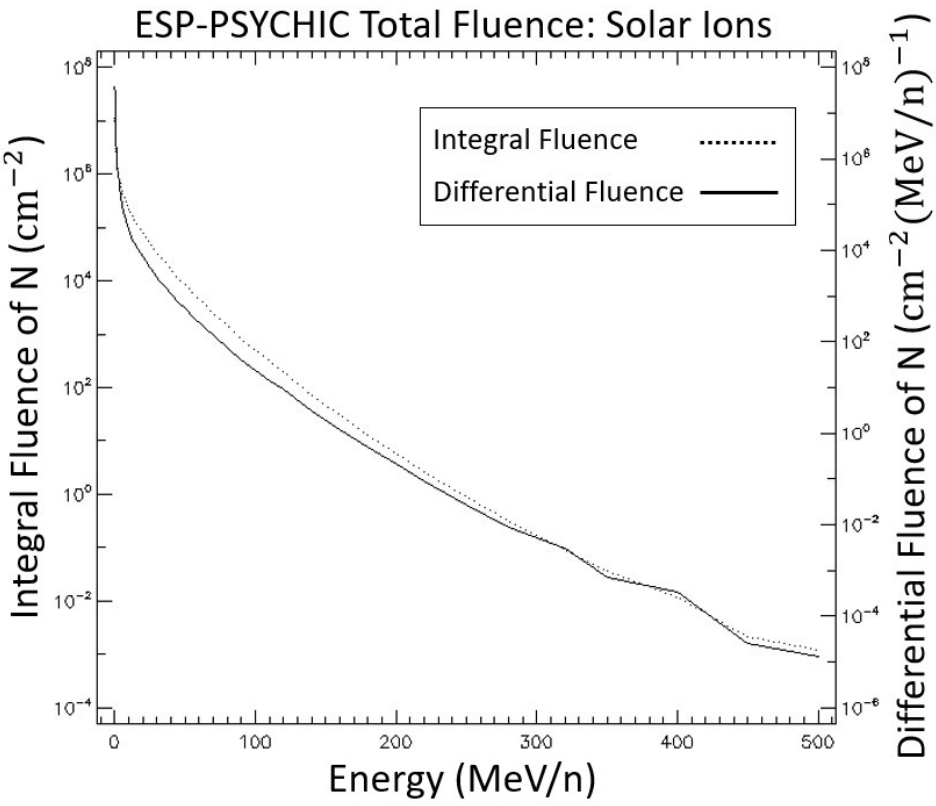

Figure 5.8 Solar Nitrogen Energy-Differential Fluence-Integral Fluence graph.

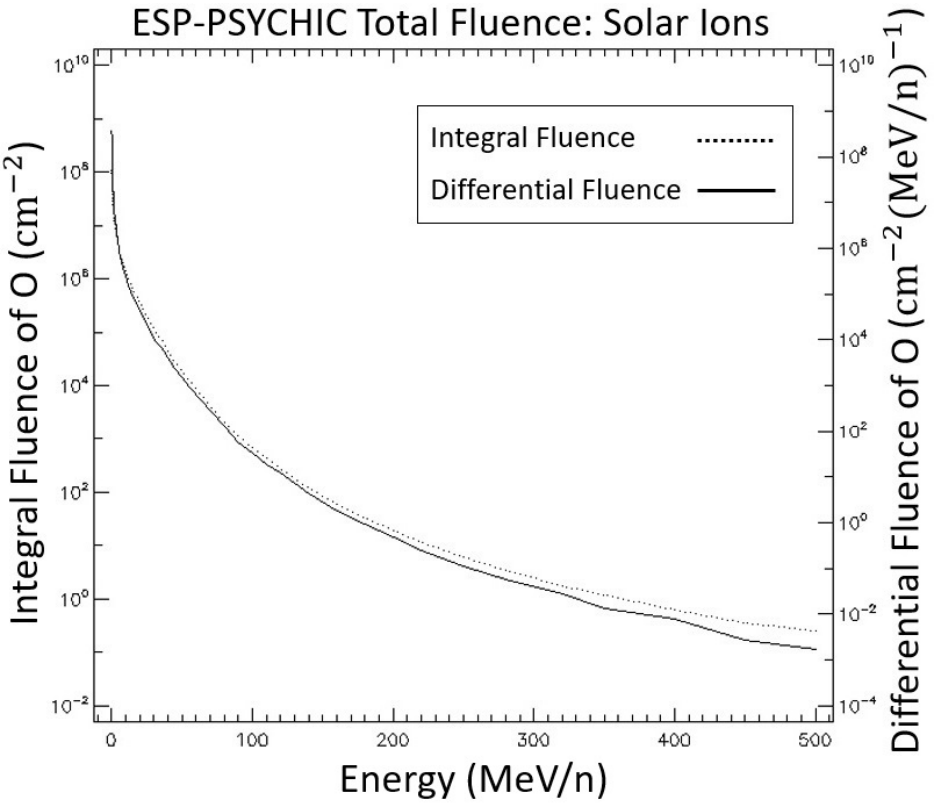

Figure 5.9 Solar Oxygen Energy-Differential Fluence-Integral Fluence graph.

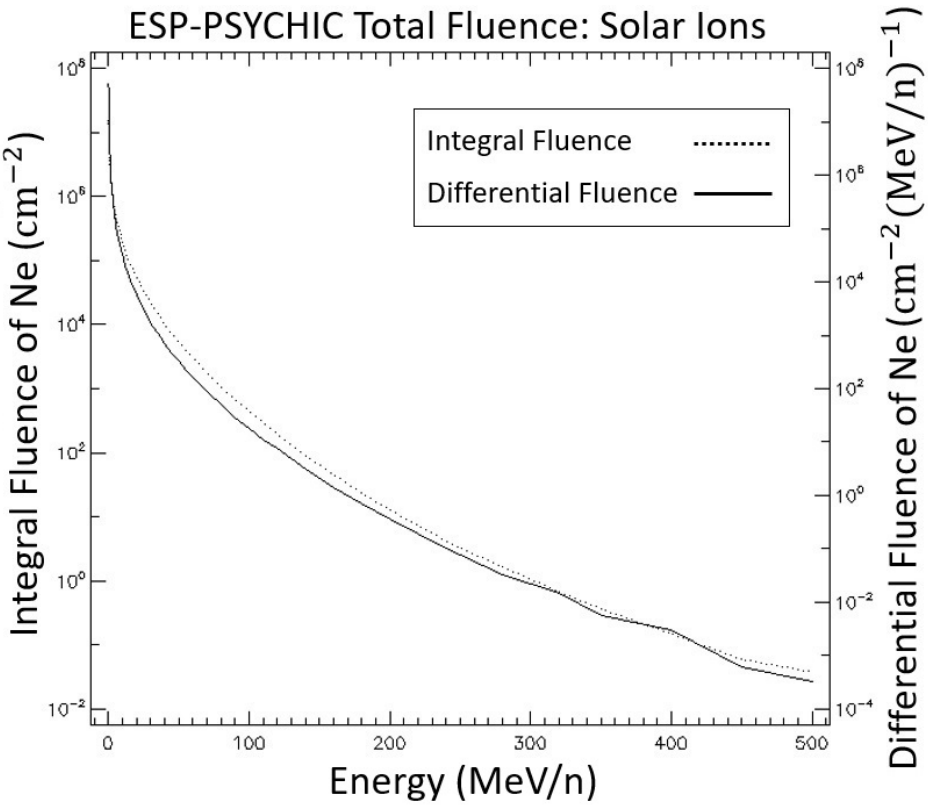

Figure 5.10 Solar Neon Energy-Differential Fluence-Integral Fluence graph.

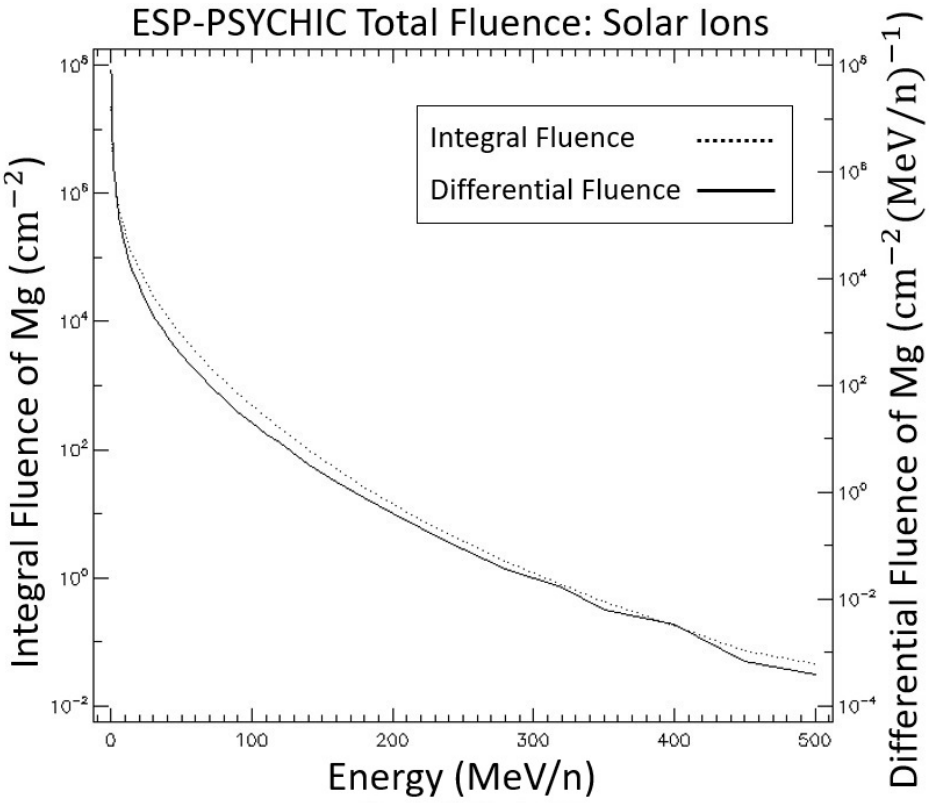

Figure 5.11 Solar Magnesium Energy-Differential Fluence-Integral Fluence graph.

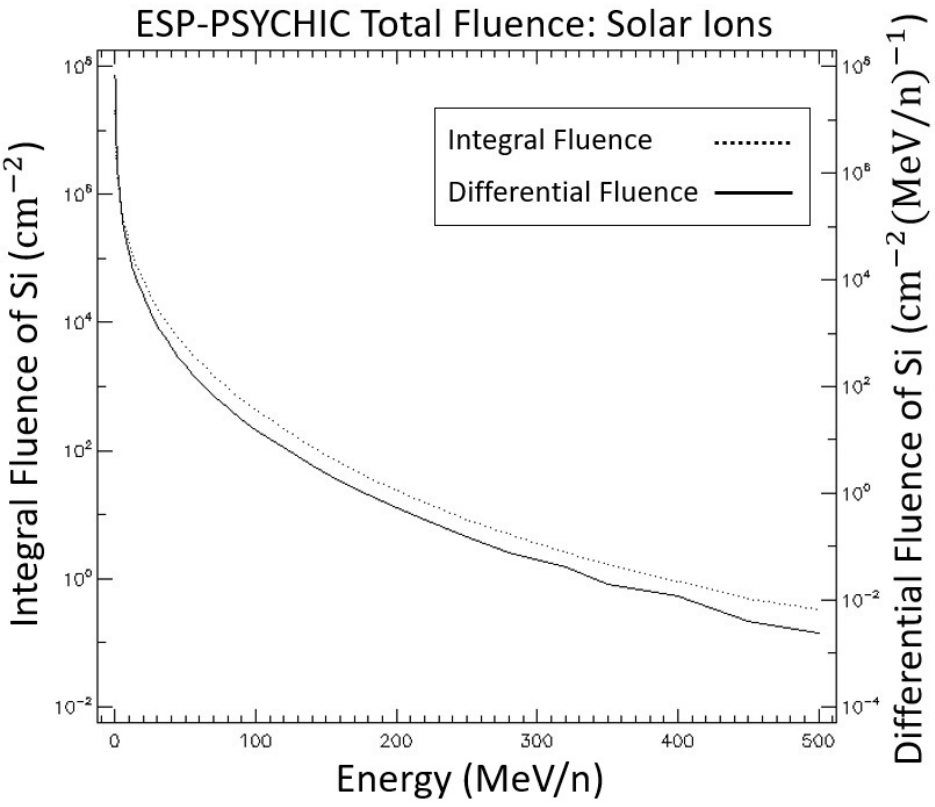

Figure 5.12 Solar Silicon Energy-Differential Fluence-Integral Fluence graph.

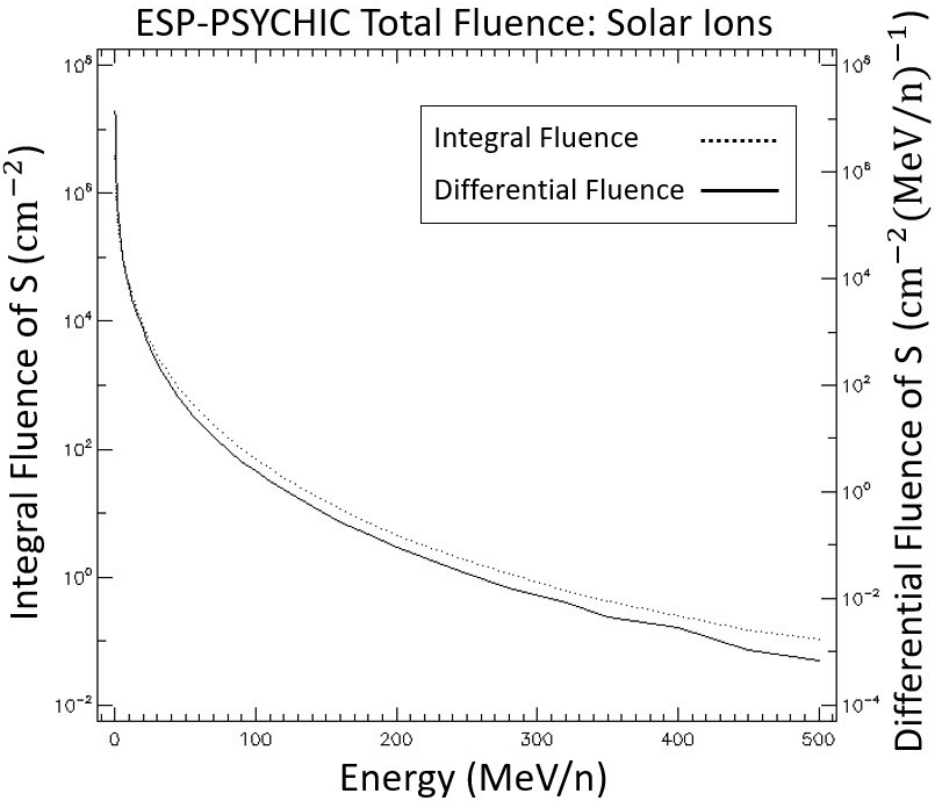

Figure 5.13 Solar Sulfur Energy-Differential Fluence-Integral Fluence graph.

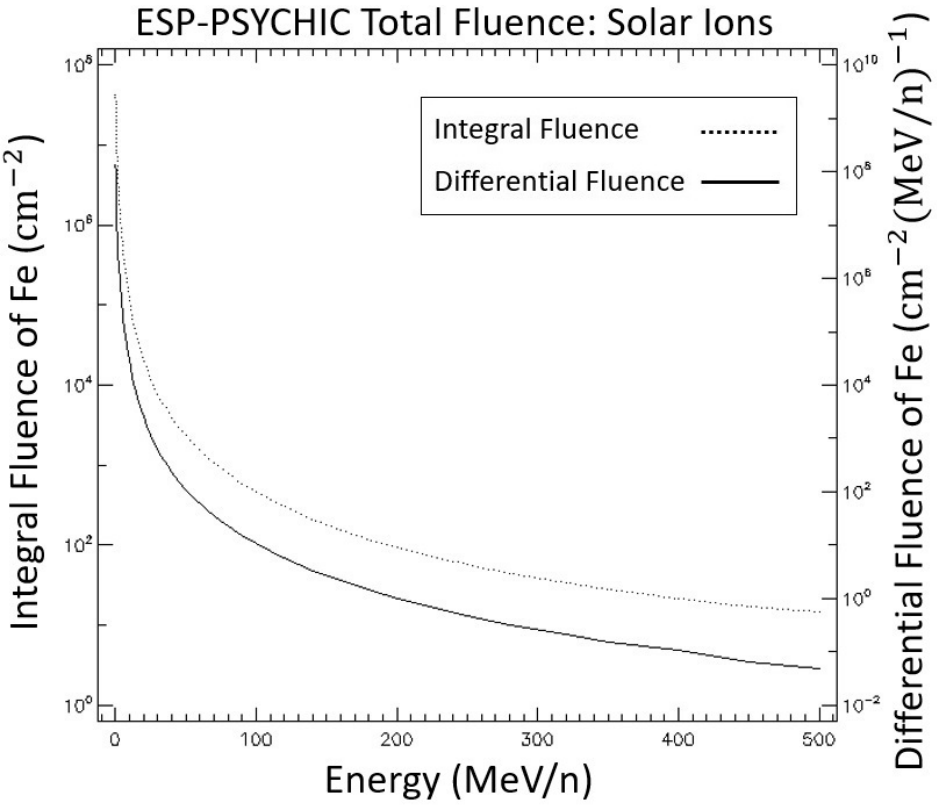

Figure 5.14 Solar Iron Energy-Differential Fluence-Integral Fluence graph.

5.1.3 Galactic Cosmic Ray Data

For the first part of the mission, galactic cosmic ray data are given in all flux-energy graphs from Figure 5.15 to Figure 5.26. The particles chosen to study the galactic cosmic ray effect are hydrogen, helium, lithium, beryllium, boron, carbon, nitrogen, oxygen, neon, magnesium, silicon, and iron. These particles were selected according to their abundance ratio [28]. Although the exact cause of differential flux breaking points in graphs is not known clearly, but it is thought that these breaking points are due to mission segments.

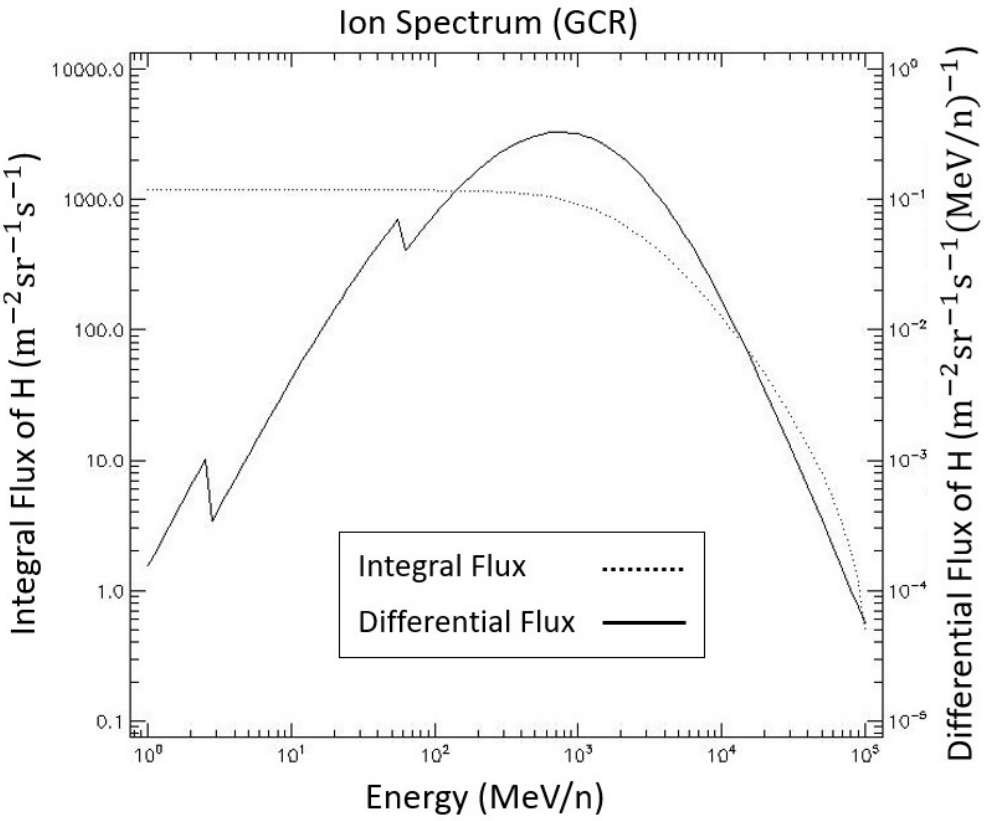

Figure 5.15 GCR Hydrogen Energy-Differential Flux-Integral Flux graph.

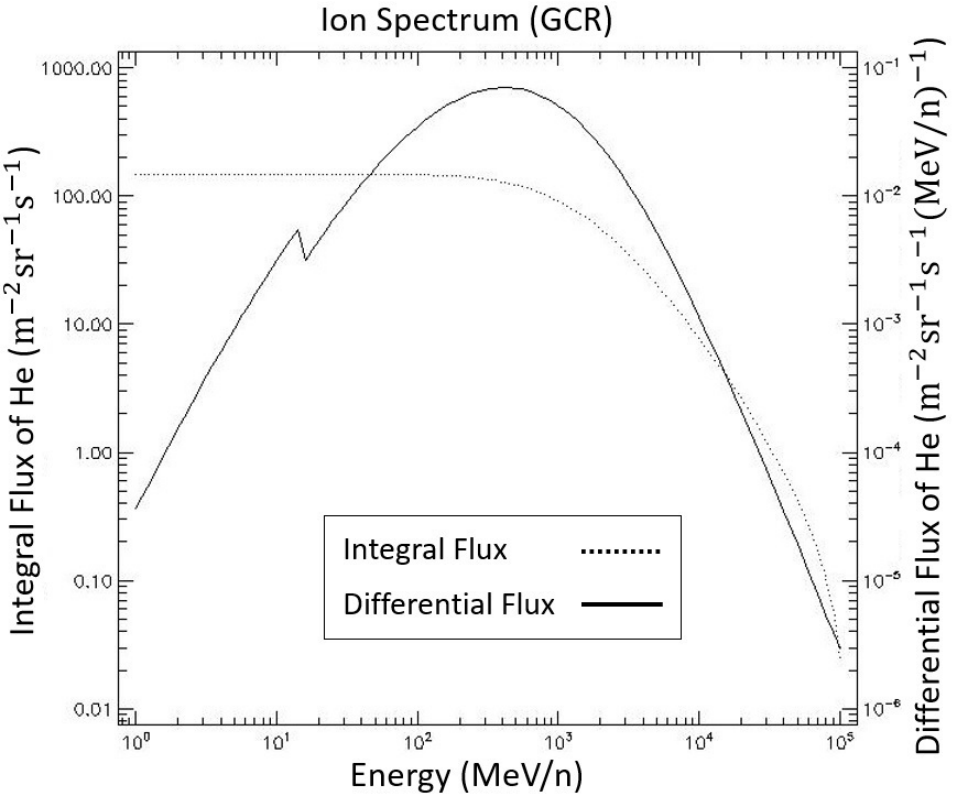

Figure 5.16 GCR Helium Energy-Differential Flux-Integral Flux graph.

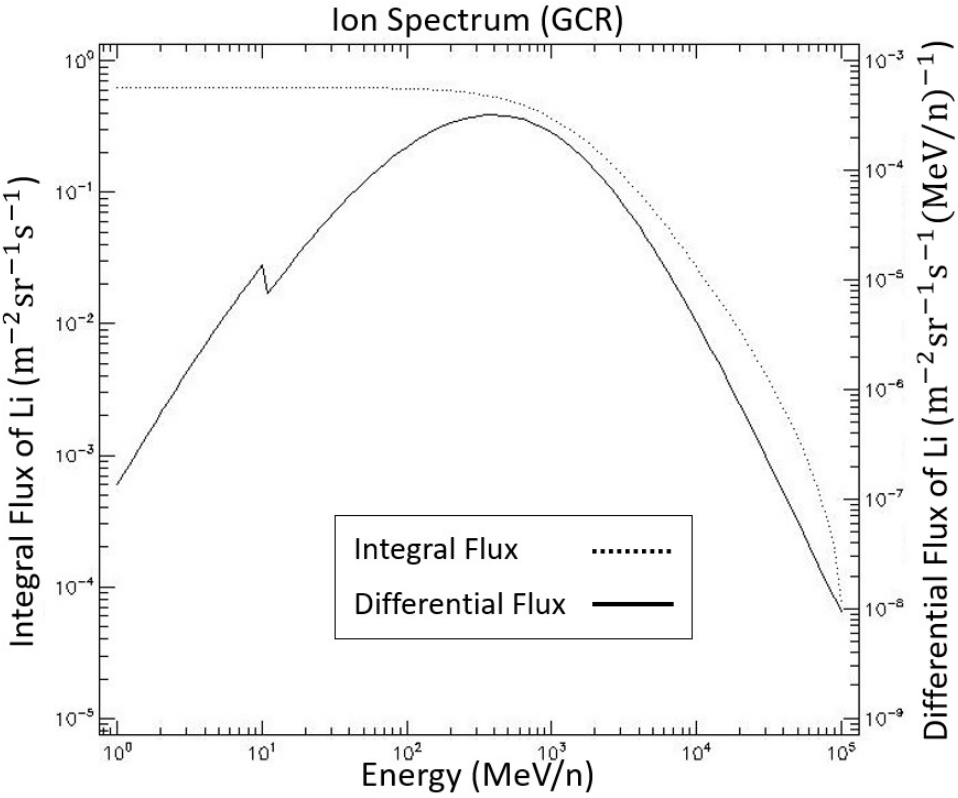

Figure 5.17 GCR Lithium Energy-Differential Flux-Integral Flux graph.

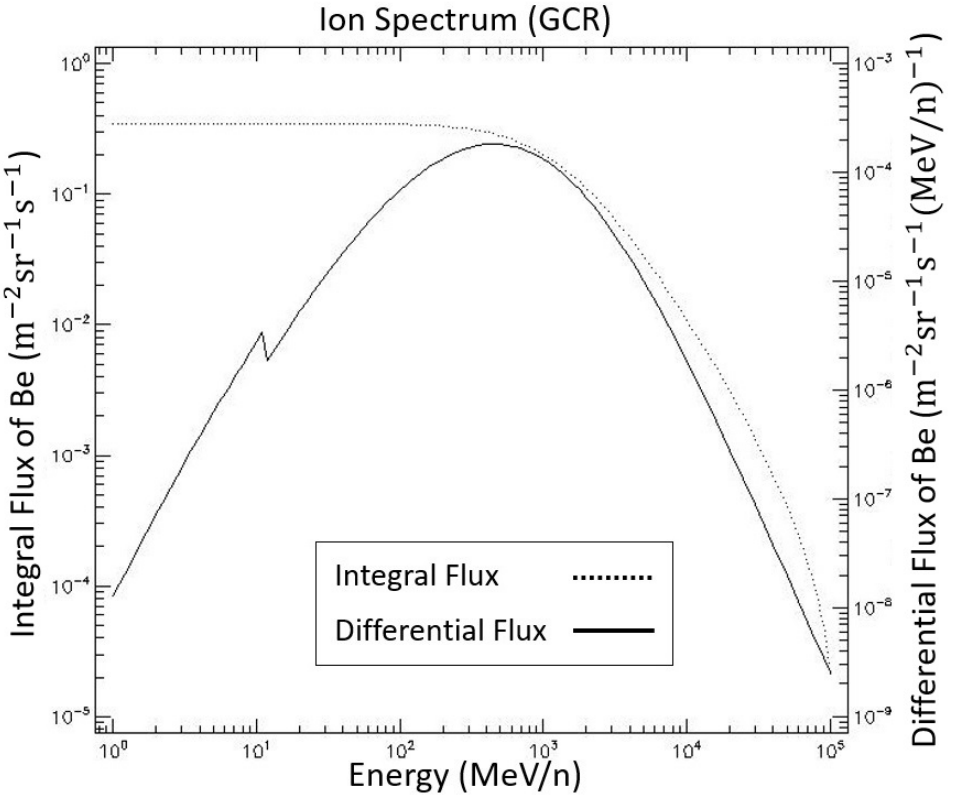

Figure 5.18 GCR Beryllium Energy-Differential Flux-Integral Flux graph.

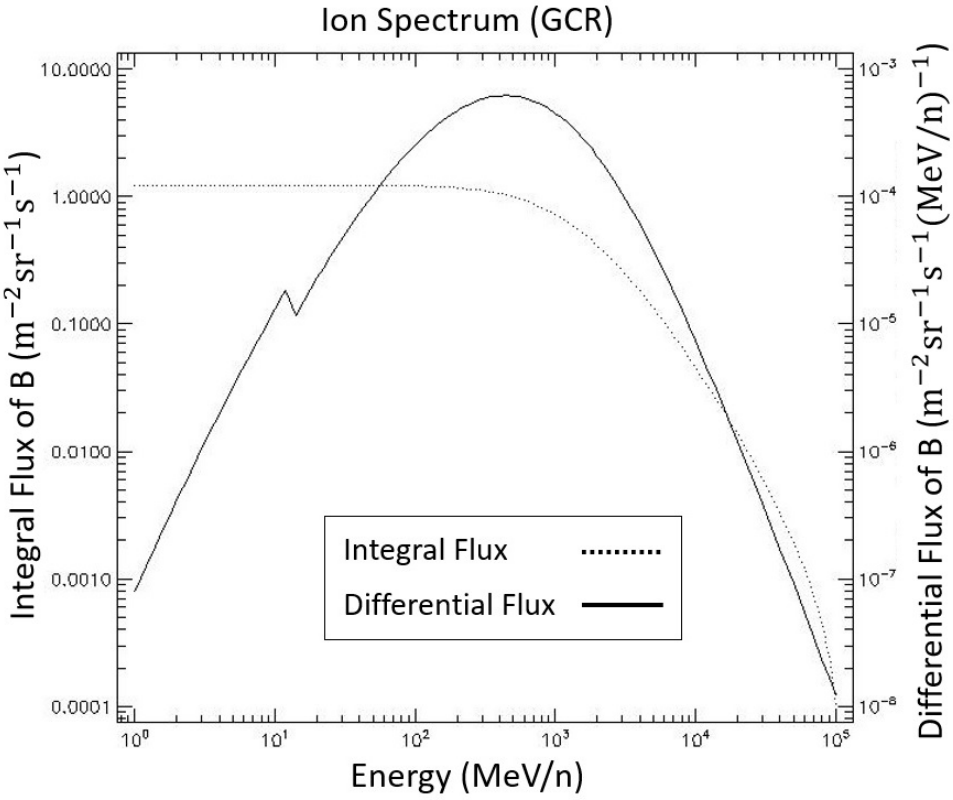

Figure 5.19 GCR Boron Energy-Differential Flux-Integral Flux graph.

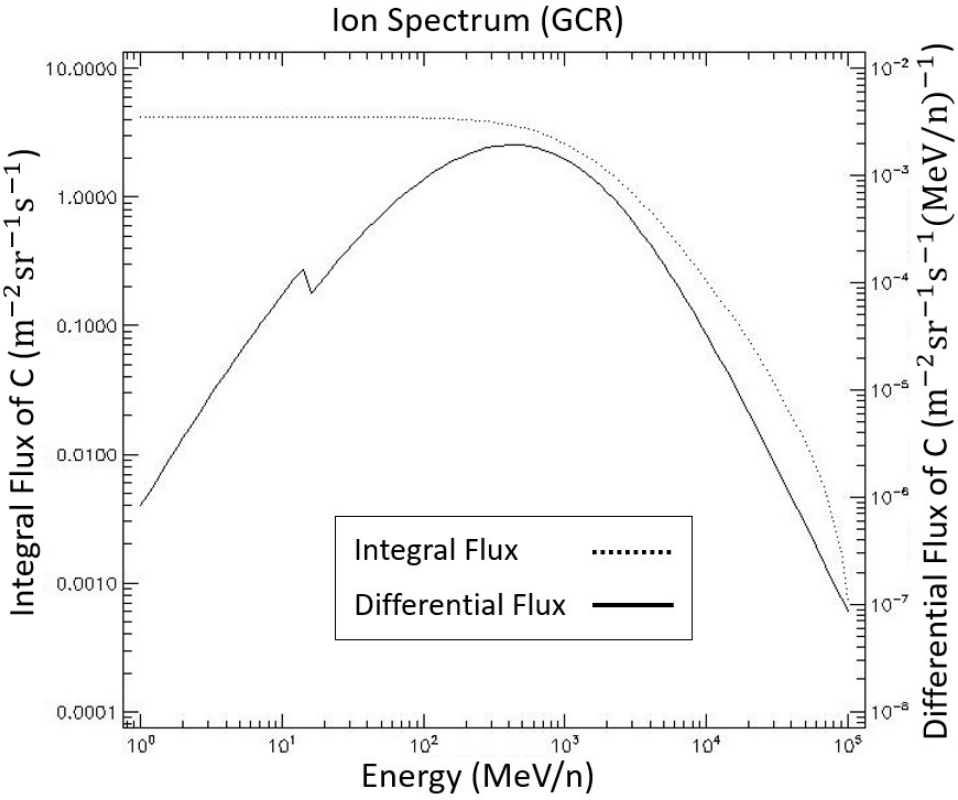

Figure 5.20 GCR Carbon Energy-Differential Flux-Integral Flux graph.

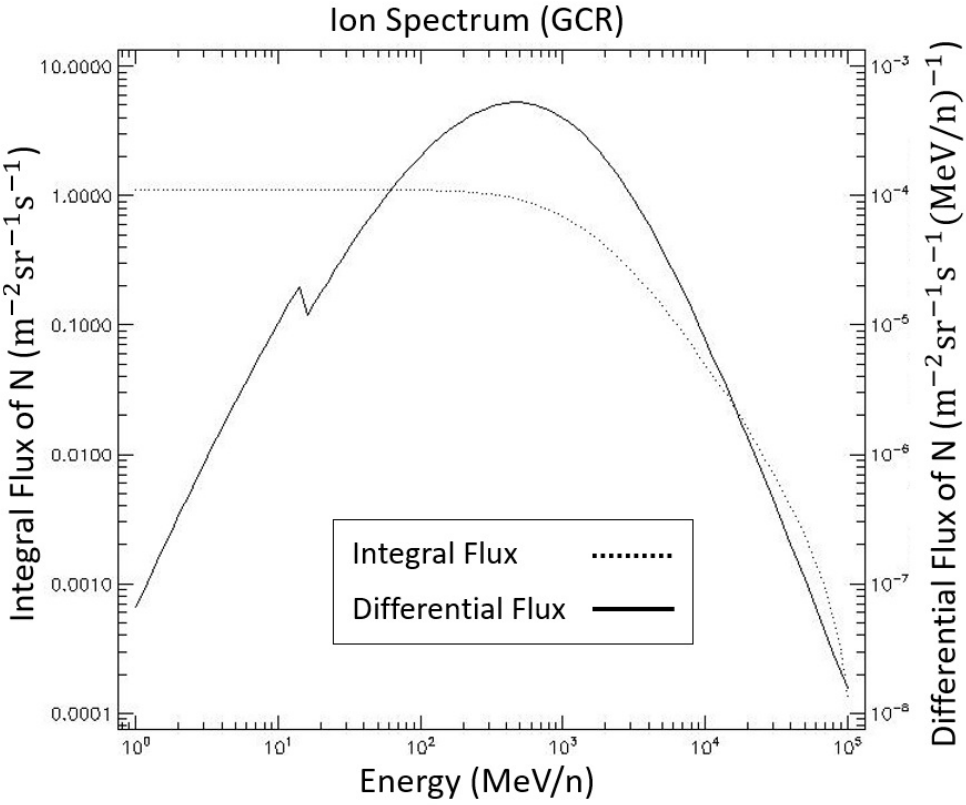

Figure 5.21 GCR Nitrogen Energy-Differential Flux-Integral Flux graph.

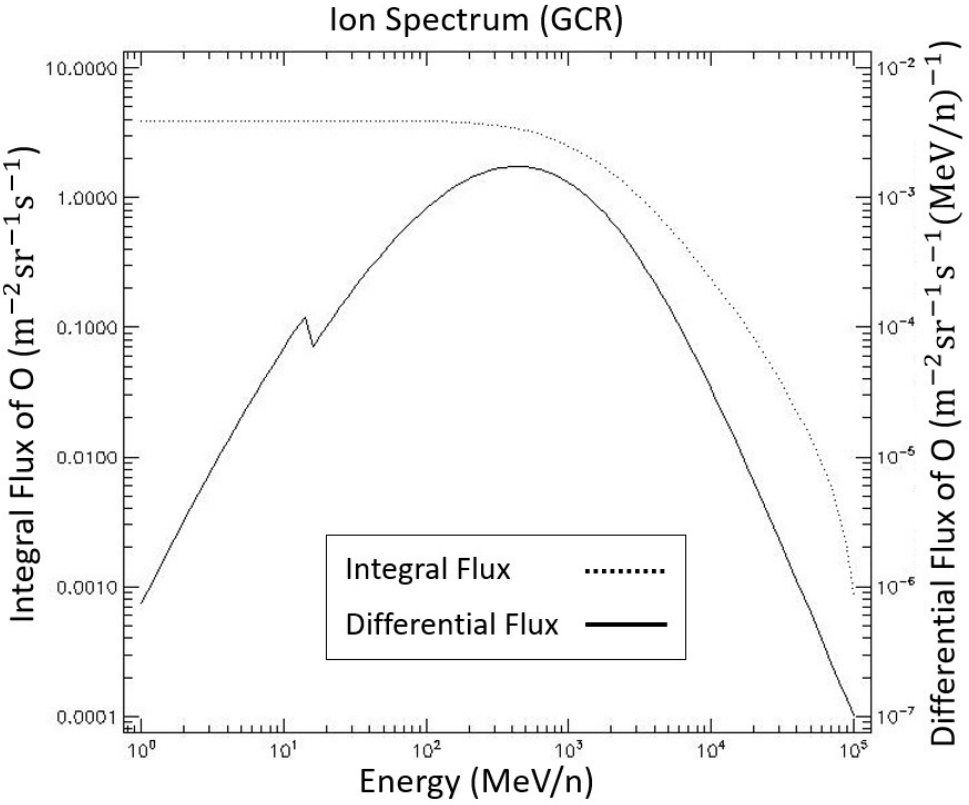

Figure 5.22 GCR Oxygen Energy-Differential Flux-Integral Flux graph.

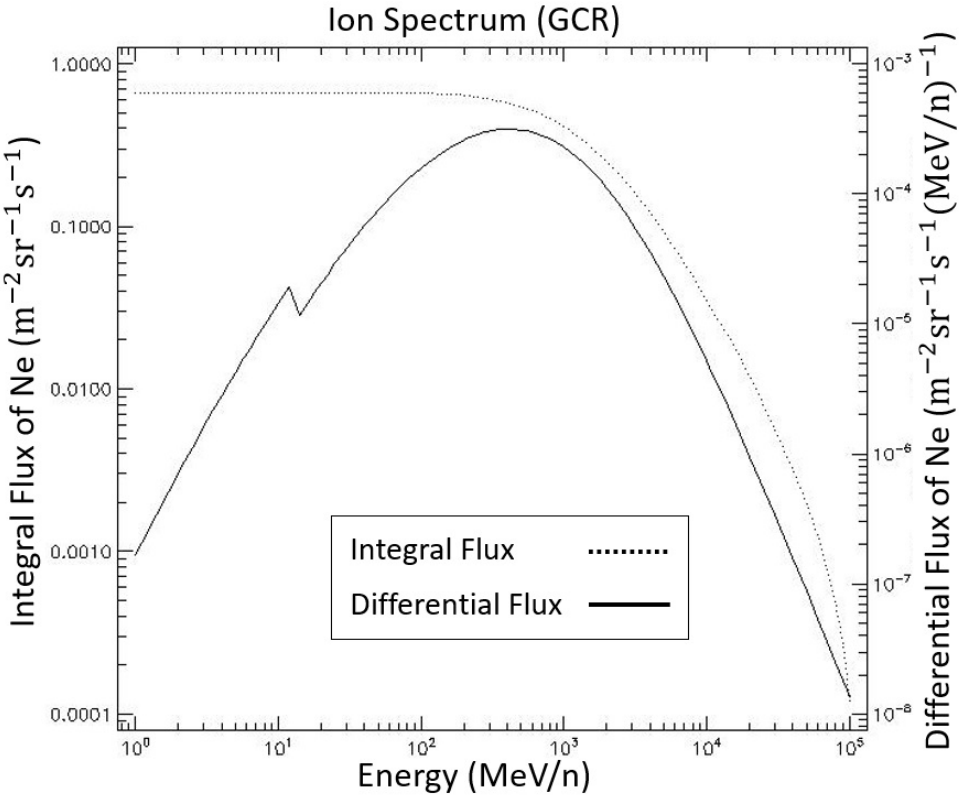

Figure 5.23 GCR Neon Energy-Differential Flux-Integral Flux graph.

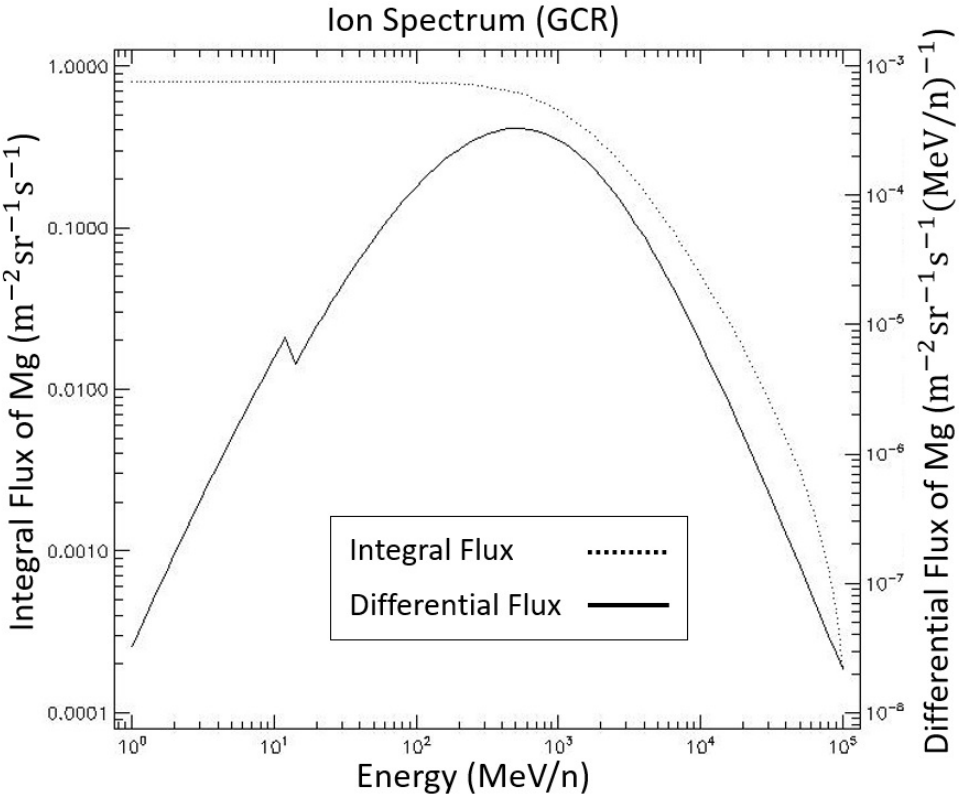

Figure 5.24 GCR Magnesium Energy-Differential Flux-Integral Flux graph.

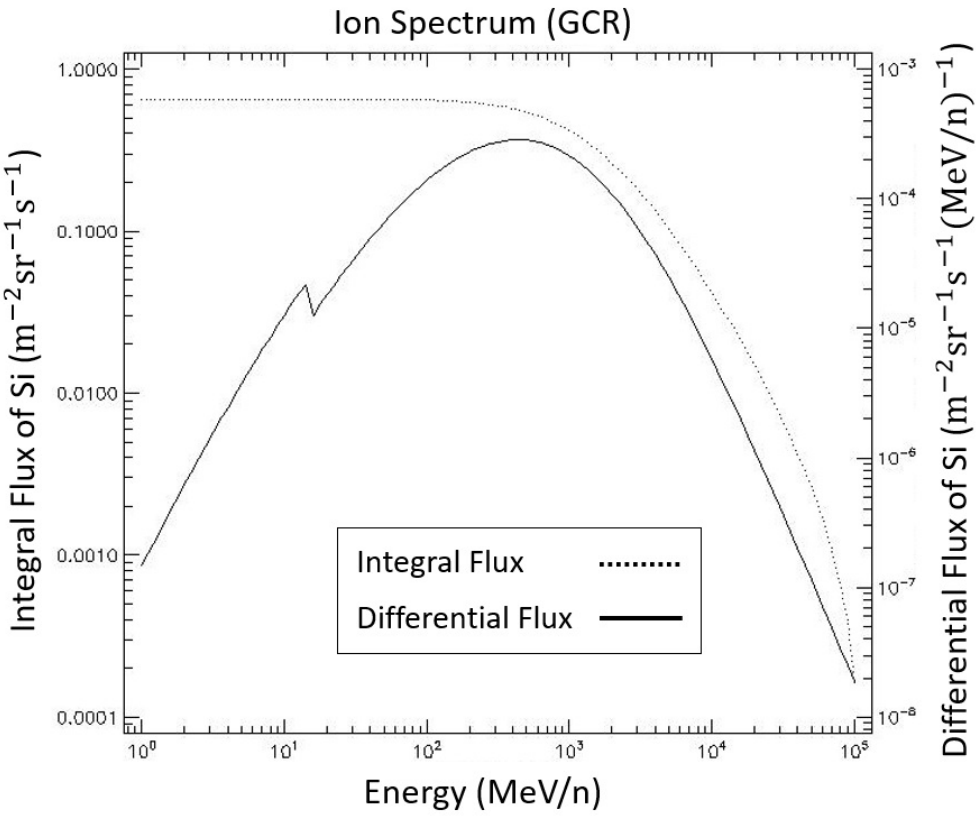

Figure 5.25 GCR Silicon Energy-Differential Flux-Integral Flux graph.

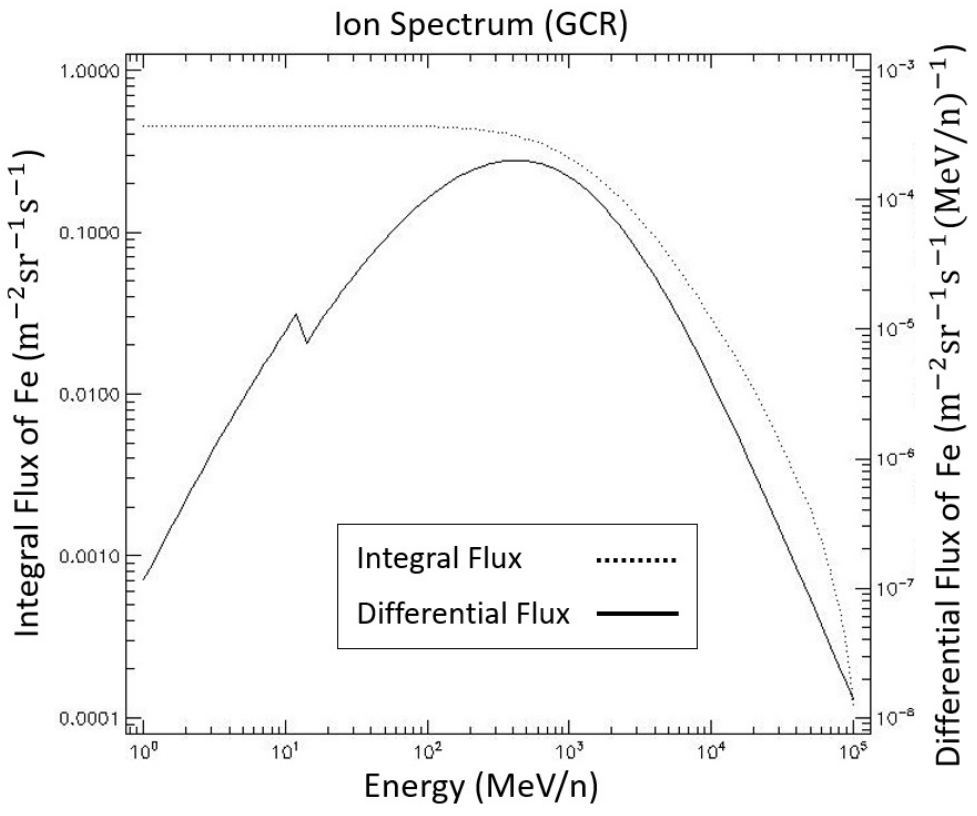

Figure 5.26 GCR Iron Energy-Differential Flux-Integral Flux graph.

5.2 Data for Lunar Orbits

5.2.1 Solar Particles Data

For the second part of the mission, all the graphs, from Figure 5.27 to Figure 5.36 gives information about fluence and energy of solar particles. Data obtained from SPENVIS and these particles are hydrogen, helium, carbon, nitrogen, oxygen, neon, magnesium, silicon, sulfur, and iron, as in Section 5.1.2. These solar particles were selected according to their abundance ratio [70][71]. In this part, as mentioned in Chapter 3 and Section 5.1.2, solar particle fluence expected to be higher because of the mission date. Due to predicted mission profile, satellite will be on Lunar Orbits. When particle fluence is getting higher, the integral fluence is getting higher than differential fluence. That's why in the solar particle graphs, except for the silicon in the second part of the mission, the integral fluence is more than the differential fluence at high energy. It is not known why the integral flux in the silicon graph is less than the differential flux as the energy increases.

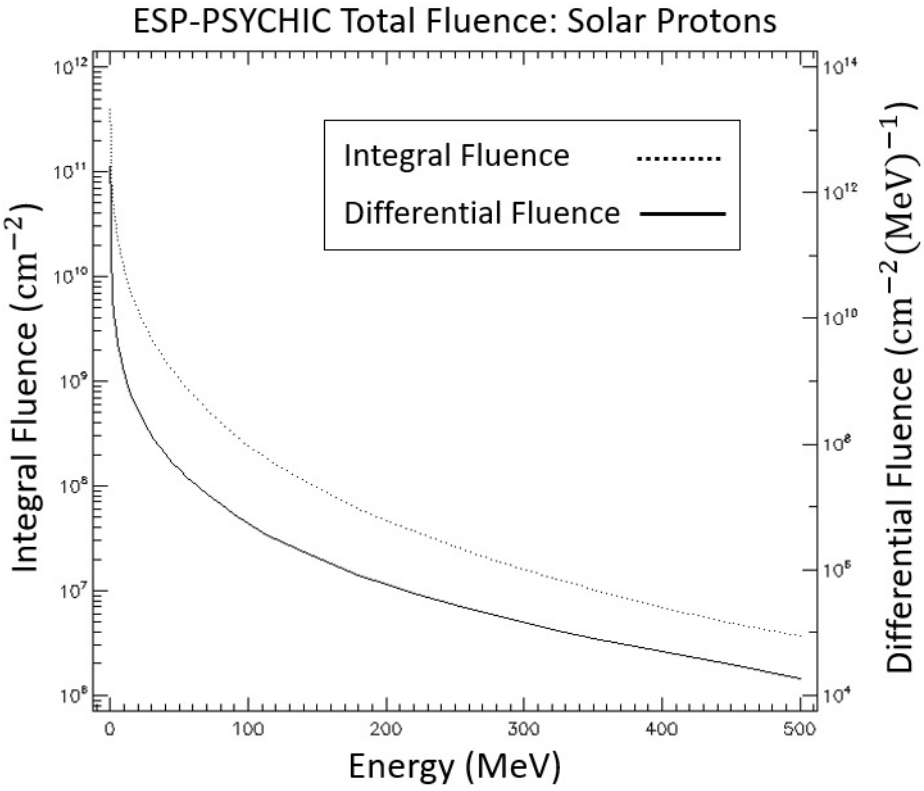

Figure 5.27 Solar Hydrogen Energy-Differential Fluence-Integral Fluence graph.

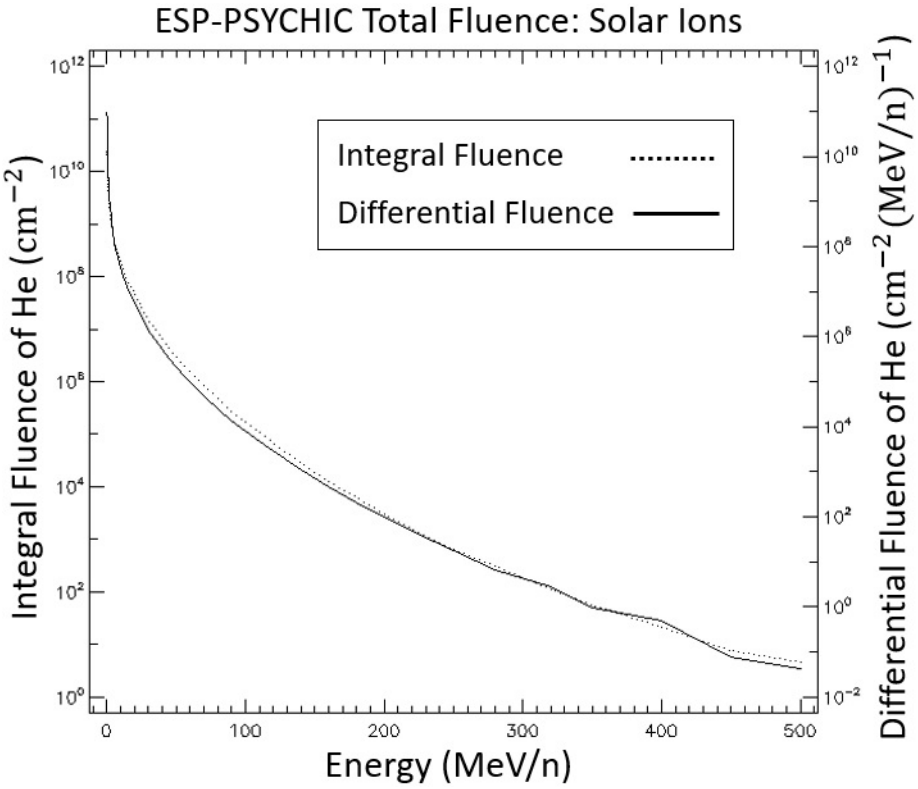

Figure 5.28 Solar Helium Energy-Differential Fluence-Integral Fluence graph.

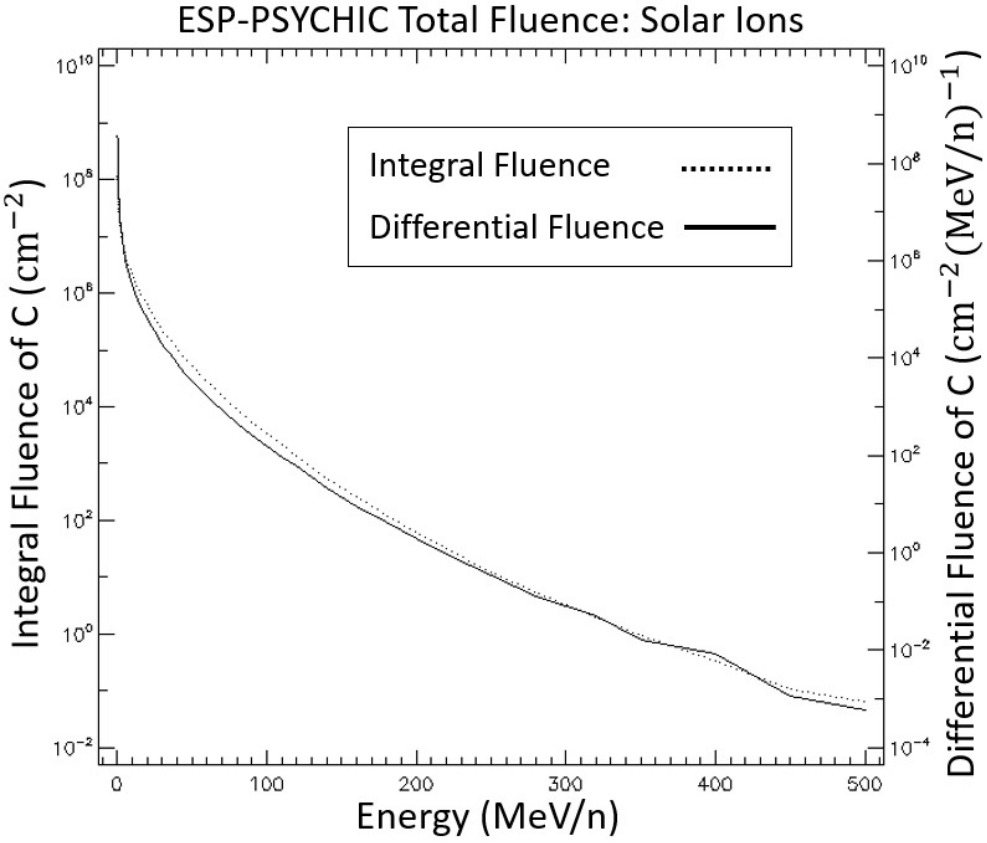

Figure 5.29 Solar Carbon Energy-Differential Fluence-Integral Fluence graph.

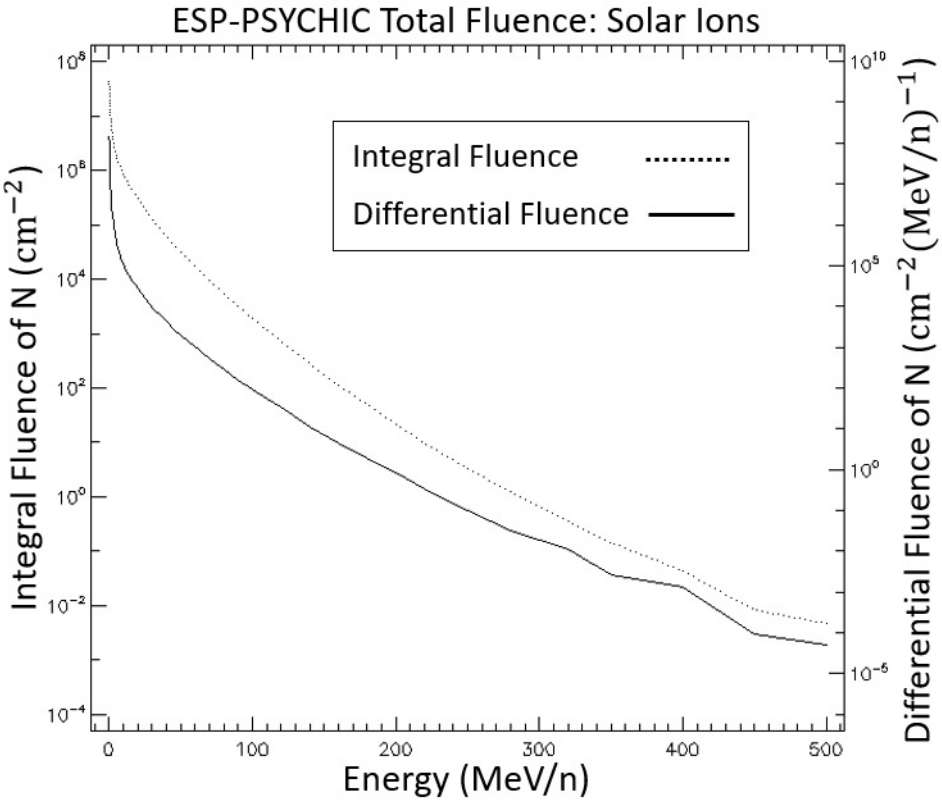

Figure 5.30 Solar Nitrogen Energy-Differential Fluence-Integral Fluence graph.

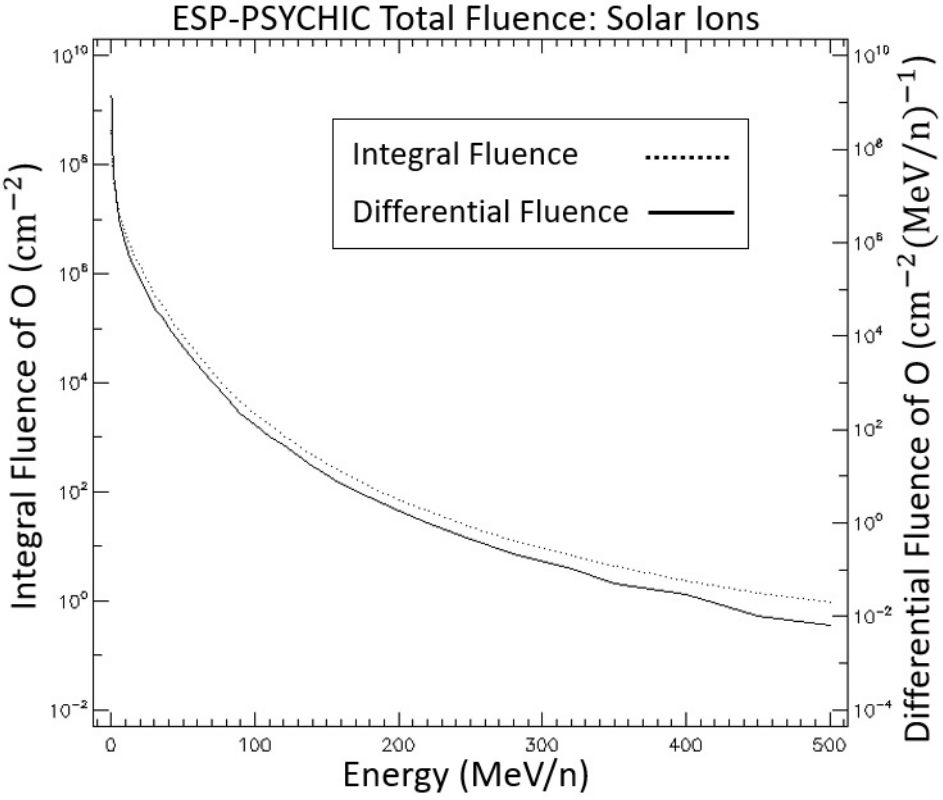

Figure 5.31 Solar Oxygen Energy-Differential Fluence-Integral Fluence graph.

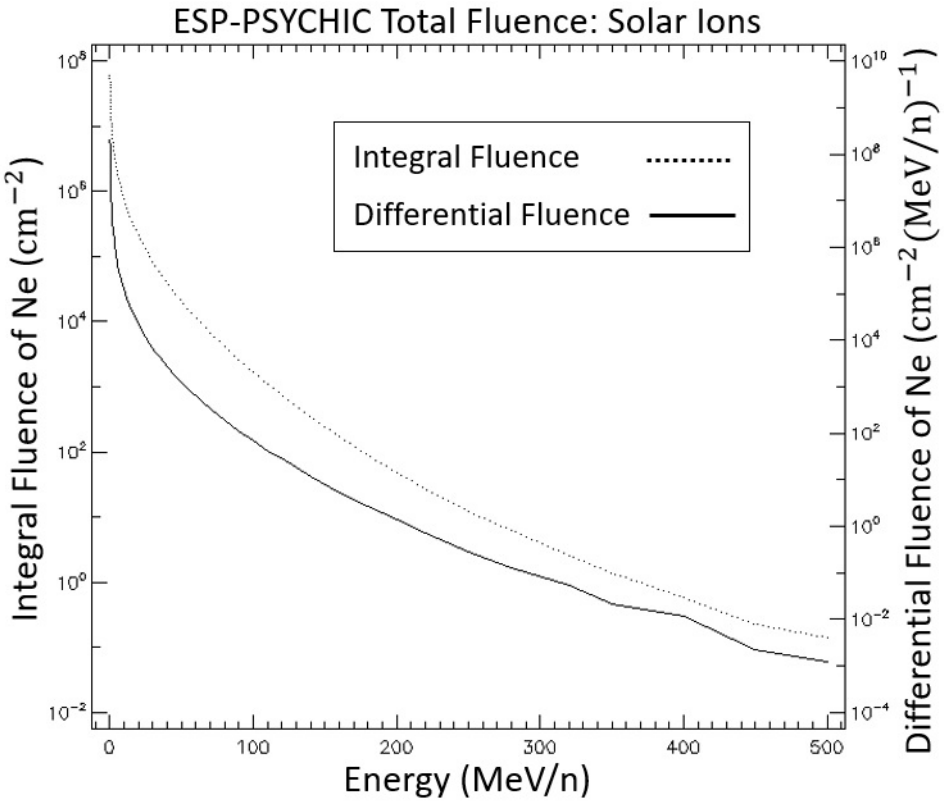

Figure 5.32 Solar Neon Energy-Differential Fluence-Integral Fluence graph.

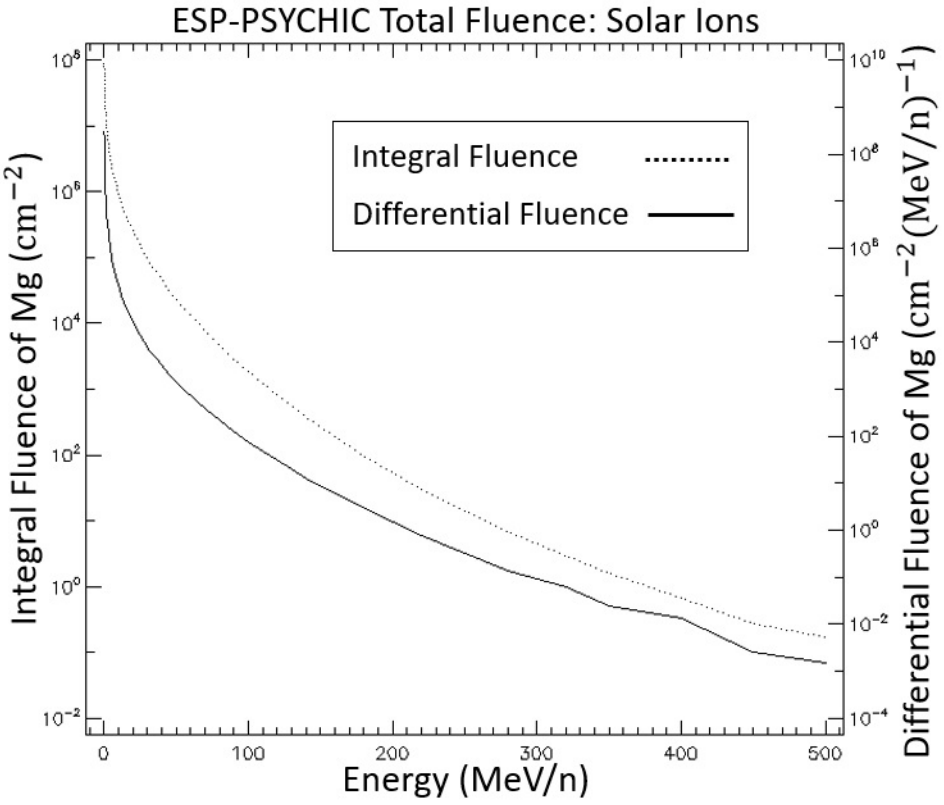

Figure 5.33 Solar Magnesium Energy-Differential Fluence-Integral Fluence graph.

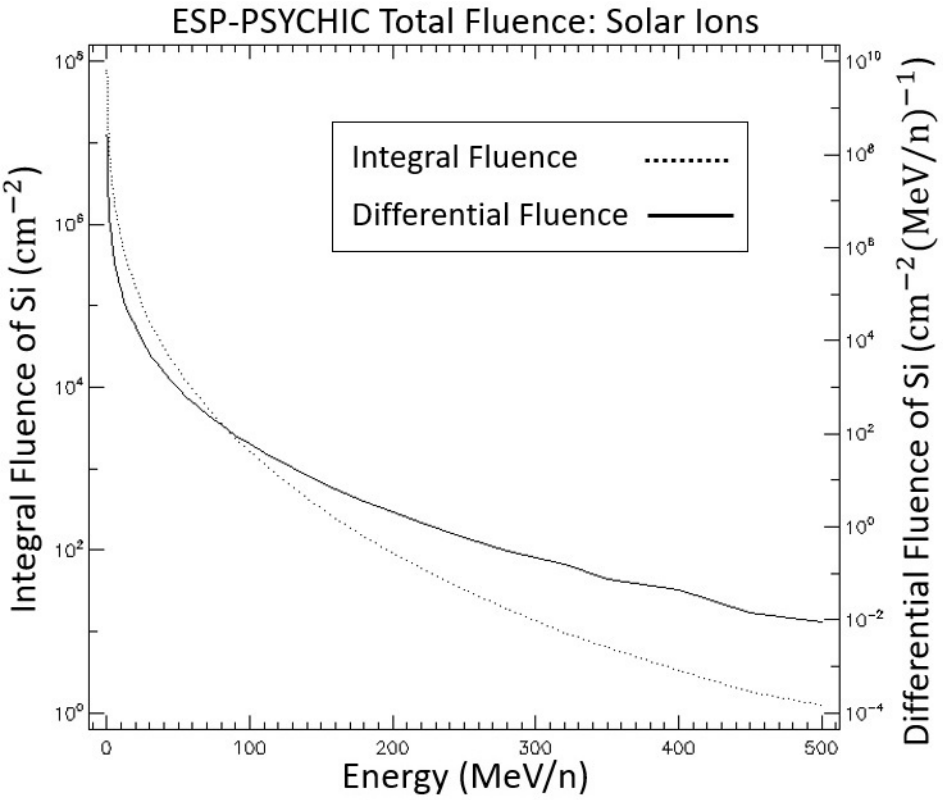

Figure 5.34 Solar Silicon Energy-Differential Fluence-Integral Fluence graph.

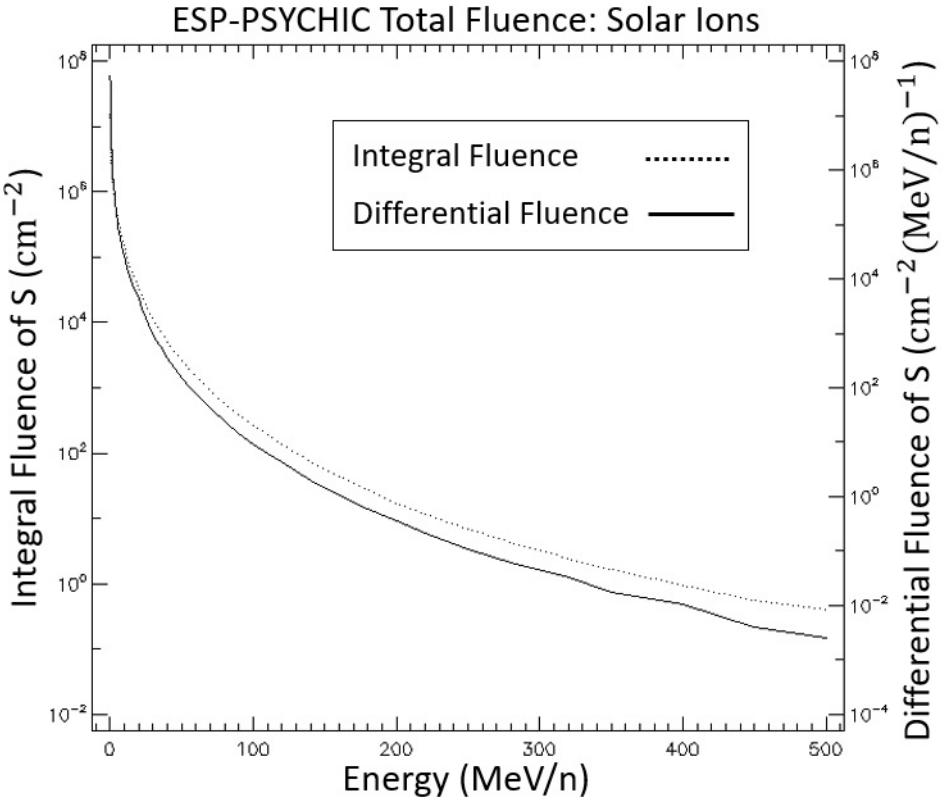

Figure 5.35 Solar Sulfur Energy-Differential Fluence-Integral Fluence graph.

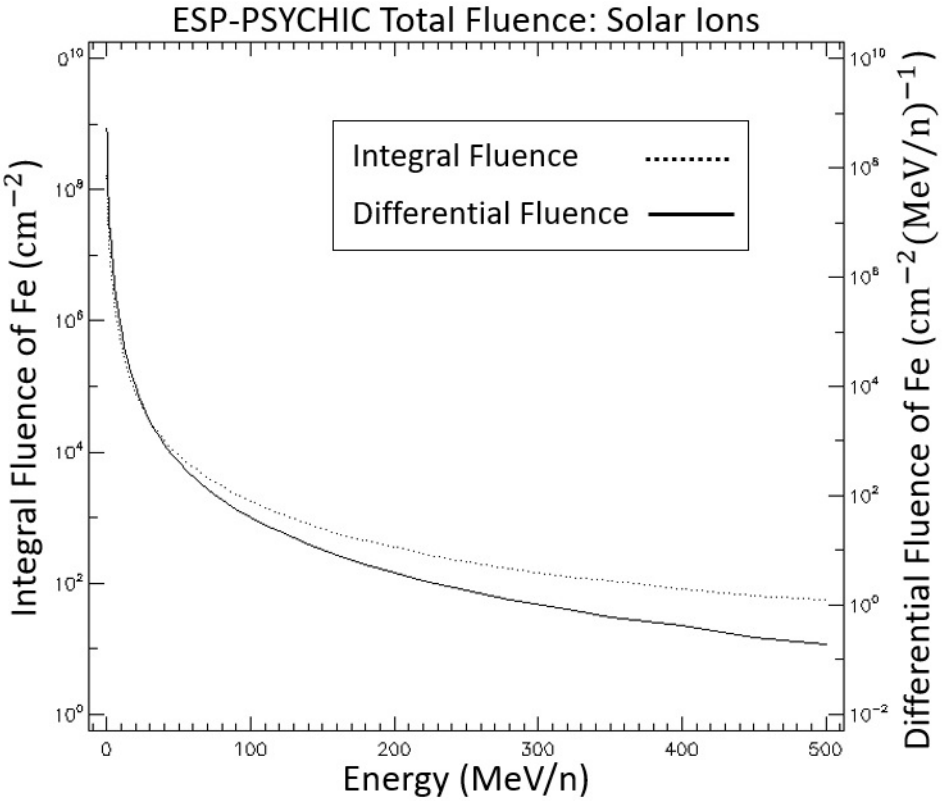

Figure 5.36 Solar Iron Energy-Differential Fluence-Integral Fluence graph.

5.2.2 Galactic Cosmic Ray Data

In graphs from Figure 5.37 to Figure 5.48, galactic cosmic ray flux and energy data are given, for the second part of the mission. Galactic cosmic ray particles were chosen based on their abundance ratios, as in the simulations for the first part of the mission. These particles are hydrogen, helium, lithium, beryllium, boron, carbon, nitrogen, oxygen, neon, magnesium, silicon, and iron. These are the most abundant 12 particles [28]. The exact cause of the differential flux breakpoints in the graphs is not clearly known. However, these breakpoints are thought to originate from the mission segments.

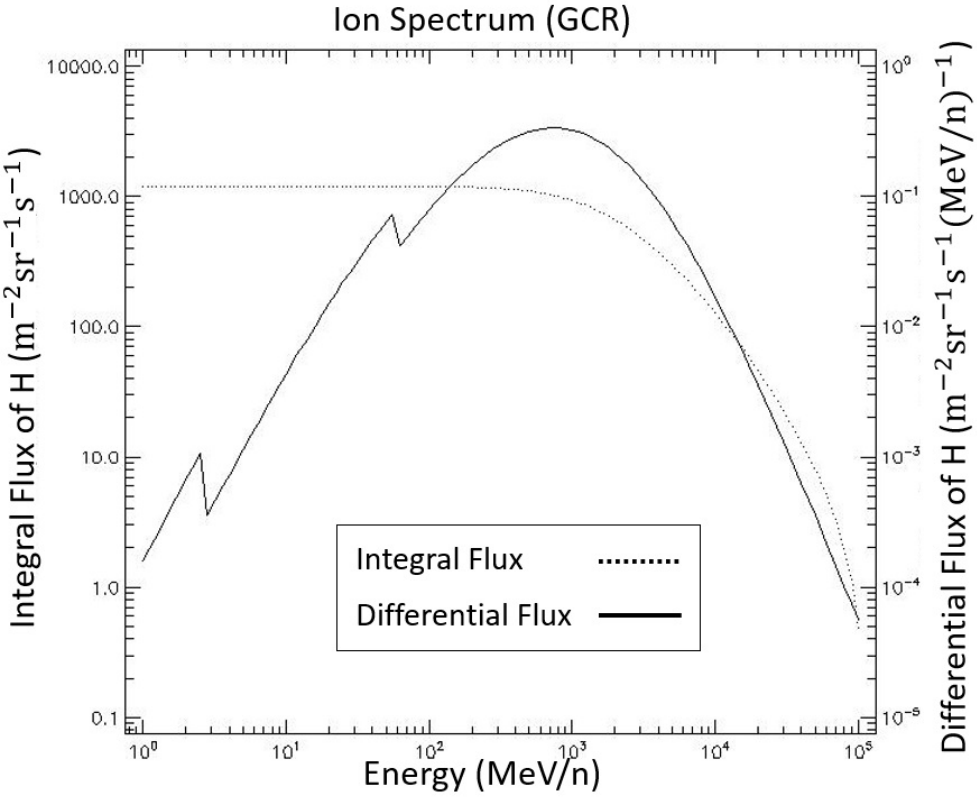

Figure 5.37 GCR Hydrogen Energy-Differential Flux-Integral Flux graph.

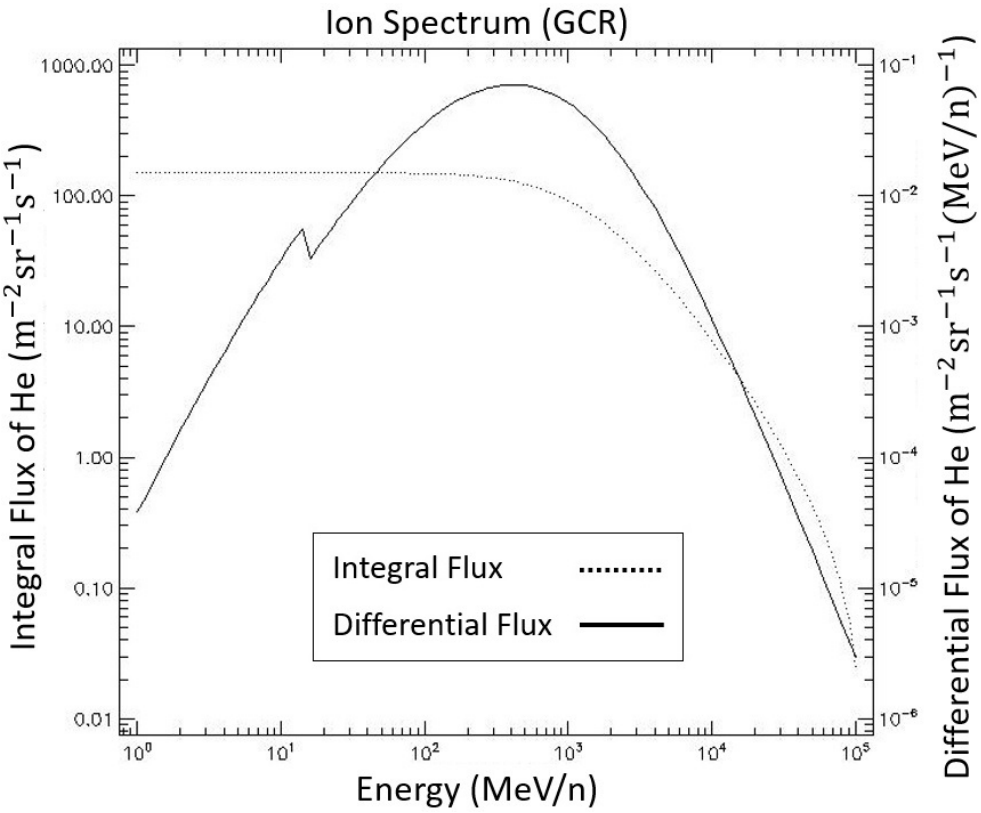

Figure 5.38 GCR Helium Energy-Differential Flux-Integral Flux graph.

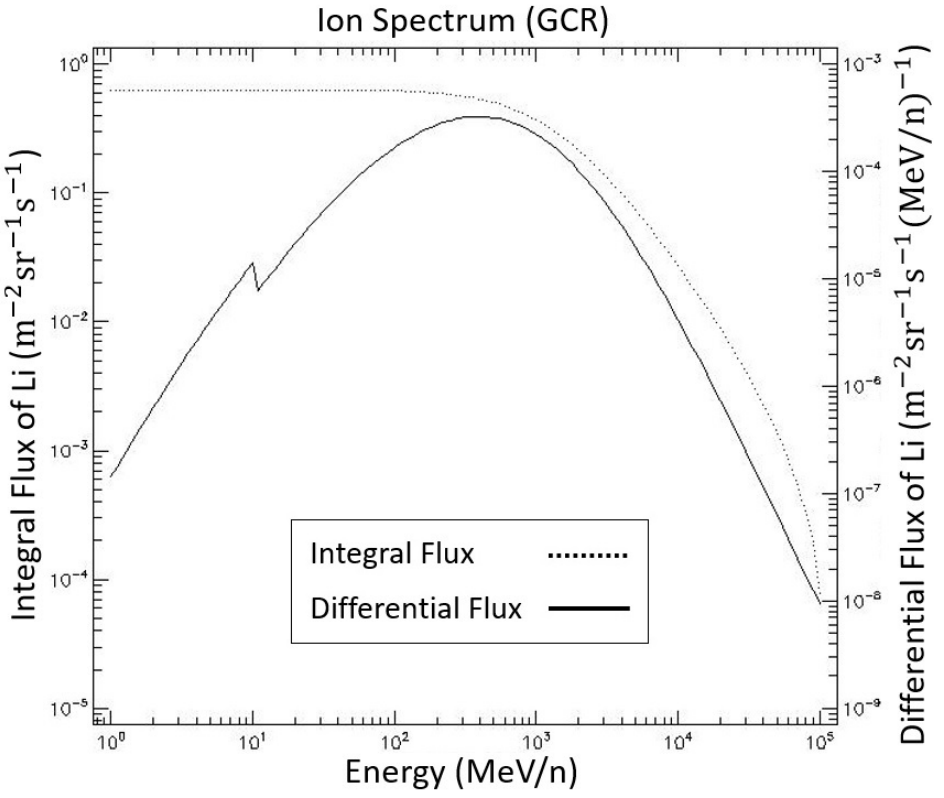

Figure 5.39 GCR Lithium Energy-Differential Flux-Integral Flux graph.

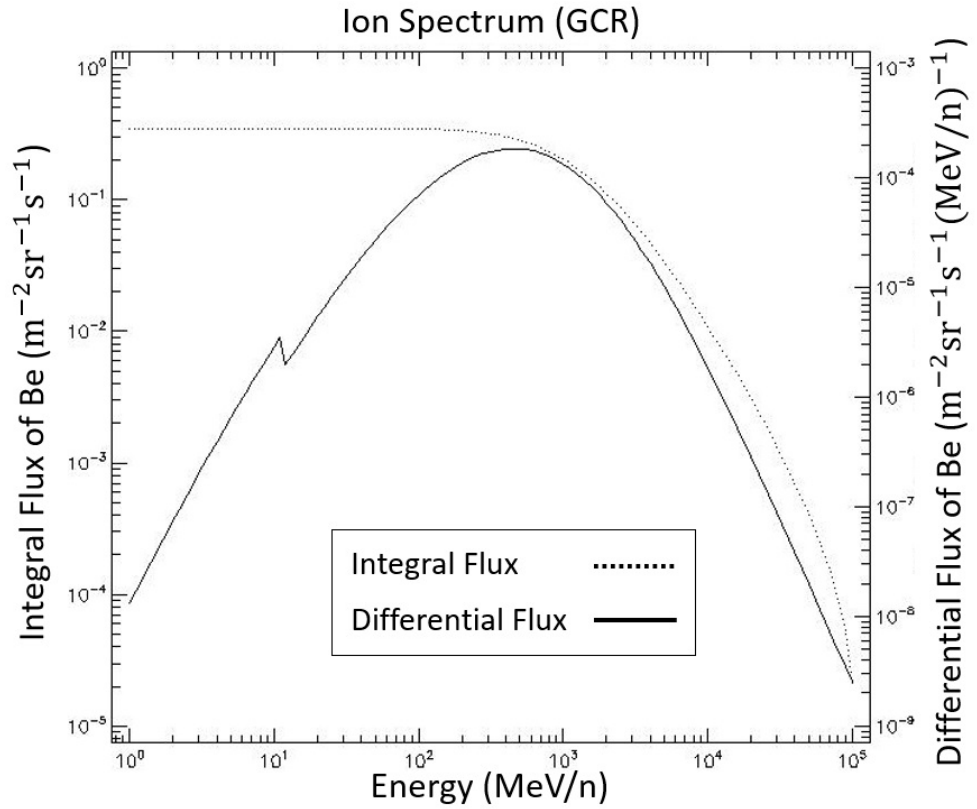

Figure 5.40 GCR Beryllium Energy-Differential Flux-Integral Flux graph.

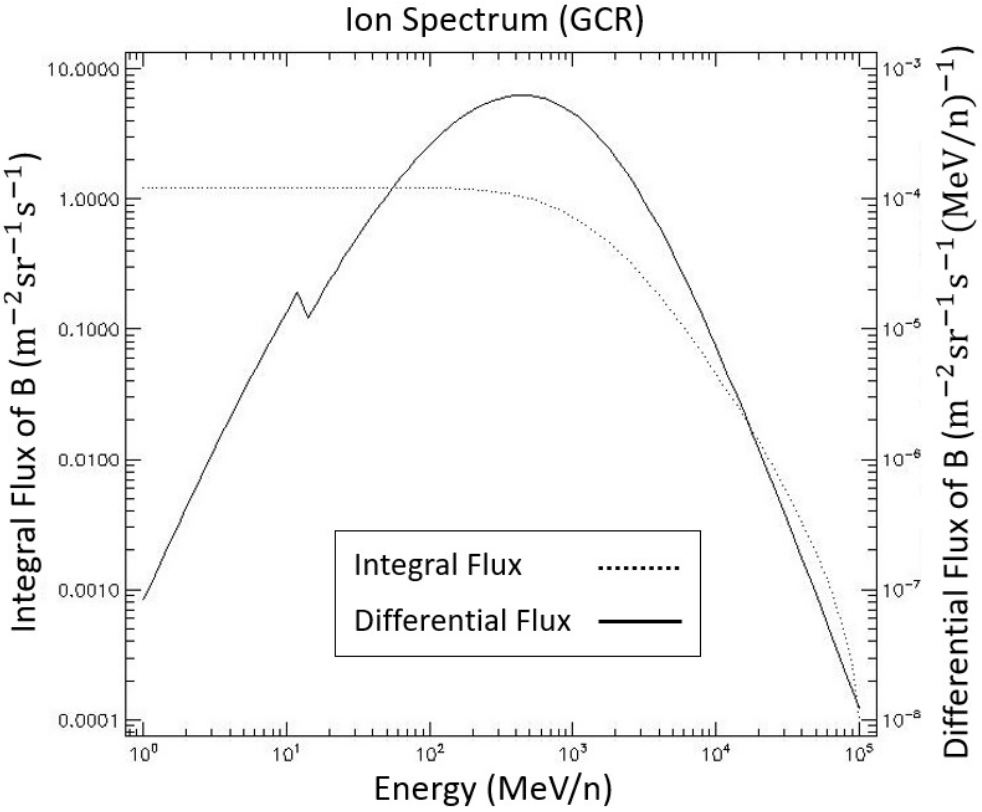

Figure 5.41 GCR Boron Energy-Differential Flux-Integral Flux graph.

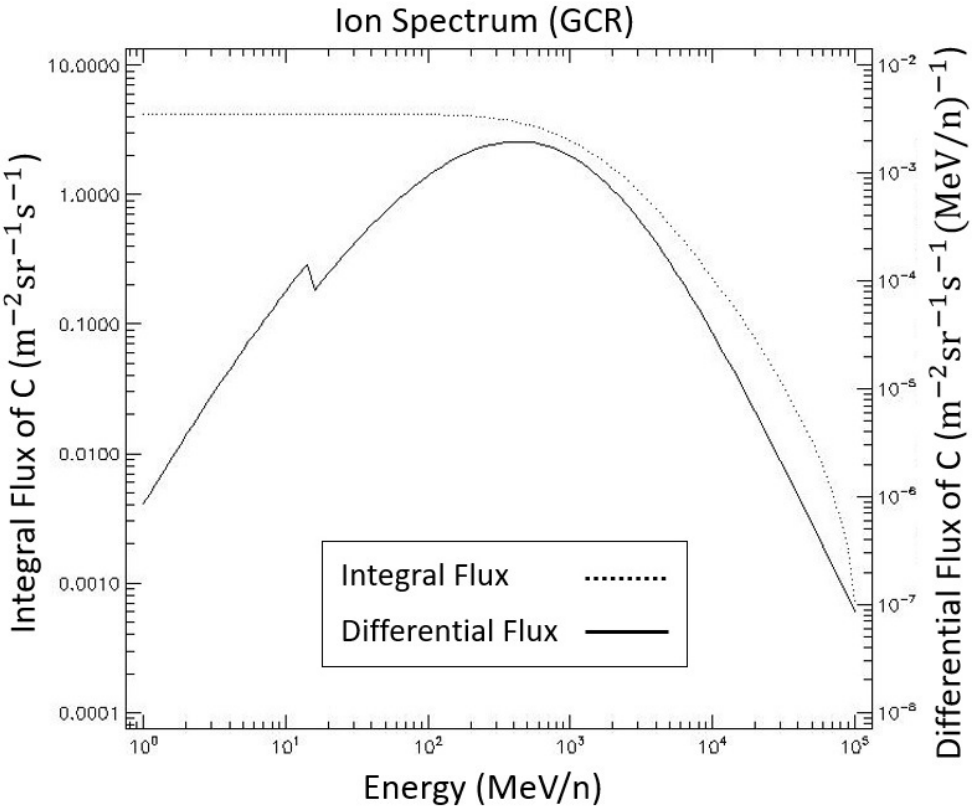

Figure 5.42 GCR Carbon Energy-Differential Flux-Integral Flux graph.

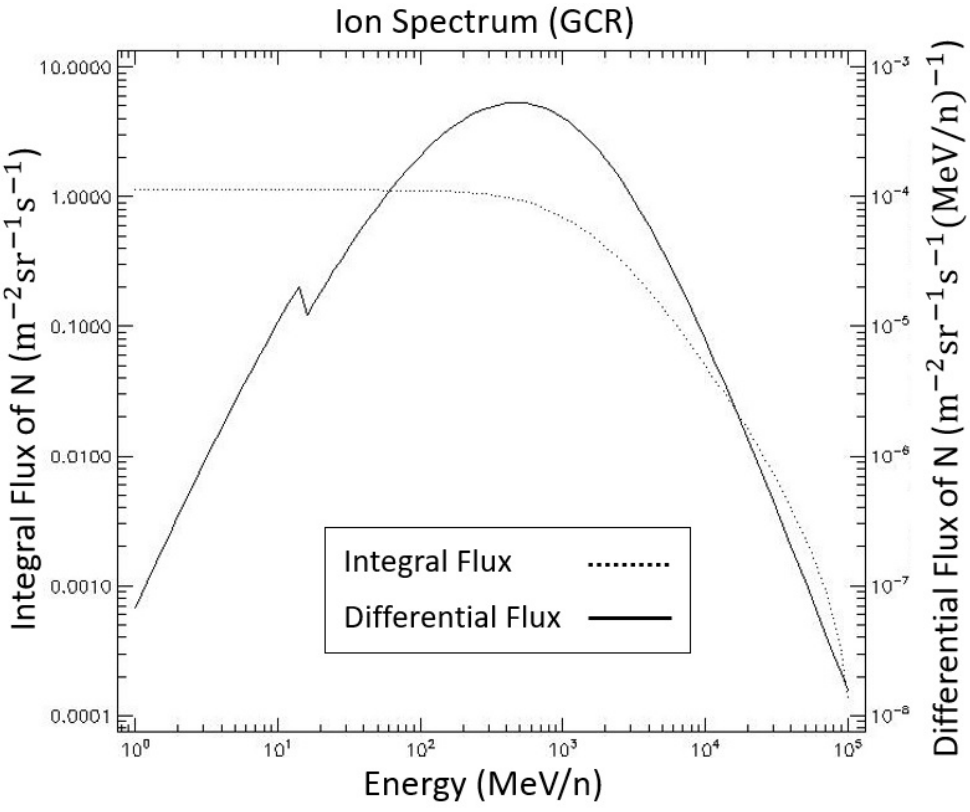

Figure 5.43 GCR Nitrogen Energy-Differential Flux-Integral Flux graph.

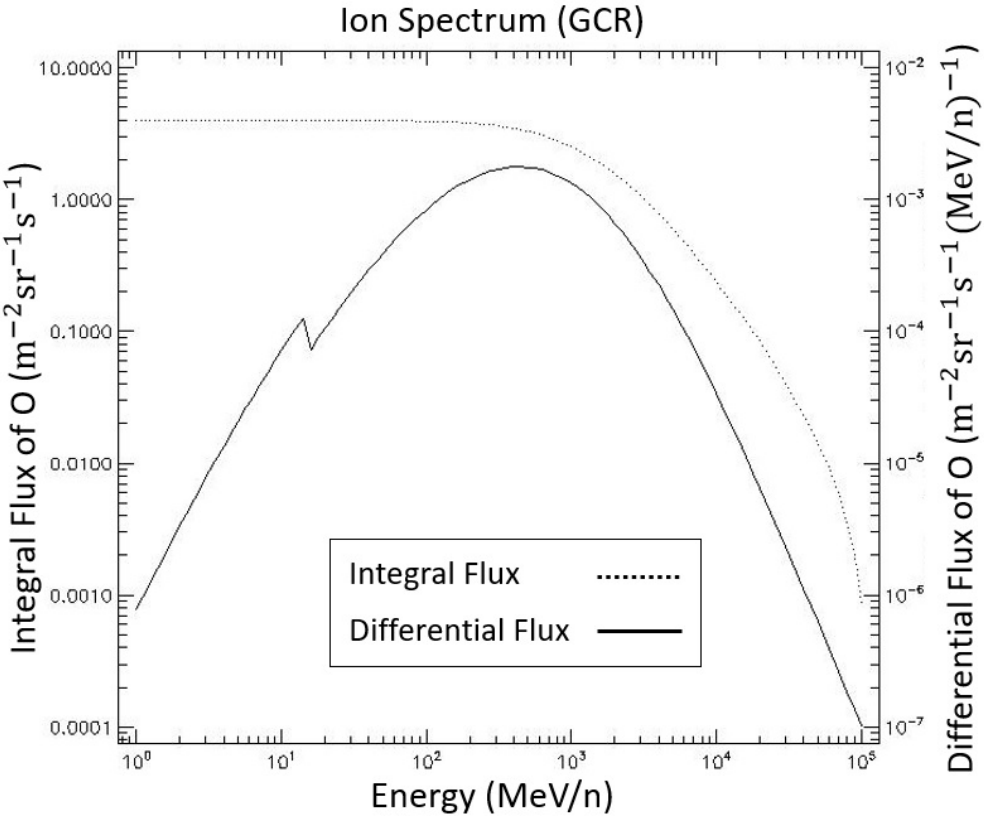

Figure 5.44 GCR Oxygen Energy-Differential Flux-Integral Flux graph.

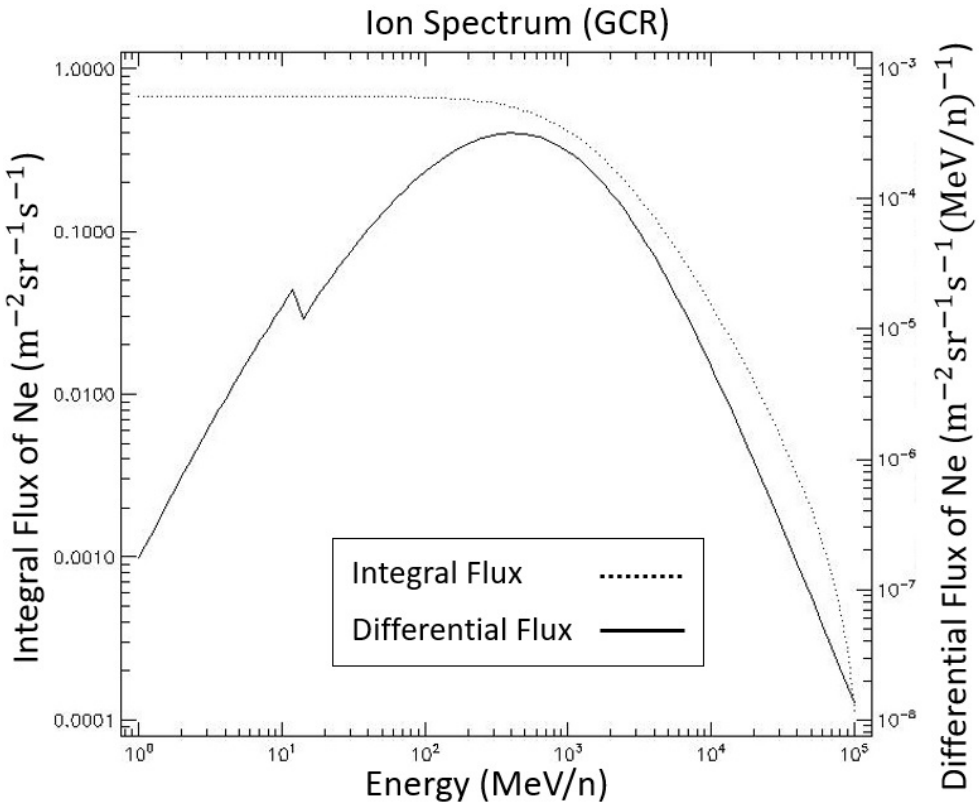

Figure 5.45 GCR Neon Energy-Differential Flux-Integral Flux graph.

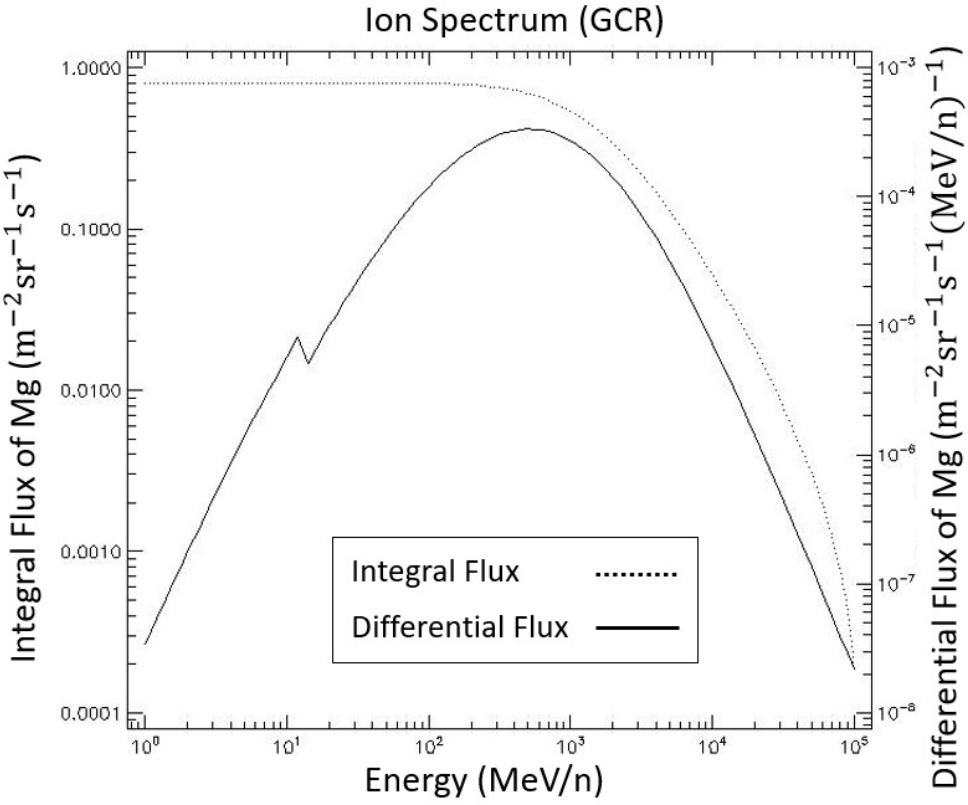

Figure 5.46 GCR Magnesium Energy-Differential Flux-Integral Flux graph.

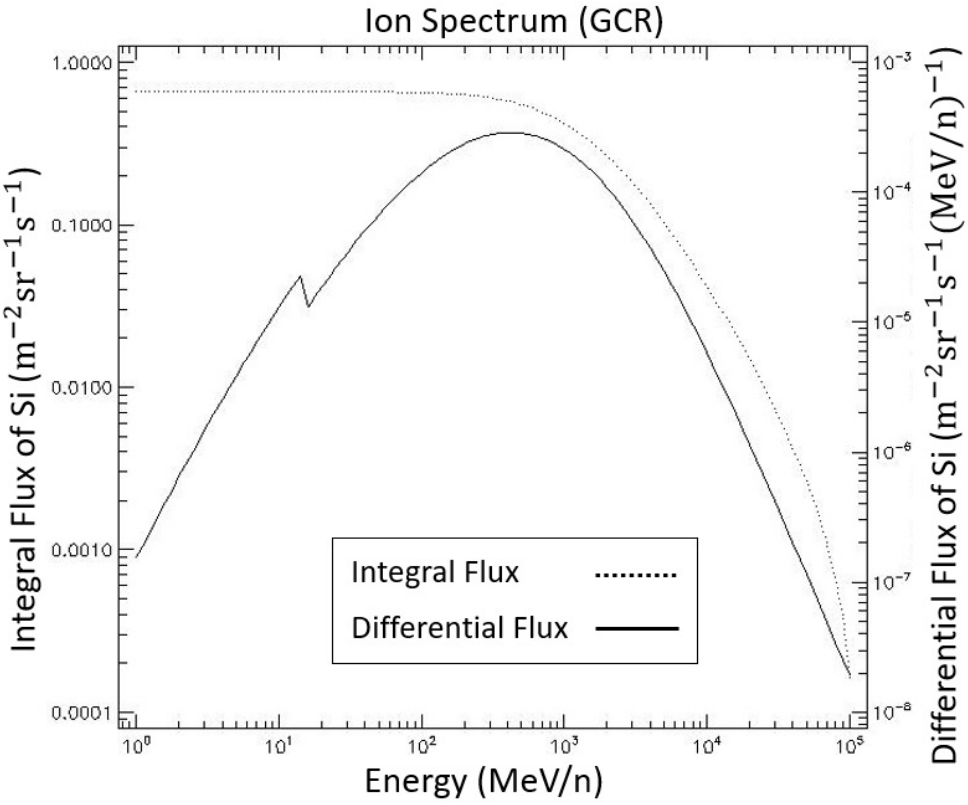

Figure 5.47 GCR Silicon Energy-Differential Flux-Integral Flux graph.

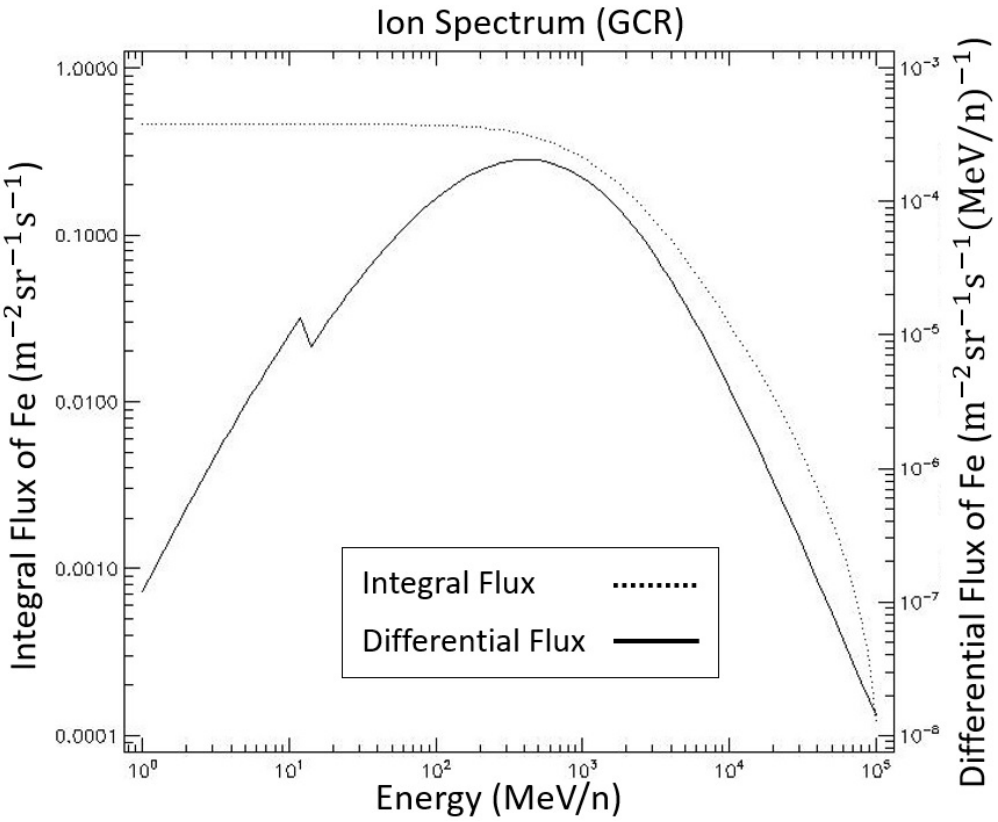

Figure 5.48 GCR Iron Energy-Differential Flux-Integral Flux graph.

6
GEANT4 SIMULATION

Using Monte Carlo methods to simulate the passage of particles through matter [72], Geant4 is built to handle complex geometries and physics models. Geant4 was developed by a worldwide, Cern-based collaboration of physicists and software engineers, and is the continuation of the Geant (Geometry and Tracking) software series. Maintenance processes are also carried out by Geant4 cooperation. Geant4 toolkit is written in C++ language. It has a very wide range of functionality, including tracking, geometry, physics models, and hits. It has different application areas [73]. High energy physics, space science, and medical physics are examples of Geant4's areas of use [74].

6.1 Simulation Result

In the 2023 Turkish Lunar Mission, under the predicted conditions, the satellite will be exposed to $2.766 \pm 0.089 \times 10^{-1}$ Gy s^{-1} in the first part of the mission and $2.438 \pm 0.078 \times 10^{-3}$ Gy s^{-1} in the second part. The error rates of the simulation results for both parts of the mission correspond to approximately 3.2% of the results found. While calculating the error, the average energy value, the average energy value error, the number of particles entering, the error of the number of particles entering (with Poisson statistics) were obtained in each BIN in the histograms obtained as a result of the simulation. With Error propagation, the energy error in each histogram was found first. Then the total energy error was found using the energy errors in each histogram. Using the error of the total energy in the error propagation, the error in the radiation dose rate was found. In Geant4 simulations, the step size is 0.1 mm. During the first part of the mission, namely Earth Bound Orbits and Lunar Transfer Trajectory, 72.47% of all particles that cause the dose rate to which the spacecraft is exposed are electrons, 27.48% are protons and the remaining particles are alpha particles, and heavy ions. In the second part of the mission, that is, around the Moon, 93.80% of the particles that cause the dose rate are protons and the remaining particles are alpha particles and heavy ions.

7
METHOD COMPARISON SIMULATION WITH CHANDRAYAAN-1 MISSION

Chandrayaan-1 is the first lunar mission under the Indian Space Research Organisation's (ISRO) Chandrayaan programme and the mission was done in 2008. The trajectory of the Chandrayaan-1 mission was mentioned in Section 3. Chandrayaan-1 satellite carried 11 scientific instruments and one of those instruments is Radiation Dose Monitor (RADOM) [75]. Chandrayaan-1 measured radiation dose throughout the mission with RADOM [11]. For this study, some of the data of the radiation dose measurement made in the mission was accessed. The data reached was given by Tsvetan Dachev from the Bulgarian Academy of Sciences. The trajectory and date from which the data was obtained were simulated exactly. By comparing the simulation result with the result obtained in the mission, the relationship between the method followed and the real data was examined. For comparison, first of all, SPENVIS was used to obtain the particle environment data of that orbit at the time the data was collected. Secondly, RADOM was modeled with real dimensions and materials using AutoCAD. Then, using FreeCAD and GUIMesh, the GDML file was created from the STEP file of the design. Finally, Geant4 simulation was performed using the RADOM model and particle environment data obtained from SPENVIS.

7.1 Orbit in Chandrayaan-1 Mission Data

The Chandrayaan-1 satellite completed one orbit between 07:43:21 and 14:21:40 on October 22, 2008. The perigee and apogee of this orbit was approximately 255 km and 22840 km [11], respectively. The image of the orbit obtained by GMAT and it is given in Figure 7.1.

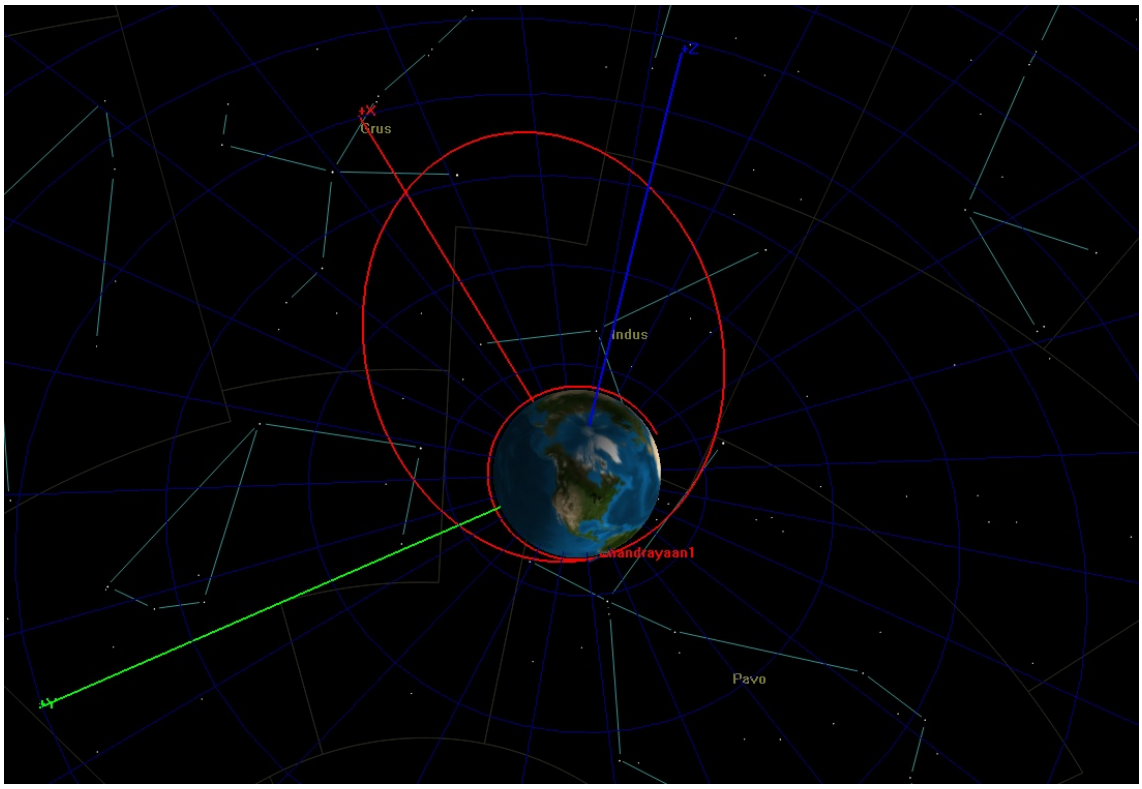

(a) Image from above.

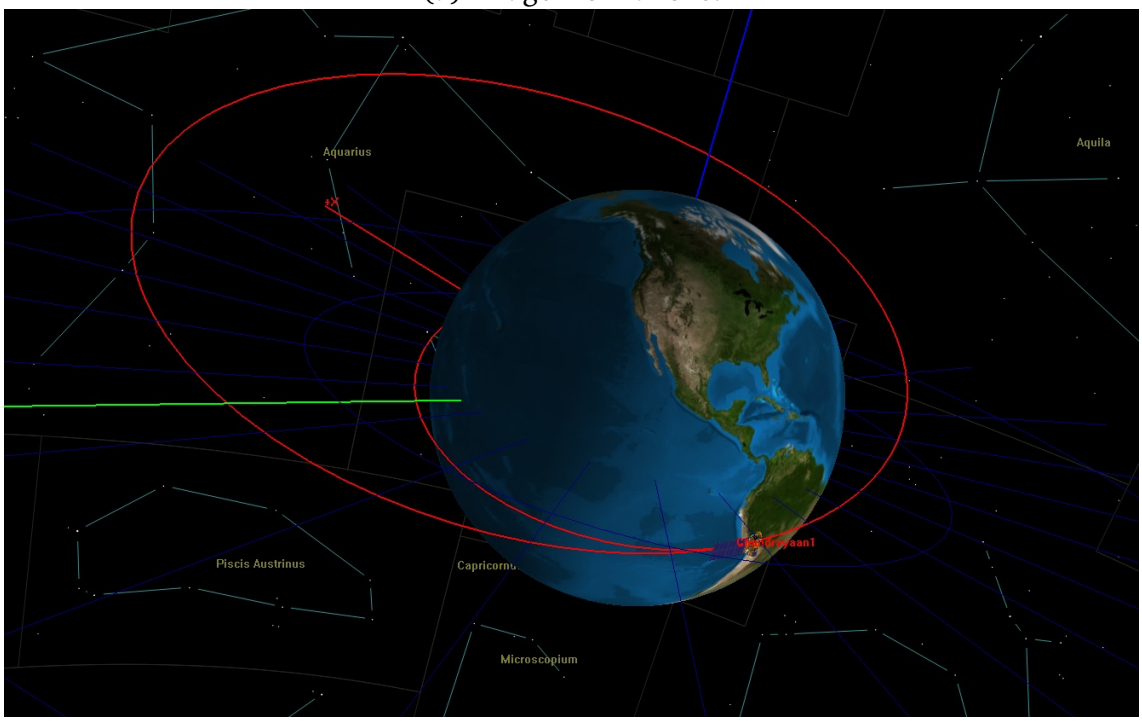

(b) Image from back.

Figure 7.1 GMAT view of the Chandrayaan-1 orbit between 07:43:21 and 14:21:40 on October 22, 2008.(The part of settling into orbit from the Earth is not included in the data.)

7.2 Modeling of RADOM

The 256 channels spectrometer RADOM measured dose by using silicon detector. Silicon detector is 0.3 mm thick and its area is $2cm^2$. RADOM, shielded by 1.0 mm aluminum, 0.1 mm copper, 0.2 mm plastic material and 15 layers of aluminized kapton. Its dimensions are $10cm \times 4cm \times 2cm$ [76]. A photo of RADOM is provided in Figure 7.2.

Figure 7.2 Photo of RADOM. Adapted from [11].

Figure 7.3 shows the model of the RADOM detector made with AutoCAD. For Geant4 simulation, a cube with 1.5 meters of was made to represent the satellite, under the detector. The walls were made of 2 mm thick Al, the base and top were made of 5 mm thick Al, and three fuel tanks were made around the center. The wall thickness of the tank was also made of 2 mm Al [66].

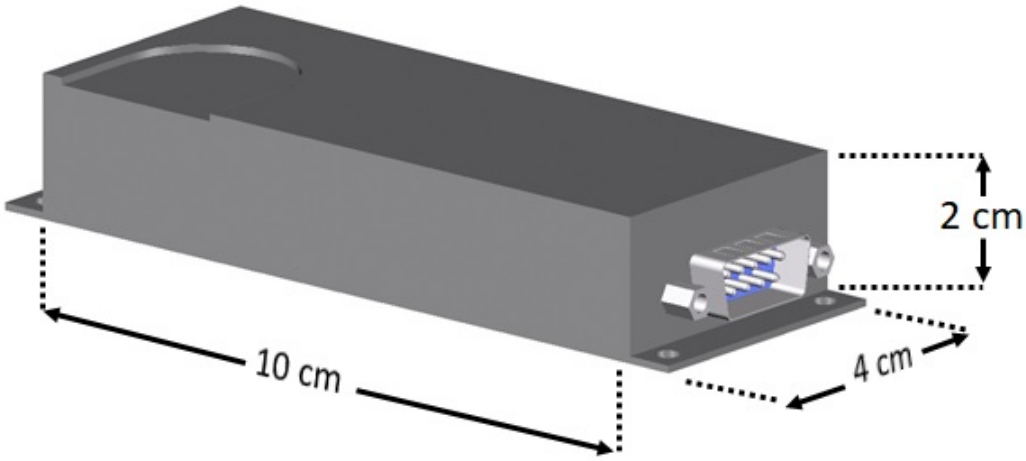

Figure 7.3 AutoCAD design of RADOM.

7.3 SPENVIS Data of Chandrayaan 1 Mission

The particle environment of the orbit specified in Section 7.1 was simulated in SPENVIS. The orbital parameter of the mission is given in Figure 7.4.

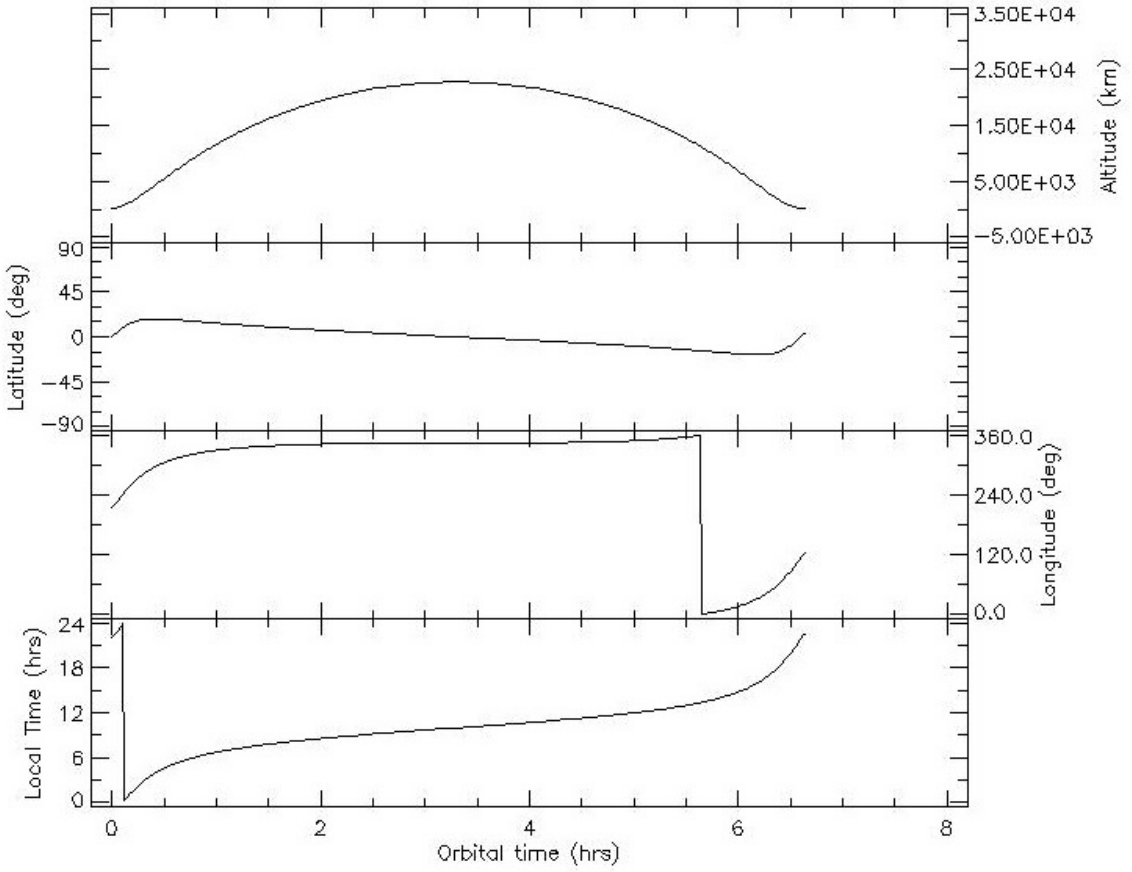

Figure 7.4 Orbit parameters [15].

It is the trapped particles in the Van Allen Belts that have the most impact on the spacecraft in this orbit. Orbit-flux plots of trapped protons and trapped electrons are given in Figure 7.5 and Figure 7.6, respectively.

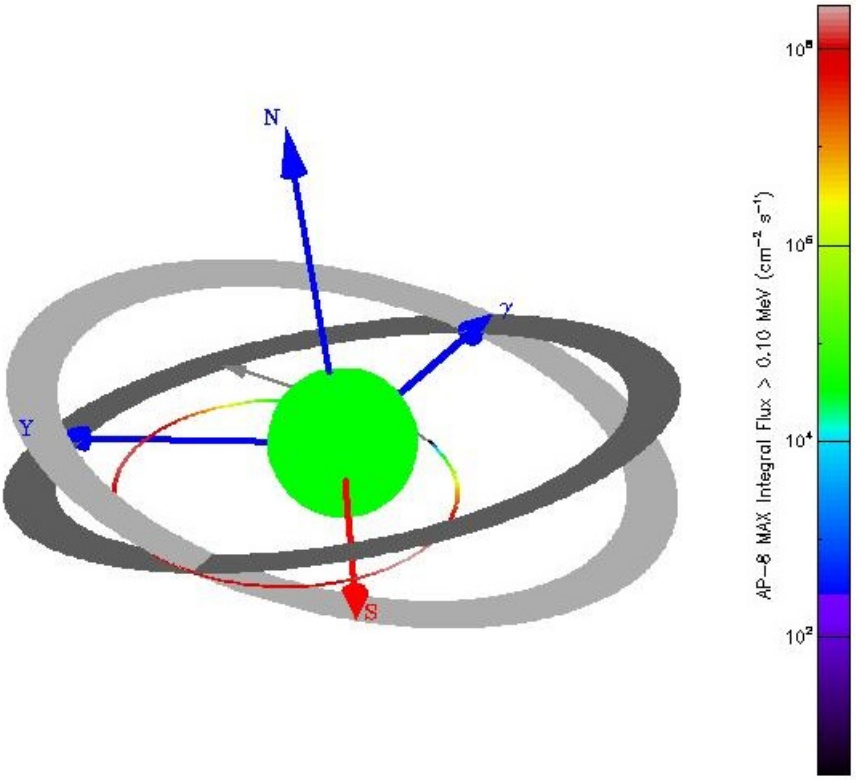

Figure 7.5 Orbit-Flux plot for proton in Van Allen Belts [15].

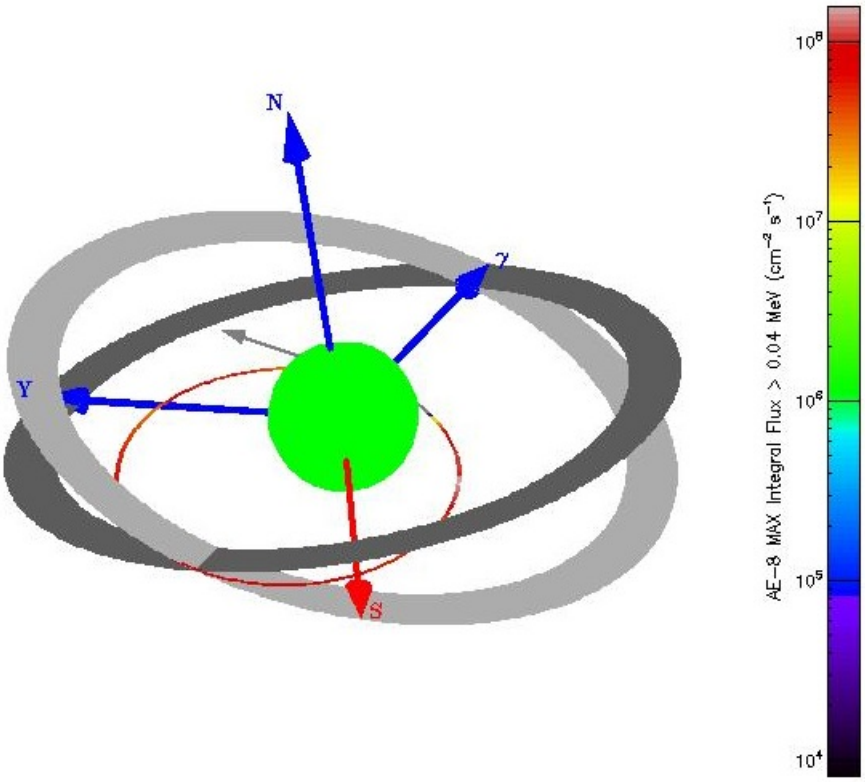

Figure 7.6 Orbit-Flux plot for electron in Van Allen Belts [15].

Energy-flux graphics of trapped protons and trapped electrons are given in Figure 7.7 and Figure 7.8, respectively. In Figure 7.7 and Figure 7.8, integral flux is higher than differential flux. According to the trajectory, this is a typical situation because the spacecraft had been in the approximately central zone of inner Van Allen Belt and outer Van Allen Belt. But integral flux is getting close to differential flux for high energies in trapped electron graph. The reason for this approximation is the apogee of the orbit. Apogee is not in the main zone of the outer Van Allen Belt.

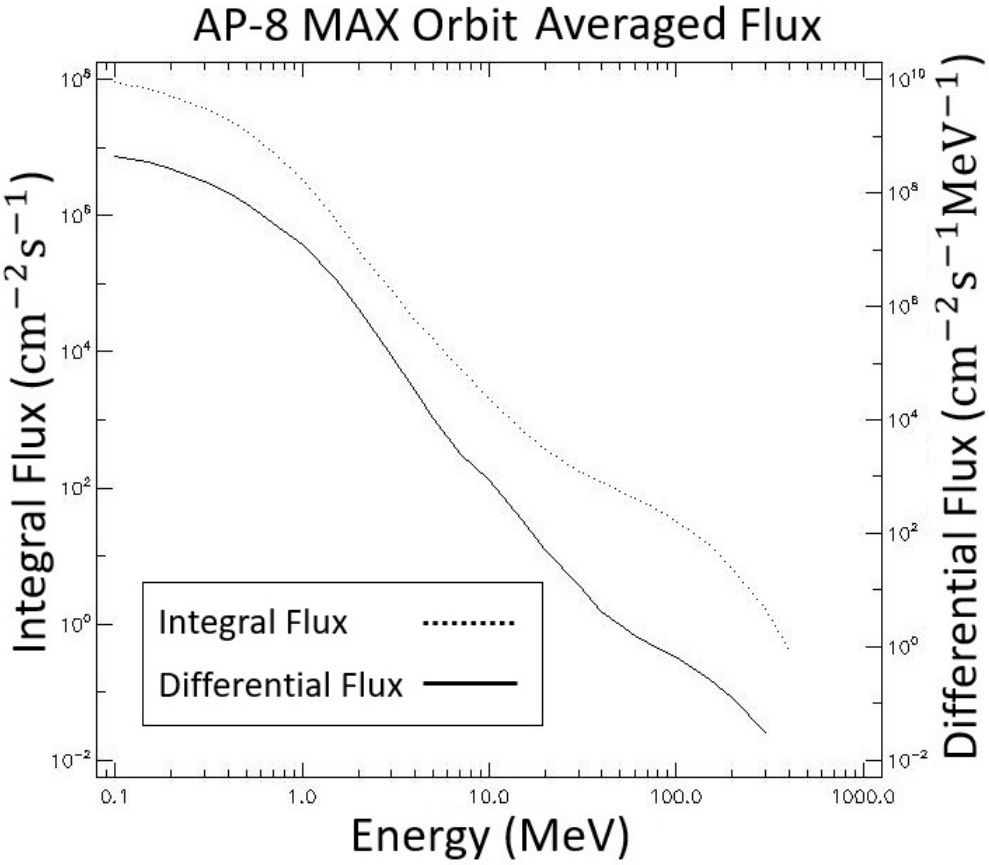

Figure 7.7 Energy-Differential Flux-Integral Flux graph for proton in Van Allen Belts [15].

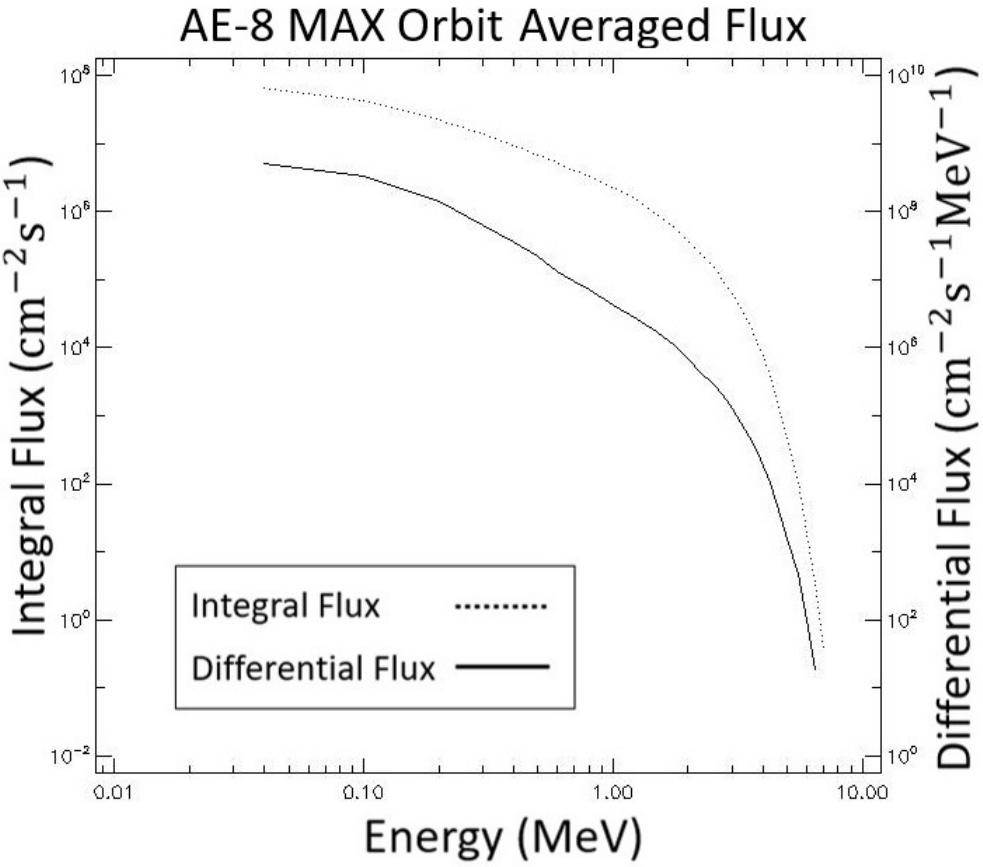

Figure 7.8 Energy-Differential Flux-Integral Flux graph for electron in Van Allen Belts [15].

The solar particle flux on this orbit is zero. Galactic cosmic ray data were used only for hydrogen, helium, carbon and oxygen, as the flux of other particles was observed to be much lower. The energy-differential flux-integral flux plots of these four particles were combined in MATLAB and given in Figure 7.9.

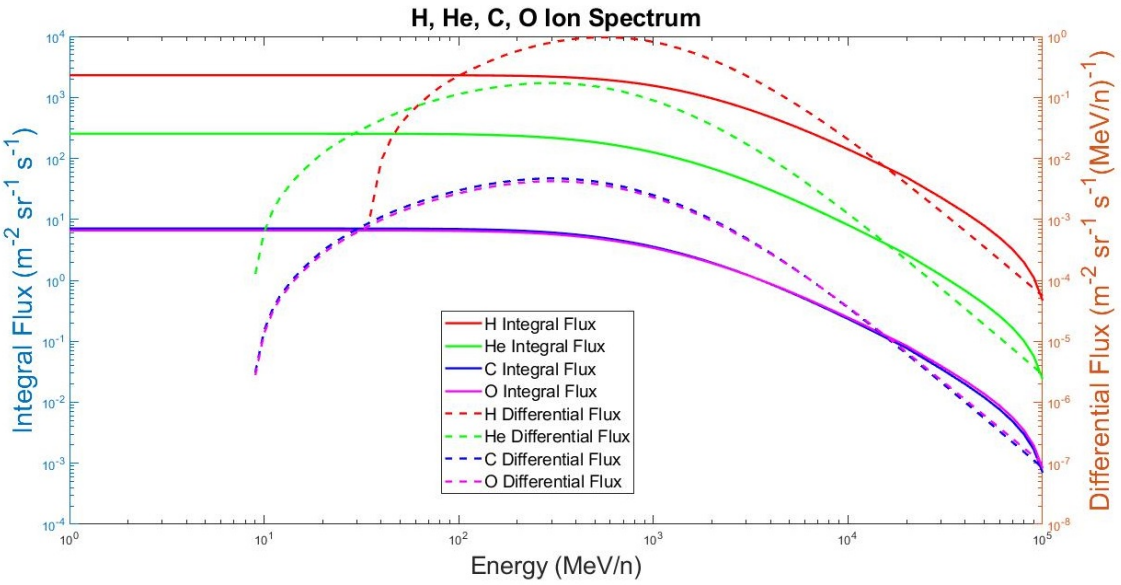

Figure 7.9 Energy-Differential Flux-Integral Flux graph for GCR particles [15]. In this graph, you can see the proportions of hydrogen (%90), helium (%9) and other particles (%1) that constitute the galactic cosmic rays mentioned in Section 2.3.

7.4 Geant4 Simulation Result and RADOM Measurement

The RADOM modeling, trajectory and SPENVIS data given above were used in the Geant4 simulation. According to the simulation result, the radiation dose that RADOM should be exposed to is $2.348 \pm 0.449 \times 10^{-5}$ Gy s^{-1}. The error rate corresponds to approximately 19.1% of the simulation result obtained. For the orbit where Chandrayaan-1 was located between 07:43:21 and 14:21:40 on October 22, 2008, RADOM measured the radiation dose rate as 4.004×10^{-6} Gy s^{-1} [11].

Table 7.1 Comparison between Chadnrayaan-1 RADOM measurement result and Geant4 simulation.

	Dose Rate
Chandrayaan-1 RADOM Data	4.004×10^{-6} Gy s^{-1}
Simulation Result	$2.348 \pm 0.449 \times 10^{-5}$ Gy s^{-1}

8
CONCLUSION

In this study, simulation studies were carried out to find the radiation dose to be exposed to the spacecraft in the 2023 Turkish Lunar Mission. The results are given in Section 6. Comparison results made to test the reliability of the method used in the study are given in Section 7.

The Chandrayaan-1 simulation result was approximately 6 times greater than the dose measured by RADOM. This is an expected difference because, according to the simulation results performed before the Chandrayaan-1 mission, the flux values obtained from SPENVIS were found to be 200 times the flux measured during the Chandrayaan-1 mission [11]. In this study, SPENVIS values of the same date were used. Therefore, SPENVIS data is almost identical. According to the simulation result, it should be expected that the modeled RADOM will be exposed to more radiation. The method used is reliable, but the ratios between the real and the simulation results should be taken into account.

It is thought that there are basically three reasons for the high radiation dose rate to which the spacecraft will be exposed during the mission under the specified conditions. The first is the size of the model satellite. The second is the uncertainties of the models used [11]. This uncertainty often causes high particle flux. High particle flux also causes a higher radiation dose. Another reason is that the solar particle contribution was found to be high in the data obtained from SPENVIS. This is because the estimated date of the mission to be performed is at a time when Solar activity continues to increase due to Solar Cycle 25 [77].

The modeled satellite, the determined mission date, and the majority of the designed mission profile were based on predictions. If the estimated conditions change, the simulation results will change. For this reason, since the satellite model and mission profile in this study will not be exactly the same as the orbit and satellite to be used in the 2023 Turkish Lunar Mission, the dose rate to be measured in the mission will also differ.

REFERENCES

[1] J. Howard, *Spacecraft environments interactions: Space radiation and its effects on electronic systems*. NASA, 1999.

[2] NASA, *Why space radiation matters*, https://www.nasa.gov/analogs/nsrl/why-space-radiation-matters/, [Online; accessed 05-May-2022], 2019.

[3] E. R. Benton, E. Benton, "Space radiation dosimetry in low-earth orbit and beyond," *Nuclear Instruments and Methods in Physics Research Section B: Beam Interactions with Materials and Atoms*, vol. 184, no. 1-2, pp. 255–294, 2001.

[4] A. D. Topper *et al.*, "Nasa goddard space flight center's compendium of total ionizing dose, displacement damage dose, and single-event effects test results," in *2019 IEEE Radiation Effects Data Workshop*, IEEE, 2019, pp. 1–10.

[5] D. Holmberg, "Radiation protection in space," *Umeå University*, 2010.

[6] B. A. Buffett, "Earth's core and the geodynamo," *Science*, vol. 288, no. 5473, pp. 2007–2012, 2000.

[7] S. Chapman, V. C. Ferraro, "A new theory of magnetic storms," *Terrestrial Magnetism and Atmospheric Electricity*, vol. 38, no. 2, pp. 79–96, 1933.

[8] NASA, *ENAs at the Magnetopause*, https://www.nasa.gov/mission_pages/ibex/multimedia/100816-earth-enas.html#.YoUhZ6hByUk/, [Online; accessed 06-May-2022], 2013.

[9] SPENVIS, *Background: Trapped Particle Radiation Models*, https://www.spenvis.oma.be/help/background/traprad/traprad.html/, [Online; accessed 06-May-2022], 2018.

[10] W. Li, M. Hudson, "Earth's van allen radiation belts: From discovery to the van allen probes era," *Journal of Geophysical Research: Space Physics*, vol. 124, no. 11, pp. 8319–8351, 2019.

[11] T. P. Dachev *et al.*, "An overview of radom results for earth and moon radiation environment on chandrayaan-1 satellite," *Advances in space research*, vol. 48, no. 5, pp. 779–791, 2011.

[12] NASA, *Van Allen Belts*, https://www.nasa.gov/feature/goddard/2018/studying-the-van-allen-belts-60-years-after-america-s-first-spacecraft/, [Online; accessed 06-May-2022], 2018.

[13] N. Y. Ganushkina, I. Dandouras, Y. Shprits, J. Cao, "Locations of boundaries of outer and inner radiation belts as observed by cluster and double star," *Journal of Geophysical Research: Space Physics*, vol. 116, no. A9, 2011.

[14] D. Heynderickx, J. Lemaire, E. Daly, H. Evans, "Calculating low-altitude trapped particle fluxes with the nasa models ap-8 and ae-8," *Radiation measurements*, vol. 26, no. 6, pp. 947–952, 1996.

[15] SPENVIS, *SPENVIS*, https://www.spenvis.oma.be/, [Online; accessed 02-May-2022], 1997-2022.

[16] D. Brautigam, J. Bell, "Crresele documentation, phillips laboratory," *Environmental Research papers*, vol. 1178, p. 1, 1995.

[17] C. E. Jordan, "Nasa radiation belt models ap-8 and ae-8," RADEX INC BEDFORD MA, Tech. Rep., 1989.

[18] D. M. Sawyer, J. I. Vette, "Ap-8 trapped proton environment for solar maximum and solar minimum," *NASA sti/recon technical report n*, vol. 77, p. 18 983, 1976.

[19] J. I. Vette, *The AE-8 trapped electron model environment*, 24. National Space Science Data Center (NSSDC), World Data Center A for Rockets ..., 1991, vol. 91.

[20] W. Dröge, "Acceleration and propagation of solar energetic particles," in *Energy Conversion and Particle Acceleration in the Solar Corona*, Springer, 2003, pp. 193–212.

[21] E. Seedhouse, *Space radiation and astronaut safety*. Springer, 2018.

[22] ESA, *Coronal mass ejection (CME) blast and subsequent impact at Earth*, https://www.esa.int/ESA_Multimedia/Images/2003/04/Coronal_mass_ejection_CME_blast_and_subsequent_impact_at_Earth/, [Online; accessed 09-May-2022], 2003.

[23] K. Petrovay, "Solar cycle prediction," *Living reviews in solar physics*, vol. 7, no. 1, pp. 1–59, 2010.

[24] ESA, *Solar Maximum and Solar Minimum*, https://www.nasa.gov/mission_pages/sunearth/news/solarmin-max.html/, [Online; accessed 09-May-2022], 2012.

[25] SPENVIS, *Solar Particle Models*, https://www.spenvis.oma.be/help/models/sep.html/, [Online; accessed 11-May-2022], 2018.

[26] ——, *SPENVIS*, https://www.spenvis.oma.be/help/background/flare/flare.html, [Online; accessed 02-May-2022], 2018.

[27] M. Moldwin, *An introduction to space weather*. Cambridge University Press Cambridge, 2008, vol. 1.

[28] J. C. Chancellor, G. B. Scott, J. P. Sutton, "Space radiation: The number one risk to astronaut health beyond low earth orbit," *Life*, vol. 4, no. 3, pp. 491–510, 2014.

[29] SPENVIS, *GCR Models*, https://www.spenvis.oma.be/help/background/gcr/gcr.html/, [Online; accessed 11-May-2022], 2018.

[30] ——, *SPENVIS*, https://www.spenvis.oma.be/help/background/gcr/gcr.html#NYM, [Online; accessed 02-May-2022], 2018.

[31] M. B. Demirkoz *et al.*, "Installation of the metu defocusing beamline to perform space radiation tests," in *2019 9th International Conference on Recent Advances in Space Technologies (RAST)*, IEEE, 2019, pp. 355–361.

[32] B. Demirköz, S. Niğdelioğlu, M. Yiğitoğlu, S. Aydın, I. Efthymiopoulos, "Metu defocusing beamline project for the first see tests in turkey and the test results from the metu-dbl preliminary setup," *Nuclear Instruments and Methods in Physics Research Section A: Accelerators, Spectrometers, Detectors and Associated Equipment*, vol. 936, pp. 54–56, 2019.

[33] J. Mazur *et al.*, "New measurements of total ionizing dose in the lunar environment," *Space Weather*, vol. 9, no. 7, 2011.

[34] F. Ravotti, "Dosimetry techniques and radiation test facilities for total ionizing dose testing," *IEEE Transactions on Nuclear Science*, vol. 65, no. 8, pp. 1440–1464, 2018.

[35] E. National Academies of Sciences, Medicine, *et al.*, *Testing at the Speed of Light: The State of US Electronic Parts Space Radiation Testing Infrastructure*. National Academies Press, 2018.

[36] R. A. Weller *et al.*, "Monte carlo simulation of single event effects," *IEEE Transactions on Nuclear Science*, vol. 57, no. 4, pp. 1726–1746, 2010.

[37] J. M. Maclaren, T. Majni, *Hard/soft error detection*, US Patent 6,711,703, Mar. 2004.

[38] ESA, *ESCC-SINGLE EVENT EFFECTS TEST METHOD AND GUIDELINES*, `https://escies.org/`, [Online; accessed 12-May-2022], 2014.

[39] A. Albarodi, "Design of a space radiation monitor for a spacecraft in leoand results from a prototype on the first turkish sounding rocket," M.S. thesis, Middle East Technical University, 2021.

[40] M. Marinella, H. Barnaby, "Total ionizing dose and displacement damage effects in embedded memory technologies (tutorial notes-draft 1).," Sandia National Lab.(SNL-NM), Albuquerque, NM (United States), Tech. Rep., 2013.

[41] J. R. Srour, J. M. McGarrity, "Radiation effects on microelectronics in space," *Proceedings of the IEEE*, vol. 76, no. 11, pp. 1443–1469, 1988.

[42] E. Lavrik, "Development of quality assurance procedures and methods for the cbm silicon tracking system," Ph.D. dissertation, Universität Tübingen, 2017.

[43] R. Biesbroek, G. Janin, "Ways to the moon," *ESA bulletin*, vol. 103, pp. 92–99, 2000.

[44] J. Touma, J. Wisdom, "Evolution of the earth-moon system," *The Astronomical Journal*, vol. 108, pp. 1943–1961, 1994.

[45] T. Murphy, "Lunar laser ranging: The millimeter challenge," *Reports on Progress in Physics*, vol. 76, no. 7, p. 076 901, 2013.

[46] M. Loucks, J. P. Carrico, T. Carrico, C. Deiterich, "A comparison of lunar landing trajectory strategies using numerical simulations," 2005.

[47] W. S. Koon, M. W. Lo, J. E. Marsden, S. D. Ross, "Low energy transfer to the moon," *Celestial Mechanics and Dynamical Astronomy*, vol. 81, no. 1, pp. 63–73, 2001.

[48] M. J. Ruiz, J. Perkins, "Spacex rocket data satisfies elementary hohmann transfer formula," *Physics Education*, vol. 55, no. 2, p. 025 011, 2020.

[49] M. A. Khan, "Equatorial radius of the earth: A dynamical determination," *Bulletin Géodésique (1946-1975)*, vol. 109, no. 1, pp. 227–235, 1973.

[50] E. Tiesinga, P. J. Mohr, D. B. Newell, B. N. Taylor, "Codata recommended values of the fundamental physical constants: 2018," *Journal of Physical and Chemical Reference Data*, vol. 50, no. 3, p. 033 105, 2021.

[51] D. R. Williams, *Earth fact sheet*, https://nssdc.gsfc.nasa.gov/planetary/factsheet/earthfact.html/, [Online; accessed 15-May-2022], 2021.

[52] F. Rimrott, F. Salustri, "A note on hohmann transfer velocity kicks," *Technische Mechanik-European Journal of Engineering Mechanics*, vol. 21, no. 2, pp. 135–143, 2001.

[53] D. R. Williams, *Moon fact sheet*, https://nssdc.gsfc.nasa.gov/planetary/factsheet/moonfact.html/, [Online; accessed 15-May-2022], 2021.

[54] N. Vighnesam, A. Sonney, N. Gopinath, "India's first lunar mission chandrayaan-1 initial phase orbit determination," *Acta Astronautica*, vol. 67, no. 7-8, pp. 784–792, 2010.

[55] ISRO, *Chandrayaan 1 mission*, https://www.issdc.gov.in/chandrayaan1.html/, [Online; accessed 17-May-2022], 2008.

[56] NASA, *Eart*, https://www.nasa.gov/topics/earth/index.html/, [Online; accessed 14-May-2022], 2021.

[57] ——, *Nasa gazes at the strawberry moon*, https://www.nasa.gov/image-feature/goddard/2021/nasa-gazes-at-the-strawberry-moon/, [Online; accessed 14-May-2022], 2021.

[58] B. Yaglioglu, "Türkiye'nin ay görevi hedefleri," *Türkiye Cumhuriyeti Sanayi ve Teknoloji Bakanlığı Anahtar Dergi*, no. 396, pp. 20–22, 2021.

[59] D. C. Folta, N. Bosanac, D. Guzzetti, K. C. Howell, "An earth–moon system trajectory design reference catalog," *Acta Astronautica*, vol. 110, pp. 341–353, 2015.

[60] NASA, *General mission analysis tool (gmat) version r2018a*, https://software.nasa.gov/software/GSC-18094-1/, [Online; accessed 16-May-2022], 2018.

[61] Nasa, *Lunar reconnaissance orbiter*, https://lunar.gsfc.nasa.gov/, [Online; accessed 18-May-2022].

[62] C. R. Tooley *et al.*, "Lunar reconnaissance orbiter mission and spacecraft design," *Space Science Reviews*, vol. 150, no. 1, pp. 23–62, 2010.

[63] Autodesk, *Autocad*, version 2022, Dec. 2021. [Online]. Available: https://www.autodesk.com/.

[64] FreeCAD Community, *Freecad*. [Online]. Available: https://www.freecadweb.org/.

[65] M. Pinto, P. Gonçalves, "Guimesh: A tool to import step geometries into geant4 via gdml," *Computer Physics Communications*, vol. 239, pp. 150–156, 2019.

[66] V. Mitrikas, "Simulation of the radiation load on the radom radiation monitor on the "chandrayaan-1" space vehicle during flight within the earth's magnetosphere," *The Russian Federation State Research Center- Journal of Aerospace and Environmental Medicine*, vol. 55, no. 1, pp. 76–81, 2021.

[67] J. A. Halchak, J. L. Cannon, C. Brown, "Materials for liquid propulsion systems," American Institute of Aeronautics and Astronautics, Tech. Rep., 2018.

[68] S. Rajesh, G. Suresh, R. C. Mohan, "A review on material selection and fabrication of composite solid rocket motor (srm) casing," *Int. J Mech. Solid*, vol. 9, no. 1, pp. 125–138, 2017.

[69] F. Heeg, L. Kilzer, R. Seitz, E. Stoll, "Design and test of a student hybrid rocket engine with an external carbon fiber composite structure," *Aerospace*, vol. 7, no. 5, p. 57, 2020.

[70] D. V. Reames, "Element abundances of solar energetic particles and the photosphere, the corona, and the solar wind," *Atoms*, vol. 7, no. 4, p. 104, 2019.

[71] ——, *Solar energetic particles: a modern primer on understanding sources, acceleration and propagation*. Springer Nature, 2021.

[72] J. Allison *et al.*, "Recent developments in geant4," *Nuclear instruments and methods in physics research section A: Accelerators, Spectrometers, Detectors and Associated Equipment*, vol. 835, pp. 186–225, 2016.

[73] S. Agostinelli *et al.*, "Geant4—a simulation toolkit," *Nuclear instruments and methods in physics research section A: Accelerators, Spectrometers, Detectors and Associated Equipment*, vol. 506, no. 3, pp. 250–303, 2003.

[74] J. Allison *et al.*, "Geant4 developments and applications," *IEEE Transactions on nuclear science*, vol. 53, no. 1, pp. 270–278, 2006.

[75] ISRO, *Chandrayaan-1*, `https://www.isro.gov.in/Spacecraft/chandrayaan-1/`, [Online; accessed 20-May-2022], 2008.

[76] T. Dachev, B. Tomov, P. Dimitrov, Y. Matviichuk, "Monitoring lunar radiation environment: Radom instrument on chandrayaan-1," *Current science*, pp. 544–546, 2009.

[77] SWPC/NOAA, *Solar cycle progression*, `https://www.swpc.noaa.gov/products/solar-cycle-progression`, [Online; accessed 25-May-2022], 2022.

Projects

1. Space Radiation Effects Feasibility Study for The Turkish Space Program-Lunar Mission
   YTU Scientific Research Project Office - FBG-2021-4332